Reduction of uncertainty in stability calculations for slopes under seepage

Liu, Kang

DOI
10.4233/uuid:8736e6df-f2fb-48ac-aa28-7d61a214507e

Publication date
2017

Document Version
Final published version

Citation (APA)
Liu, K. (2017). *Reduction of uncertainty in stability calculations for slopes under seepage*. [Dissertation (TU Delft), Delft University of Technology]. https://doi.org/10.4233/uuid:8736e6df-f2fb-48ac-aa28-7d61a214507e

Reduction of uncertainty in stability calculations for slopes under seepage

Reduction of uncertainty in stability calculations for slopes under seepage

Proefschrift

ter verkrijging van de graad van doctor
aan de Technische Universiteit Delft,
op gezag van de Rector Magnificus prof. ir. K.C.A.M. Luyben,
voorzitter van het College voor Promoties,
in het openbaar te verdedigen op vrijdag 22 september 2017 om 15:00 uur

door

Kang LIU

Master of Science in Hydraulic Structure Engineering,
Hohai University, Nanjing, China,
geboren te Anhui, China.

Dit proefschrift is goedgekeurd door de

promotor: prof. dr. M. A. Hicks
copromotor: dr. P. J. Vardon

Samenstelling promotiecommissie:

Rector Magnificus,	voorzitter
Prof. dr. M. A. Hicks,	Technische Universiteit Delft
Dr. P. J. Vardon,	Technische Universiteit Delft

Onafhankelijke leden:

Prof. dr. N. Dixon,	Loughborough University
Prof. dr. C. Jommi,	Technische Universiteit Delft
Prof. dr. ir. S. N. Jonkman,	Technische Universiteit Delft
Prof. dr. S. Utili,	Newcastle University
Dr. ir. F. C. Vossepoel,	Technische Universiteit Delft

Keywords: Data assimilation, ensemble Kalman filter, heterogeneity, inverse analysis, seepage, slope stability, uncertainty reduction, unsaturated soil

Printed by: Ipskamp Drukker

Author: Kang LIU

Email: k.liu@tudelft.nl; kangliu922@yahoo.com

ISBN 978-94-6186-844-2

An electronic version of this dissertation is available at
http://repository.tudelft.nl/.

To my family

Contents

1

Introduction

1

1.1. Background

Soil slopes under seepage are common geotechnical structures, such as embankments, dikes, and dams. The stability of such slopes is of great concern to engineers due to the high potential consequences of failure. Examples include the Juvre dike breach after a storm surge in Denmark in 1999, and the failure of a peat dike in Wilnis in the Netherlands in 2003 (Van Baars, 2005) (see Figure 1.1).

(a) (b)

Figure 1.1: Soil slope failures: (a) Juvre dike breach; (b) peat dike failure in Wilnis.

A variety of analysis methods have been developed, initially utilising a factor of safety (FOS) to define the ratio between the resistance and de-stabilising forces. Popular methods used to calculate the FOS include the limit equilibrium method (LEM) and the finite element method (FEM). The LEM approach includes the Fellenius, Bishop, Janbu, Morgenstern–Price, Spencer and Sarma methods. These approaches divide the soil above the slip surface into a number of slices and consider the force equilibrium in the sliding area, such as forces along the slip surface and between the slices. Based on different assumptions regarding both the forces between the slices and the shape of the slip surface, the different approaches were formulated. For example, the Fellenius method assumes that the slip surface is circular and there are no inter-slice forces, whereas the Bishop method does take some account (albeit simplified) of inter-slice forces. The other four methods deal with non-circular slip surfaces. The FEM approach discretizes the slope domain into small elements and calculates the stress–strain behaviour in order to investigate the slope behaviour. FEM can search for the critical slip surface without assuming its shape in advance, and often follows one of two approaches. One method is to increase the gravity load (Chen and Mizuno, 1990) and the second approach is to reduce the strength characteristics of the soil mass, i.e. the strength reduction method (SRM) (Matsui and San, 1992).

More recently, probabilistic analyses have been used, which utilise the uncertainty in soil property values to determine the probability of failure. Due to the

natural variability of soils, slopes do fail occasionally, even when the FOS had previously been calculated to be greater than 1.0. To better reflect the uncertainty in the slope stability, the reliability index has been proposed, due to it being able to incorporate the variability of soil parameters. Probabilistic methods range from simplified methods, such as the first order reliability method (FORM) and point estimate method (PEM), to more complex and accurate methods such as the Monte Carlo method (MCM).

In the probabilistic analysis of slope stability, the precision depends on the estimation of the uncertainty existing in the soil parameters. Normally, the variation in a soil parameter is characterised by a distribution, e.g. normal, log-normal or Gamma. This distribution is generally based on limited field or laboratory tests of soil parameters. However, these distributions only provide a general description of the variation of the soil, e.g. the mean and standard deviation of the soil parameters.

Using probabilistic analyses with given distributions, wide ranges of possible outcomes are often encountered. In order to narrow down the range, researchers have found that the local variability, i.e. the spatial correlation of property values, and the observation of the performance of geotechnical structures can be used. Indeed, inverse analysis can be considered as a way to reduce the uncertainty in the stability analysis of a slope under seepage. This thesis investigates this aspect, with the aim to reduce uncertainty in the behaviour of existing structures.

1.2. Motivation

Accurate prediction of the slope stability for existing structures is important to help investors protect assets. Currently, the estimation of soil parameters mainly depends on field or laboratory tests. However, there are many in-situ monitoring devices installed in the field and observations of a structure's behaviour can be utilised to improve the estimation of soil parameters, as well as the prediction of a structure's behaviour.

Additional complexity in the hydro-mechanical behaviour may also impact the calculated stability. For example, the hysteresis in the water retention behaviour of unsaturated soils has a significant impact on the seepage results, i.e. the suction/pore water pressure, which, in turn, affects the analysis of slope stability. Therefore, it is essential to incorporate the complex water retention behaviour.

1.3. Aims and objectives

The overall aim of this thesis is to reduce the uncertainty that exists in the stability analysis of a slope under seepage. The thesis considers three different ways to achieve this. One way is to use the hydraulic measurements of geotechnical projects to improve the estimation of hydraulic parameters. A second way is to cross-correlate the hydraulic and mechanical parameters so that it can reduce the uncertainty of strength parameters. The third way is to improve the simulation of the hydraulic behaviour of unsaturated soils.

In order to achieve the above objectives, the following tasks have been defined:

- To propose a framework which links the stochastic analysis of seepage and slope stability with a method of data assimilation, i.e. the ensemble Kalman filter (EnKF) in this thesis;
- To implement the governing equation of steady state saturated or transient saturated–unsaturated seepage, considering the spatial variability of hydraulic parameters, and the EnKF within a finite element code;
- To cross-correlate the hydraulic and mechanical parameters in order to reduce the uncertainty of strength parameters based on the improved estimation of hydraulic parameters;
- To investigate the proposed framework for an embankment experiencing both steady state and transient seepage;
- To incorporate the effect of hysteresis in the soil water retention curve (SWRC) into saturated–unsaturated seepage and combine the hysteretic effect with the spatial variability of hydraulic parameters.

1.4. Outline of the thesis

The thesis contains the following chapters:

Chapter 2 reviews the relevant literature. In this chapter, the variability of soil parameters, specifically hydraulic conductivity, is reviewed, and the cross-correlations between different soil parameters is discussed. Then, previous research on the stochastic analysis of slope stability under seepage is investigated. Finally, the methods used for data assimilation (or inverse analysis) in geotechnical engineering are reviewed.

Chapter 3 proposes a framework which first utilises hydraulic measurements to reduce the uncertainty in the estimation of hydraulic parameters via inverse analysis using the ensemble Kalman filter (EnKF). Then, the improved estimation of hydraulic parameters is used to improve the mechanical parameters based on a cross-correlation between them. Finally, after reducing the uncertainty in the soil parameters, the impact on slope stability analyses has been investigated. The proposed framework is investigated for an embankment under saturated steady state seepage.

Chapter 4 applies the proposed framework presented in Chapter 3 to an embankment under saturated–unsaturated transient seepage. In the transient seepage process, the EnKF is again used to improve performance. Additionally, the influence of the spatial continuity (scale of fluctuation) and the initial estimation of soil parameters has been investigated.

Chapter 5 aims to improve the accuracy in the stability analysis of slopes under stochastic seepage by taking a more detailed account of unsaturated soil behaviour. Specifically, the water retention behaviour is modelled more realistically than in previous research by considering the hysteretic effect in the water retention behaviour (represented by the soil water retention curve (SWRC)).

Chapter 6 presents a probabilistic analysis of the water velocity distribution in an earth embankment under saturated stochastic seepage, considering the spatial variability of the hydraulic conductivity. The influence of the velocity distribution is discussed in relation to the piping failure mechanism.

Chapter 7 presents an overview and the conclusions of the thesis, as well as several recommendations for future research.

2

Literature Review

2. Literature Review

2.1. Introduction

This chapter provides a critical overview of literature related to the thesis and is divided into three main sections. Section 2.2 describes the stochastic analysis of seepage and slope stability. In Section 2.3, the cross-correlation between different soil parameters is presented. Inverse analysis methods applied in geotechnical engineering are reviewed in Section 2.4. The last section, i.e. Section 2.5, provides some concluding comments on the reviewed work.

In this chapter, the reviewed literature is a general introduction to soil variability and the numerical methods which are used in the thesis. In the following chapters additional literature is reviewed, specific to the subject of that chapter. Hence, in Chapters 3 and 4, literature on reliability methods used in geotechnical applications is reviewed, including the impact of spatial variability. Additionally, types of inverse analysis and data assimilation are introduced. In Chapter 5 literature on the hysteresis observed in soil water retention behaviour is reviewed, with a particular emphasis on the impact on slope stability. Chapter 6 gives a review of the assessment of piping.

2.2. Soil variability

Natural soils have long been recognised as heterogeneous materials (Lumb, 1966; DeGroot and Baecher, 1993). Therefore, the soil property values are spatially random variables, which means they are different at different locations. A statistical description, i.e. probability density function (PDF), can be used to characterise the pointwise variability of the soil property values. In the PDF, μ and σ are the mean and standard deviation, respectively. The coefficient of variation (COV), which describes the dispersion of the variable, is defined as

$$COV = \frac{\sigma}{\mu} \tag{2.1}$$

2.2.1. Spatial variability of hydraulic conductivity

For hydraulic conductivity, k, the mean, μ_k, mainly depends on the soil type or composition. Table 2.1 presents mean values of hydraulic conductivity presented in the literature.

Nielsen et al. (1973) reported that the COV of hydraulic conductivity of soil varied from 0.9 to 1.0 and indicated that the distribution of hydraulic conductivity was log-normal. Carsel and Parrish (1988) investigated the COV of different types of soil. They found that the COV increased from sand to clay, i.e. $COV = 0.524$ for a sand and $COV = 4.533$ for a silty clay. They also found that the distribution of hydraulic conductivity was log-normal. Rayne et al. (1996) reported the COV of hydraulic conductivity to be 62.1%, 66% and 43.6% for a sand till by using slug tests, bail tests and pumping tests, respectively. Gupta et al. (2006) found the COV of a sandy loam to be 111.3% and 109% by using a double ring infiltrometer and Guelph permeameter, respectively, with the hydraulic conductivity generally being log-normally distributed. Duncan (2000) reported the COV of hydraulic conductivity

Table 2.1: Reported means of hydraulic conductivity for different soils

Soil type	μ_k (m/s)	References
Gravel	10^{-3}–10^{-2}	Verruijt (2012)
Coarse sand	1.38×10^{-3}	Wells et al. (2006)
Sandy till	2.9×10^{-4}, 1.5×10^{-4}, 3.9×10^{-4}	Rayne et al. (1996)
Sand	10^{-6}–10^{-3}	Verruijt (2012)
	10^{-5}–10^{-3}	Robertson (2010)
	9×10^{-7}, 2×10^{-7}	Campanella et al. (1995)
Loamy sand	4.9×10^{-5}	Freeze (1975)
Sandy loam	8.111×10^{-6}, 1.164×10^{-5}	Gupta et al. (2006)
	3.7×10^{-6}	Springer and Cundy (1987)
Silt	10^{-8}–10^{-6}	Verruijt (2012)
Silty clay	2.21×10^{-7}, 5.71×10^{-6}, 2.71×10^{-5}	Freeze (1975)
Clay	10^{-10}–10^{-8}	Verruijt (2012)
	10^{-10}–10^{-9}	Robertson (2010)
	4.1×10^{-10}	Campanella et al. (1995)
	4.91×10^{-8}, 2.297×10^{-7}, 6.8×10^{-7}	Freeze (1975)
Peat	10^{-8}–10^{-5}	Mesri et al. (1997); Huat et al. (2011)
	Around 10^{-6}	Schlotzhauer and Price (1999)
	5×10^{-5}	Dai and Sparling (1973)

of saturated clay to be 68–90% and Zhu et al. (2013) gave a range of COV for sand of 60–100%.

In addition to the mean and coefficient of variation of a soil parameter (e.g. hydraulic conductivity), the scale of fluctuation (SOF) is essential to characterise the spatial nature of the variability. The SOF is defined as the distance within which the soil property values of two points are significantly correlated. Hence, when the SOF is much larger than the size of the structure, for example, there is little variation in the soil property values within the structure. There is only a limited literature relating to the values of SOF. Phoon and Kulhawy (1999) reported that the vertical SOF could be from 1 m to 6 m, whereas the horizontal SOF could typically be within a range of 40–60 m. El-Ramly et al. (2003) reported values of autocorrelation distance of 10–40 m in the horizontal direction and 1–3 m in the vertical direction. The SOF and autocorrelation distance are similar in concept, but the SOF is 2 times the autocorrelation distance for the exponential autocovariance function. Hence, the values of El-Ramly et al. (2003) were consistent with Phoon and Kulhawy (1999) after being transformed into SOF. Hicks and Samy (2002a) suggested that the vertical SOF could be 0.3–3 m and that the degree of anisotropy of the heterogeneity, i.e. the ratio of horizontal to vertical SOFs, is typically greater than 10. Cho and Park (2010) indicated that the ratio of the correlation distance in the vertical direction to that in the horizontal direction was in the range of 1 to 10, and was mainly due to the geological soil formation process. Firouzianbandpey et al. (2014) studied a sand layer deposit in Denmark and found that the vertical correlation length was two to seven times shorter than that in the horizontal direction. In the vertical direction, the spatial correlation lengths were estimated to be from 0.2 m to 0.5 m.

2.2.2. Cross-correlation between soil parameters

Geotechnical parameters are not always independent of each other and there may be a strong interdependence between stochastic variables (Nguyen and Chowdhury, 1985). Figure 2.1 shows the influence of different correlation coefficients between two stochastic variables on the distribution of parameters. The correlation coefficient between two variables is defined as:

$$\rho_{X,Y} = \frac{COV(X,Y)}{\sigma_X \sigma_Y} = \frac{\mathrm{E}[(X-\overline{X})(Y-\overline{Y})]}{\sigma_X \sigma_Y} \tag{2.2}$$

where X and Y are the variables, $-1 \leq \rho_{X,Y} \leq 1$ is the correlation coefficient, $COV(X,Y)$ is the covariance of the two variables, and σ_X and σ_Y are the standard deviation of X and Y, respectively. If $\rho_{X,Y} > 0$, the variable Y increases with an increase in X. Conversely, if $\rho_{X,Y} < 0$, the variable Y decreases with an increase in X.

Previous literature mainly considered cross-correlated strength parameters or hydraulic parameters separately. The effect of the cross-correlation between strength and hydraulic parameters is seldomly investigated (an exception being Arnold and Hicks (2011)). However, although there is no literature directly showing the cross-correlation between strength and hydraulic parameters, many studies have implied its existence.

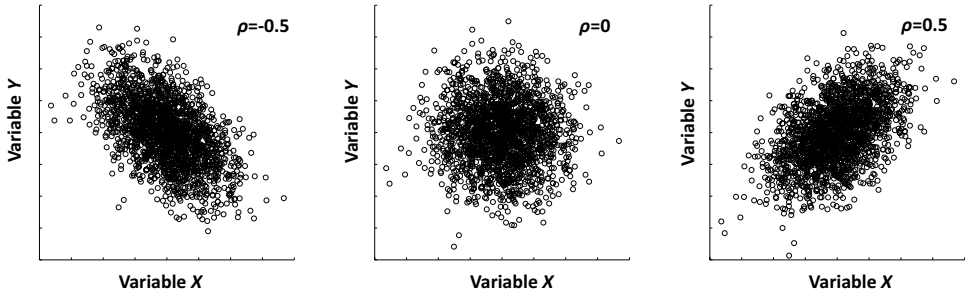

Figure 2.1: Different correlation coefficients between two variables (Phoon and Ching, 2014).

Hydraulic parameters are generally considered to be correlated to porosity or plastic/liquid limit. The well-known Kozeny–Carman equation (Carman, 1937) correlates the saturated hydraulic conductivity with porosity and particle size, and has been widely applied in research, such as in Le et al. (2015). The equation defines a relationship in which the hydraulic conductivity increases with increasing porosity and increasing particle size. Vallejo and Mawby (2000) investigated the influence of porosity and particle size on the shear strength of granular mixtures and found that the porosity of the mixture has a strong influence on the shear strength, with the peak shear strength generally correlating to the minimum porosity. Bartetzko and Kopf (2007) studied the undrained shear strength and porosity versus depth relationships of marine sediments. While a spread of results was noted, most field tests exhibited an increase in shear strength with depth and a decrease in porosity, that is, the porosity and shear strength were negatively correlated. Moreover, the effect of particle size was also studied; it was shown that the shear strength, in terms of the coefficient of friction, increased with an increase in quartz content (and a decrease in clay content). Thevanayagam (1998) investigated the effects of particle size and void ratio on the undrained shear strength, finding that, in general, with a lower porosity the shear strength increased. The mixture of particle sizes influenced the shear strength in a more complex way, with high proportions of a certain constituent particle size dominating the behaviour, alongside a dependence on density and confining pressure.

Deng et al. (2011) proposed an improved method to estimate the hydraulic conductivity of Boom Clay, by using an empirical relationship incorporating void ratio and liquid limit. Holtz and Krizek (1971) studied some triaxial test data and built two correlation matrices for several soil parameters including the liquid limit, cohesion and friction angle. The correlation matrices contained correlation coefficients between pairs of different variables, i.e.

$$\rho = \begin{bmatrix} 1 & \rho_{x,y} & \cdots & \rho_{x,z} \\ \rho_{x,y} & 1 & \cdots & \rho_{y,z} \\ \vdots & \vdots & \ddots & \vdots \\ \rho_{x,z} & \rho_{y,z} & \cdots & 1 \end{bmatrix} \tag{2.3}$$

Holtz and Krizek (1971) reported that both cohesion and friction are negatively

correlated to the liquid limit. Ching and Phoon (2014) pointed out that the liquid limit was correlated with undrained shear strength. Vardanega and Haigh (2014) indicated that the undrained shear strength is negatively correlated to the liquidity index, which is a function of the liquid index and plastic index.

Overall, the literature implies that when the porosity decreases, the hydraulic conductivity decreases as well. Moreover, the decreased porosity causes a friction angle increase (Bjerrum et al., 1961). A cross-correlation between cohesion and saturated hydraulic conductivity has also been shown to exist for specific soils, although the coefficient can be either negative or positive. Therefore, it is reasonable to assume that the effective shear strength variables, c' and ϕ', and the hydraulic parameters can be cross-correlated. However, the correlation properties will depend on how the variation of a soil in a certain locale depends upon the particle size and/or porosity distributions.

2.3. Stochastic analysis

2.3.1. Stochastic analysis of seepage

The concept of stochastic analysis of seepage has emerged since the 1960s (Warren and Price, 1961; McMillan, 1966; Freeze, 1975; Gelhar, 1976; Bakr et al., 1978; Tang and Pinder, 1977). Researchers have employed different methods to deal with seepage behavior, including spectral analysis, numerical solution of the stochastic flow equation and the MCM.

Stochastic analysis of seepage requires a representation of the spatial variability of the hydraulic conductivity. In early research, stochastic seepage analyses were undertaken assuming that the hydraulic conductivity in adjacent elements or blocks were independent (Freeze, 1975). However, the generated heterogeneous field of hydraulic conductivity was not realistic because soil parameters are inherently correlated in space due to natural depositional processes or to construction techniques. Bakr et al. (1978) and Smith and Freeze (1979a,b) started to account for the spatial correlation of hydraulic conductivity. They utilised random fields to model the spatial variability of soil parameters; such a field is filled with stochastic values of a soil parameter following a specific distribution, with the values at different locations being variable and correlated. The random fields of hydraulic conductivity were generated by both the Fourier–Stieltjes representation and the nearest-neighbor stochastic process model. Vanmarcke (1977) proposed local average theory and Fenton and Vanmarcke (1990) developed the Local Average Subdivision (LAS) method to simulate spatially correlated random fields. An advantage of LAS is that it is compatible with FEM and can be easily implemented in a FEM program, as the values of each block generated by the LAS can fit in the elements of the FEM.

Griffiths and Fenton (1993) applied LAS to a water retaining structure overlying a heterogeneous foundation. This was the first use of LAS in a stochastic seepage analysis. They used it to generate spatially correlated random fields, and used FEM with MCM to study the statistics of the flow rate, exit gradient and uplift pressure. They also compared the stochastic results with deterministic results. The

results indicated that three quantities (i.e. the flow rate, exit gradient and uplift pressure) were significantly affected by the heterogeneity of hydraulic conductivity, i.e. by its standard deviation and spatial correlation. In addition to LAS, there are various methods to generate random fields, such as the turning bands method (TBM) (Matheron, 1973), fast Fourier transform (FFT) method (Cooley and Tukey, 1965), and moving average method (Gersch and Yonemoto, 1977). Fenton (1994) made a comparison of three of the methods, namely FFT, TBM and LAS, in terms of their run-time and accuracy. When combining random field generators with FEM analysis, LAS was shown to be able to produce random fields whose statistics are consistent with the prior distribution of soil parameters. Moreover, it is ideally suited for use with finite elements, as each local average becomes an element property; that is, the random field can be mapped directly onto a finite element mesh. Fenton and Griffiths (1996, 1997) extended their previous confined seepage analysis to investigate an unconfined seepage problem, i.e. seepage in an earth dam. They analysed the influence of the standard deviation and spatial correlation of hydraulic conductivity on the free surface and flow rate. Griffiths and Fenton (1997) extended the confined seepage investigation of Griffiths and Fenton (1993) to three dimensions. Revelli and Ridolfi (2000) studied the influence of heterogeneity on the flow in a rectangular unconfined aquifer, where the random field of hydraulic conductivity was generated by the Fourier inverse transform. The consequences on the free surface position and on the total discharge were investigated. Ahmed (2009) extended the work of Fenton and Griffiths (1996), regarding free surface flow in earth dams, by introducing anisotropic heterogeneity in the analysis and used a fixed FE mesh approach to solve the unconfined flow. Srivastava et al. (2010) used FLAC 5.0 to analyse steady state seepage flow in a slope with a foundation layer, and also its corresponding stability. A finite difference approach was used to solve the flow equation and the (isotropic) hydraulic conductivity was considered as a random variable. Moreover, the porosity and dry unit weight were related to the hydraulic conductivity via the Kozeny–Carman equation (Carman, 1937). Therefore, these two variables were both considered as random variables and calculated based on hydraulic conductivity, which impacted the subsequent slope stability analysis. Ahmed (2012) investigated steady state confined flow under a hydraulic structure with a single sheet pile wall, extending the research of Griffiths and Fenton (1993). The hydraulic conductivity was modelled as heterogeneous and anisotropic. The influence of the degree of anisotropy on the hydraulic responses, i.e. the flow rate, uplift force and exit gradient, was studied.

Gui et al. (2000) studied transient seepage in an earth dam without a foundation layer, in which the influence of spatial variability of the hydraulic conductivity on the seepage and slope stability were investigated. The random hydraulic conductivity was generated by TBM. Le et al. (2012) also investigated stochastic transient seepage in an earth dam. In their paper, the porosity was considered to be a random variable and modelled by LAS. The saturated hydraulic conductivity and the parameter related to the suction value at which the soil starts to desaturate were both derived from the porosity. Cho (2012) used the Karhunen–Loéve expansion to generate two different uncorrelated random fields for an embankment and founda-

tion. The steady state seepage in an embankment overlying a foundation layer was studied, and the difference between one case in which a single random field was used to simulate the embankment and foundation and another case using two random fields was investigated. In addition, the sensitivity of the seepage behaviour in relation to the heterogeneity of the embankment or the foundation separately was investigated. Zhu et al. (2013) analysed a slope, which had a spatially variable saturated hydraulic conductivity, subjected to steady state rainfall infiltration. The random hydraulic conductivity was generated by FFT.

In the three studies of the previous paragraph, the unsaturated zone in the embankment or slope was considered in the seepage analyses. It has been recognised that the soil water retention behaviour of an unsaturated soil plays an important role in the simulation of saturated–unsaturated seepage. In the water retention behaviour, hysteresis is commonly seen and the effect of hysteresis on seepage has been investigated in several studies (Yang et al., 2012a; Wu et al., 2012; Bashir et al., 2015). However, most of these studies are limited to homogeneous domains. For example, Yang et al. (2012a) considered the effect of hysteresis in the infiltration modelling of a 1D soil column and compared the numerical results to experimental results done by other researchers. They found that the results with hysteresis were closer to the experimental results.

Nakagawa et al. (2012) pointed out the importance of considering both hysteresis and heterogeneity in the simulation of unsaturated flow, by comparing the numerical computation with laboratory tests. Yang et al. (2012b) studied a heterogeneous one-dimensional soil column in which hysteresis was considered. It was shown that the hysteretic effect increases the uncertainty in the degree of water infiltration downwards compared to a non-hysteretic heterogeneous case. Zhang (2007) studied a 2D slope subjected to rainfall infiltration in which hysteresis was considered. The author considered several hydraulic parameters used in Fredlund and Xing's (1994) equation for simulating the soil water retention curve, e.g. the saturated hydraulic conductivity and the saturated volumetric water content, as random variables, and calculated the mean and standard deviation of the FOS. It was pointed out that the reliability of the slope was underestimated without considering the effect of hysteresis. However, in the paper, the influence of the spatial variability of soil parameters, i.e. the SOF, was not analysed. Therefore, due to the lack of consideration of spatial variability, the influence of modelling hysteresis in stochastic analyses of 2D saturated–unsaturated seepage needs to be further investigated.

2.3.2. Stochastic analysis of slope stability

By the 1970s, the emerging field of structural reliability started to influence research in geotechnical engineering, and slope and embankment reliability analyses were carried out. Wu and Kraft (1970) took account of uncertainties in the computation of the failure probability of slopes designed according to conventional practice, and studied the effect of uncertainties on the optimum design and expected cost. Tang et al. (1976) also researched the design of slopes based on probabilistic theory. Meanwhile, Cornell (1972), Alonso (1976) and Vanmarcke (1977) took various un-

certainties into account and analysed their influence on slope stability uncertainty. In Alonso's paper, he pointed out that there were reported failures for computed safety factors larger than 1.0, indicating that, no matter what FOS is found by analytical means, there is always some chance of failure. For example, in a heterogeneous slope, the local strength parameters (cohesion and friction angle) are different everywhere. If a weak zone is located along the slope surface, the slope could fail through the weak zone even if the calculated FOS for the slope as a whole is greater than 1.0. Therefore, reliability analysis was proposed as a more reasonable way of understanding safety. In this respect, the reliability index, β, is defined as

$$\beta = \frac{\mu_F}{\sigma_F} \tag{2.4}$$

where μ_F and σ_F are the mean and standard deviation of the performance function F. In slope stability analysis, the performance function can be defined as $F = \mathrm{FOS} - 1$. When the reliability index is determined, the reliability can be calculated according to the distribution of F. For example, if F is normally distributed, the reliability is $1 - \Phi(-\beta)$, where $\Phi(-\beta)$ is defined as the probability of failure (i.e. the hatched area below the curve in Figure 2.2).

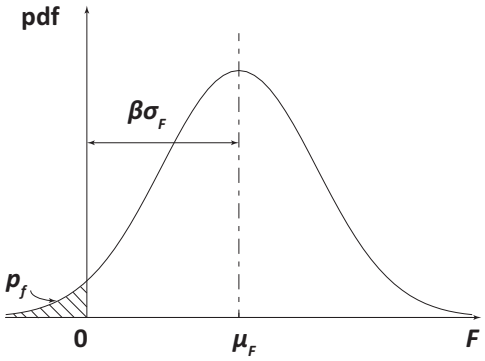

Figure 2.2: Illustration of reliability index and probability of failure (Baecher and Christian, 2005).

Over the years, several methods have been proposed to conduct probabilistic analyses of slope stability, e.g. the First Order Second Moment (FOSM) method (Cornell, 1969, 1970), FORM (Hasofer and Lind, 1974), PEM (Rosenblueth, 1975, 1981), Second Order Reliability Method (SORM) (Madsen, 1985) and MCM. Reliability tools such as FOSM, FORM, PEM and SORM reduce the computational load by simplifying the problem. However, arising from these simplifications, the uncertainties that exist in problems are not always taken into account well. For example, if FORM is used to calculate the probability of failure of a slope, only the mean and standard deviation of the soil strength parameters are used. The local variability of the strength parameters across the domain is ignored, and hence the slope is still considered to be homogeneous. Therefore, MCM, which can take the uncertainties of soil parameters into account more thoroughly, has often been preferred.

Griffiths and Fenton (1993) proposed the random finite element method (RFEM), which links together random fields, FEM and MCM, to conduct stochastic analyses of a confined seepage problem, and Fenton and Griffiths (1996, 1997) extended this work to an unconfined seepage problem, i.e. seepage through an earth dam. Hicks and Samy (2002b) used RFEM to study the influence of anisotropy of the heterogeneity and depth trends in the undrained shear strength on slope reliability. Griffiths and Fenton (2004) analysed a cohesive slope and studied two scenarios: one using the "single random variable approach", meaning that the spatial correlation length was infinity and no local averaging was applied; the other involving a full RFEM analysis of slope stability. By comparing these two situations, the influence of spatial correlation length and local averaging on the slope stability was shown. Hicks and Samy (2004) studied the influence of slope angle for slopes cut in a clay layer, for spatially varying undrained shear strength, including the influence of anisotropy of the heterogeneity and strength increasing linearly with depth. Griffiths and Fenton (2007) applied RFEM in a range of problems, including steady state seepage, foundation settlement and slope stability. In these problems, the hydraulic conductivity in the steady seepage analysis, the stiffness in the foundation settlement analysis and the cohesion in slope stability analysis were considered as random variables. The random fields were generated based on LAS. Hicks et al. (2007) and Hicks and Spencer (2008, 2010) implemented RFEM in 3D slope analyses. They compared the results of 2D and 3D analyses of failure in slope, showing that 3D aspects cannot be ignored. Hicks et al. (2014) extended the investigations of Hicks and Spencer (2008, 2010) to more closely quantify failure volumes in 3D slopes, once again considering the spatial variability of the undrained shear strength. Li et al. (2015a) compared and evaluated the performance of RFEM with respect to a simplified method proposed by Vanmarcke (1977) in 3D slope analyses, thereby demonstrating the greater flexibility and robustness of RFEM, especially for smaller SOFs, whereas Li et al. (2015b) studied the stability of a 3D heterogeneous slope and focused on the number of discrete failures in the slope. Arnold and Hicks (2011) applied RFEM to a slope subjected to rainfall. The rainfall infiltration and slope stability were both modelled by stochastic analysis, in which the hydraulic and strength parameters were both spatially random variables.

2.3.3. Stochastic analysis considering cross-correlated soil parameters

The influence of the cross-correlation of soil parameters on stochastic analyses has been rarely investigated by researchers and engineers. Nguyen and Chowdhury (1985) first developed a Monte Carlo simulation which took account of correlation between two variables, i.e. the hydraulic conductivity and the storage coefficient. They demonstrated the effect of correlation between the two variables on water level drawdown in the sloping face of an open strip coal mine. Griffiths et al. (2009) investigated the influence of cross-correlation between strength parameters (i.e. cohesion and friction angle) on the results of probabilistic slope stability analyses. Fenton and Griffiths (2003) and Cho and Park (2010) studied the influence of cross-correlation between cohesion and friction angle on the bearing capacity

of a foundation soil layer beneath a strip footing. Zhang et al. (2005) considered the cross-correlation between different unsaturated hydraulic parameters (i.e. θ_s, α, n and k_{sat}) in seepage analyses. However, they did not explicitly show the effect of the cross-correlation on the final results. Arnold and Hicks (2011) cross-correlated hydraulic and strength parameters in RFEM analyses of rainfall-induced slope failure.

2.4. Inverse analysis in geotechnical engineering

In the 1980s, Cividini et al. (1983) made use of the displacements of a foundation to back calculate the elastic modulus of the founding soil layer. The authors used both a deterministic method, i.e. the least-squares method, and a statistical method, i.e. the Bayesian approach. Gioda and Sakurai (1987) studied the use of both deterministic and probabilistic methods in back analyses and their application to different geotechnical problems. Honjo et al. (1994) implemented the extended Bayesian method, which can adjust the importance of prior information in the estimation process, for an embankment on soft clay. Ledesma et al. (1996b) briefly introduced four commonly used methods of inverse analysis; namely, the least-squares method, the maximum likelihood method, the Bayesian method and the Kalman filter (KF) approach. Ledesma et al. (1996a) and Gens et al. (1996) implemented the maximum likelihood method for a hypothetical tunnel excavation problem. The authors combined this method with the finite element method to back-calculate the Young's modulus. Lee and Kim (1999) used the extended Bayesian method in tunnelling engineering and tried to back calculate four parameters, i.e. the elastic modulus, the initial horizontal stress coefficient at rest, the cohesion and the internal friction angle. Zhou et al. (2007) proposed a modified extended Bayesian method in the estimation of the Young's modulus for a three-layered embankment.

Kalman (1960) published the so-called KF, in which he described a recursive solution to the discrete data linear filtering problem. The KF was initially used to better estimate a set of state variables and uncertainties based on observations. The method takes account of the observed error and utlises the Kalman gain to update the values. The Kalman gain is a function of the covariance between the variables and the measurements. Later, in order to solve problems involving a nonlinear relationship between the state variables and measurements, the extended Kalman filter (EKF) was developed. The only difference between the KF and EKF is that the EKF linearises the relationship.

Bolzon et al. (2002) applied the EKF in the stochastic identification of the material parameters which govern a cohesive discrete-crack model. Yang et al. (2011b) made use of the EKF and observations in a tunnel to back analyse the natural stress in a rock mass.

Evensen (1994) published a paper which proposed a variant of the traditional KF called the EnKF, which resolved the identified disadvantages which existed in EKF. The first disadvantage was the use of the approximate closure scheme in the EKF, i.e. the linearisation of the function which links state variables and measurements together. The other problem was the significant computational requirements associated with the storage and forward integration of the state error covariance

matrix (Evensen, 2003, 2009). The EnKF addresses these by utilising an ensemble of forward models (i.e. many different calculations with different but statistically equal input parameters) to calculate the covariance model. This method has been widely used in meteorology and oceanography, such as in weather forecasting and navigation (Zheng et al., 2010). Burgers et al. (1998) discussed an analysis scheme using EnKF and compared two different cases, with and without perturbations in the observations, to illustrate the importance of using random perturbations in observations. For applications in engineering, Hommels et al. (2005) used the EnKF combined with the finite element method to conduct inverse analysis of the stiffness of an embankment located on a layered foundation. Hommels and Molenkamp (2006) presented an inverse analysis of a 1D foundation problem by using the EnKF combined with RFEM. Krymskaya et al. (2009) applied a variant, referred to as the iterative EnKF, in a history matching analysis in reservoir engineering. Hommels et al. (2001) pointed out a major advantage of using EnKF, i.e. it is not necessary to have access to the source code of a (finite element) program to implement EnKF.

In geotechnical engineering, measurements of pore water pressure (PWP) have rarely been used in the back analysis of seepage problems. Zhang et al. (2013) applied the Bayesian method to back calculate hydraulic parameters by utilising the measurements of PWP and investigated the effect of uncertainty in the hydraulic parameters on the prediction of rainfall infiltration; however, although the slope stability was influenced by the prediction of rainfall infiltration, the spatial variability of the hydraulic parameters was not taken into account. In hydrology, it has been shown that EnKF has been able to improve the estimation of hydraulic parameters based on the measurements of PWP. Chen and Zhang (2006) applied the EnKF in a transient 2D model of saturated flow and showed that the EnKF can improve the estimation of the local variability of hydraulic conductivity based on the pore pressure head. Xu et al. (2013) combined the EnKF with parallel computation and tested this new strategy in a 3D transient saturated groundwater flow analysis.

2.5. Conclusions

Soil variability can be large and causes wide uncertainties in geotechnical reliability analyses. Previous research has shown that inverse analysis can be a useful tool to improve the precision of soil parameters based on measurements. Firstly, it can improve the estimation of the distribution of soil parameters, e.g. the mean and standard deviation. Then, the improved estimation of the soil parameter statistics can improve the stochastic analysis of the boundary value problem. Research has applied inverse analysis in geotechnical engineering by using displacements, stresses or strains. However, the PWP has rarely been used in inverse analysis, especially in geotechnical engineering. In addition, the influence of cross-correlation between the hydraulic and mechanical parameters on slope stability has so far recieved little attention.

3

Reduction of Slope Stability Uncertainty Based on Hydraulic Measurement via Inverse Analysis

The determination of slope stability for existing slopes is challenging, partly due to the spatial variability of soils. Reliability-based design can incorporate uncertainties and yield probabilities of slope failure. Field measurements can be utilised to constrain probabilistic analyses, thereby reducing uncertainties and generally reducing the calculated probabilities of failure. A method to utilise pore pressure measurements, to first reduce the spatial uncertainty of hydraulic conductivity, by using inverse analysis linked to the ensemble Kalman filter, is presented. Subsequently, the hydraulic conductivity has been utilised to constrain uncertainty in strength parameters, usually leading to an increase in the calculated slope reliability.

This chapter has been published in *Georisk: Assessment and Management of Risk for Engineered Systems and Geohazards*, 10(3): 223-240 (2016) (Vardon et al., 2016). Kang Liu, the second author, contributed significantly to this paper, in particular, contributing to the initial theoretical development, and was responsible for the implementation and investigation of performance.

3.1. Introduction

Conventional methods for the determination of slope stability are deterministic, with soil properties characterised as constants for a given soil layer. The results tend to be expressed as a single number; that is, by a FOS (Fredlund and Krahn, 1977; Griffiths and Lane, 1999). However, natural soils are highly variable and heterogeneous (Phoon and Kulhawy, 1999). The limitations of deterministic methods, which do not explicitly account for variability and uncertainty related to soil parameters, have been highlighted, for example, by Vanmarcke (1977), Gui et al. (2000) and Cho (2007), and it has been shown that they can over- or underpredict the true FOS.

Reliability-based methods for geotechnical applications have been developing since the 1970s; from simpler methods such as the first order second moment method, first order reliability method (Hasofer and Lind, 1974) and point estimate method (Rosenblueth, 1975), to more complex methods such as RFEM (Griffiths and Fenton, 1993). In RFEM, random fields of spatially varying soil properties are linked with finite elements within a Monte Carlo simulation. Such analyses require a knowledge of the distributions of the soil parameter values, including the scale of fluctuation, which is the distance over which variables are significantly correlated (Fenton and Vanmarcke, 1990). These data can be derived from field tests (e.g. cone penetration tests (CPTs) and piezometers), laboratory tests and previous experience. However, the overall distribution of soil parameters is a general description of soil parameter variability, whereas, if the local variability was captured better, the overall uncertainty could be reduced (Lloret-Cabot et al., 2012).

In geotechnical engineering, many projects are equipped with tools to monitor the project performance, for example, through measurements of displacement, strain, pore pressure and so on. These measurements cannot be directly incorporated into conditional random fields to reduce the uncertainty of soil parameters, as they measure system responses and not soil properties. However, a general way to make use of these measurements is inverse analysis, which can be used to back-calculate the soil parameters (e.g. Cividini et al., 1983; Gens et al., 1996; Honjo et al., 1994; Ledesma et al., 1996a).

Honjo et al. (1994) indicated that inverse analysis methods can generally be categorized into two types: direct methods and indirect methods. Direct methods need to build a unique explicit relationship between parameters and measurements, so that the relationship can be inverted. However, due to the complexity of most engineering problems, it is virtually impossible to build such a relationship. Indirect methods are iterative procedures and make use of the forward relationship between parameters and measurements.

A number of indirect methods exist. These include the maximum likelihood method, which considers the measurements as random quantities and estimates a set of parameters which are statistically the most likely, that is, to maximise the probability of achieving the measured data; and Bayesian methods, which consider the parameters to be random and the distribution of parameters which are able to produce the measured data are estimated. The KF is a scheme which uses ongoing measurements to better estimate parametric inputs. In the case of the EnKF,

an ensemble of potential parameters is used, making it a variant of the Bayesian approach (Ledesma et al., 1996b).

Ledesma et al. (1996b) and Gens et al. (1996) implemented the maximum likelihood method in a synthetic problem of tunnel excavation. The authors combined this method with the FEM to back-calculate Young's modulus. Wang et al. (2013, 2014) utilised the maximum likelihood method in analysing a slope failure and an excavation, respectively, to improve the estimation of soil parameters based on field measurements such as slip surface inclination and ground settlement. The application of the maximum likelihood method was found to better explain the slope failure mechanism and also the prediction of wall and ground responses in the staged excavation.

Lee and Kim (1999) used the extended Bayesian method in tunnelling engineering and tried to back-calculate four parameters, that is, the elastic modulus, the initial horizontal stress coefficient at rest, the cohesion and the internal friction angle. Zhou et al. (2007) proposed a modified extended Bayesian method in the estimation of the Young's modulus for a three-layered embankment. Papaioannou and Straub (2012) utilised Bayesian updating to improve the estimation of the reliability of an excavation, with a sheet pile retaining wall, in sand, based on non-linear deformation measurements. Zhang et al. (2013) applied the Bayesian method to back-calculate hydraulic parameters by utilising measurements of pore water pressure and investigated the effect of uncertainties in the hydraulic parameters on the prediction of slope stability, but without considering the spatial variability of hydraulic parameters. Zhang et al. (2014) further investigated the effect of measurement data duration and frequency in the Bayesian updating of hydraulic parameters.

Kalman (1960) developed the KF, which was initially used to estimate a set of variables and uncertainties and, based on a set of observations, improve the estimation. Later a number of variants were developed, such as the EKF and the EnKF. The EnKF requires no linearisation when updating state variables which are governed by a non-linear relationship, in contrast to the EKF. Hommels et al. (2005) and Hommels and Molenkamp (2006) utilised the EnKF and observations of settlements to improve the estimation of Young's modulus. Yang et al. (2011b) made use of the EKF and observations of displacement in a tunnel to back-analyse the natural stress in the rock mass.

The majority of the inverse analysis methods given above only made use of direct measurements which were directly related to the undetermined parameters. For example, the measurements used in Chen and Zhang (2006) were pressure head, so the corresponding uncertain parameter was hydraulic conductivity. In Hommels and Molenkamp (2006), the parameter and measurement were stiffness and settlement, respectively. This limits the choice of information which could contribute to the determination of parameters, although, as the underlying differences in material behaviour come from, in general, differences in composition, stress state or stress history, it is likely that material parameters are correlated (Nguyen and Chowdhury, 1985; Ching and Phoon, 2013). Fenton and Griffiths (2003) and Cho and Park (2010) studied the influence of cross-correlation between cohesion and

friction angle on the bearing capacity of a strip foundation. Griffiths et al. (2009) investigated the influence of cross-correlation between Mohr–Coulomb strength parameters (i.e. cohesion and friction angle) in probabilistic analyses of slope stability. Zhang et al. (2005) considered the cross-correlation between different unsaturated hydraulic parameters in seepage analysis, and Arnold and Hicks (2011) considered the cross-correlation of hydraulic and strength parameters in stochastic analyses of rainfall-induced slope failure.

In this chapter, a theoretical study of the uncertainty in the factor of safety (with respect to the stability) of embankment slopes under steady-state seepage conditions is presented. The work takes advantage of the fact that instrumentation is often available in geotechnical projects, but also that, in soils, pore pressure measurements are cheaper, easier to install and more reliable than stress/strain measurements. In addition, it takes account of the cross-correlation between material properties; specifically, it proposes that the hydraulic conductivity, cohesion and friction angle are cross-correlated. Therefore, the pore pressure measurements can be used to reduce the uncertainty in the slope stability, via more accurate effective stress and shear strength estimations. The proposed method first utilises the EnKF inverse analysis method to better determine the hydraulic conductivity field; then the cohesion and friction angle are cross-correlated with hydraulic conductivity so that the estimation of slope stability can be improved.

The purpose of this chapter is to present, demonstrate and evaluate the robustness of the new method within a controlled (albeit simplified) environment. This has been facilitated by the use of synthetic (i.e. numerically generated) "measurements", so that full knowledge of the solution is available and the results can be properly tested. First the method is presented, and this is followed by a series of analyses to examine the effects of the various parameters on the overall calculated uncertainty. These results will be used to guide future studies involving real field situations.

3.2. Framework and theoretical formulation

3.2.1. Framework of the overall analysis

The framework of the proposed numerical approach is shown in Figure 3.1. The flow chart shows that it can be split into two parts: inverse and forward analyses. Inverse analysis is possible where there are measurements available, that is, pore pressures in this chapter. Synthetic data have here been used to provide a fully known solution against which the method can be tested, and are sampled to provide a proxy for real measurements. In the remainder of the chapter, these sampled data are referred to as "synthetic measurements".

The analysis starts with an estimation of the hydraulic conductivity in the field, which is the distribution of hydraulic conductivity characterised by its mean, standard deviation and scales of fluctuation. Based on this statistical characterisation of the hydraulic conductivity an RFEM analysis can be undertaken, whereby multiple realisations of the hydraulic conductivity field are generated and analysed to give a distribution of computed pore water pressure fields. Then, via the EnKF, the

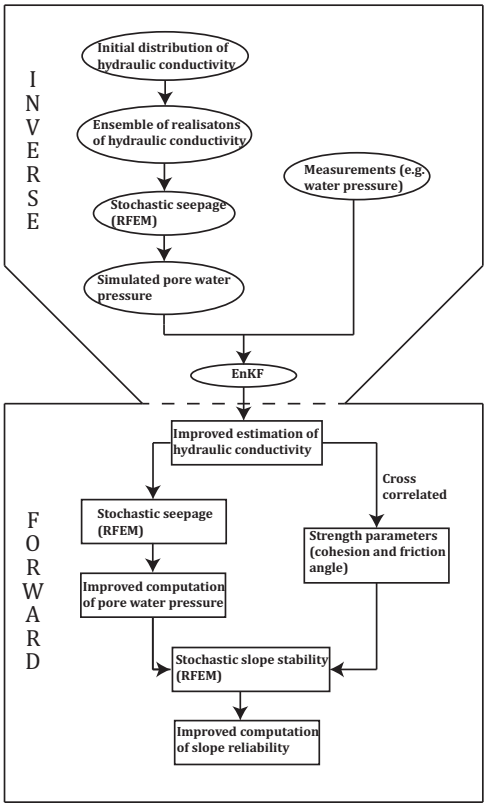

Figure 3.1: Flowchart of the numerical approach.

ensemble of realisations are compared to the synthetic measurements, so that the estimation of the hydraulic conductivity field can be updated/improved.

The forward analysis benefits from the output of the preceding inverse analysis. The updated hydraulic conductivity field improves the computed pore pressure field, which in turn affects the effective stress field. In addition, by using the cross-correlation between the hydraulic conductivity and strength parameters, the strength parameters can also be updated. Another RFEM analysis is then carried out, this time to obtain a probabilistic description of the slope stability. However, the EnKF method cannot be used to update the slope stability, as the shear strength cannot be easily/directly measured in a non-destructive way. The improvements achieved during the inverse and forward analysis stages, that is, with respect to pore water pressure and strength parameters, cause a reduction in the uncertainty in the calculated FOS of the slope.

In order to facilitate the understanding and evaluation of the model, in the analyses in Section 3.3 the following simplifications were adopted: (i) a one-directional coupled analysis; (ii) no flow in the unsaturated zone; (iii) linear elastic, perfectly plastic constitutive behaviour, with a Mohr–Coulomb failure surface; and (iv) steady-

state seepage.

3.2.2. Slope stability under seepage conditions

In this chapter, a one-way coupled slope stability analysis has been undertaken. First, the pore pressure distribution due to steady-state seepage has been analysed; next, the influence of the pore pressure distribution has been incorporated in the slope stability analysis.

Steady state seepage

The governing mass conservation equation for steady-state saturated groundwater flow in 2D is utilised, with the deformation of the domain and compressibility of water being neglected. Therefore, the governing equation is (Smith et al., 2013)

$$\frac{\partial}{\partial x}\left(k_x \frac{\partial h}{\partial x}\right) + \frac{\partial}{\partial y}\left(k_y \frac{\partial h}{\partial y}\right) = 0 \tag{3.1}$$

where $h = z + p/\gamma_w$ is the hydraulic head, in which z is the elevation, p is the pore pressure and γ_w is the unit weight of water, and k_x and k_y are the hydraulic conductivity in the x and y directions, respectively.

Over the domain, the hydraulic conductivity is taken as a spatially random variable so that a stochastic seepage analysis can be undertaken.The hydraulic conductivity is lognormally distributed (Griffiths and Fenton, 1993) and RFEM is applied to incorporate the uncertainty existing in the hydraulic conductivity. Griffiths and Fenton (1993) first applied RFEM to stochastic seepage in the foundation of a water retaining structure. Since then, a series of stochastic seepage studies have been undertaken using this method. Some have focused on the seepage itself (Fenton and Griffiths, 1996), whereas others have studied the influence of stochastic seepage on slope or embankment stability (Le et al., 2012). RFEM is the combination of LAS, to create "random fields" of material parameters, FEM and MCM. Generally speaking, the stochastic seepage simulation can be realized in three steps. Firstly, LAS is used to generate a random field of hydraulic conductivity based on the statistical values of hydraulic conductivity, i.e. the mean μ_k and standard deviation σ_k, and the scale of fluctuation θ_k reflecting the spatial correlation of hydraulic conductivity at different locations. Then, FEM is used to compute the pore pressure, seepage velocity, etc. Finally, the process is repeated multiple times as part of a MC simulation (Hicks and Samy, 2004).

In this study, a fixed FE mesh is used to solve Equation 3.1, and also prescribed hydraulic head (Drichlet) boundary conditions. However, in this saturated unconfined flow problem there are initially unknown boundary conditions, which are the position of the phreatic surface and the exit point on the downstream surface of the embankment. During the computation, an iterative process is adopted to determine the exact positions of the exit point and phreatic surface (Chapuis and Aubertin, 2001; Chapuis et al., 2001). An outer iteration loop is used to determine the position of the exit point and an inner iteration loop is used to determine the position of the phreatic surface. The outer iteration stops when the nodes on the downstream surface of the embankment which are above the exit point have no

positive pore water pressure. The inner iteration stops when the hydraulic head at every node converges.

In the fixed mesh method, the hydraulic conductivity at each Guass point in the domain is modelled based on its pore pressure p. When $p \geq 0$, the hydraulic conductivity is equal to k and, when $p < 0$, the hydraulic conductivity is zero (Bathe and Khoshgoftaar, 1979). Hence, the elements in the dry region are effectively removed from the computation and those in the wet region are still active.

Slope stability

The slope stability analysis uses the results of the previous seepage analysis to define the pore water pressure, in order to generate the effective stress field. The effective stress vector $\boldsymbol{\sigma}' = [\sigma_x' \ \sigma_y' \ \tau_{xy} \ \sigma_z']^{\mathrm{T}}$ can be expressed as

$$\boldsymbol{\sigma}' = \boldsymbol{\sigma} - p\mathbf{m} \tag{3.2}$$

where $\boldsymbol{\sigma}$ is total stress vector generated by the gravitational load, $\mathbf{m} = [1, \ 1, \ 0, \ 1]^{\mathrm{T}}$ for 2D plane strain analysis and p is the pore water pressure.

The slope stability analysis considers an elastic, perfectly plastic soil with the Mohr–Coulomb failure criterion (e.g. Smith et al., 2013) and the FOS of the slope is computed using the strength reduction method (Griffiths and Lane, 1999), that is:

$$c_f' = c'/\mathrm{FOS} \tag{3.3}$$

$$\phi_f' = \arctan\left(\frac{\tan\phi'}{\mathrm{FOS}}\right) \tag{3.4}$$

where c' and ϕ' are the effective cohesion and friction angle, and c_f' and ϕ_f' are the respective factored shear strength parameters corresponding to slope failure.

3.2.3. Stochastic FE analysis

Due to the spatial variability of the soil parameters, FEM is combined with random field theory within a stochastic (Monte Carlo) process. This involves multiple simulations (i.e. realisations) of the same problem, a procedure often referred to as RFEM (Griffiths and Fenton, 1993). In each realisation of an RFEM analysis, a random field of material properties is generated, based on the point and spatial statistics of the material properties. RFEM has proved to be an efficient approach for conducting stochastic slope stability analyses (e.g. Hicks and Samy, 2002b, 2004).

Random field generation for single variable

LAS (Fenton and Vanmarcke, 1990) has been applied to generate the random fields. This method generates standard normal fields, in which the spatial variation of property values is related to a correlation function incorporating the scale of fluctuation. The standard normal field is then transformed to the appropriate distribution based

on the mean and standard deviation of the variable being modelled, and also post-processed to account for different scales of fluctuation in different directions (Hicks and Samy, 2004).

For the application in this chapter, as the distribution of hydraulic conductivity is usually considered to be log-normal (Griffiths and Fenton, 1993; Zhu et al., 2013), the natural log of hydraulic conductivity, $\ln(k)$, follows a normal distribution. Hence the standard normal random field is transformed into a normal field of $\ln(k)$. An exponential Markov correlation function has been used to build the covariance function relating the spatial correlation between the variable values at different locations, that is:

$$\rho(\tau) = \exp\left(-\frac{2}{\theta_{\ln k}}\tau\right) \tag{3.5}$$

where τ is the lag distance between two points in a random field, and $\theta_{\ln k}$ is the scale of fluctuation of $\ln k$. Fenton and Griffiths (2008) indicated that $\theta_{\ln k} \approx \theta_k$ (where θ_k is the scale of fluctuation of k), and this relationship has been adopted in this chapter.

Random field generation for multiple variables

In this chapter, three variables are spatially random, that is, hydraulic conductivity, cohesion and friction angle. The chapter makes use of the inter-dependence between these parameters (Nguyen and Chowdhury, 1985) to cross-correlate the random fields. Cross-correlated parameters are first transformed into standard normal space and the dependence between the parameters is defined via a correlation matrix (Fenton and Griffiths, 2003),

$$\rho = \begin{bmatrix} 1 & \rho_{\ln k,c} & \rho_{\ln k,\phi} \\ \rho_{\ln k,c} & 1 & \rho_{c,\phi} \\ \rho_{\ln k,\phi} & \rho_{c,\phi} & 1 \end{bmatrix} \tag{3.6}$$

where ρ represents the correlation (in standard normal space) between the parameters identified by the first and second subscripts. The matrix is decomposed by Cholesky decomposition, that is, $\boldsymbol{\rho} = \mathbf{L}\mathbf{L}^{\mathrm{T}}$, and used to generate correlated random field values from initially uncorrelated random field values, via:

$$\mathbf{G}_{depend} = \mathbf{L}\mathbf{g}_{independ} \tag{3.7}$$

$$\begin{bmatrix} G_{\ln k} \\ G_c \\ G_\phi \end{bmatrix}_{depend} = \mathbf{L}\begin{bmatrix} g_{\ln k} \\ g_c \\ g_\phi \end{bmatrix}_{independ} \tag{3.8}$$

where $\mathbf{G}_{depend}$ is a vector of correlated values and $\mathbf{g}_{independ}$ is a vector of uncorrelated values.

3.2.4. Inverse analysis via the EnKF

Evensen (1994) proposed the EnKF based on the traditional KF (Kalman, 1960), to reduce parameter uncertainty based upon measured data. In this chapter, the EnKF is linked to the random field approach to better capture the local variability of hydraulic conductivity. In the approach of Evensen (1994) the measurements are time dependent, but here the measured data are fixed in time and hence the EnKF has been used independent of time.

Herein, the EnKF follows an iterative process, in which each iteration contains two steps: forecast and update. For applying the EnKF to stochastic seepage, a state vector has to be constructed to incorporate both the unknown local hydraulic conductivities and measurements of hydraulic head. This is expressed as:

$$\mathbf{x}_i = \begin{pmatrix} \mathbf{k} \\ \mathbf{h} \end{pmatrix} = \begin{pmatrix} (\ln(k_1) & \ln(k_1) & \cdots & \ln(k_{N_k}))^{\mathrm{T}} \\ (h_1 & h_2 & \cdots & h_m)^{\mathrm{T}} \end{pmatrix} \tag{3.9}$$

where subscript i represents an ensemble; $\mathbf{k}$ is the vector of logarithmic hydraulic conductivity, $\ln(k)$, as the EnKF can only be applied to normally distributed variables (Chen and Zhang, 2006); $\mathbf{h}$ is the vector of hydraulic heads computed at the measurement locations; and N_k and m are the number of unknown hydraulic conductivity values and hydraulic head measurements, respectively. In this case, the number of unknown hydraulic conductivity values is equal to the number of Gauss points in the foundation of the FE mesh. In the EnKF, an ensemble of N state vectors is used to simulate the initial estimation of the hydraulic conductivity field, that is, $\mathbf{x} = (\mathbf{x}_1, \mathbf{x}_2, \cdots, \mathbf{x}_N)$.

In the forecasting step of each iteration, the ensemble of state vectors is forecasted to the second (i.e. update) step by the model describing the problem, that is, $\mathbf{x}_t = \mathrm{F}(\mathbf{x}_{t-1})$, where t is the iteration number in the EnKF. In this case, the seepage model is utilised to compute the hydraulic heads for all realisations of the ensemble, based on the updated hydraulic conductivity fields from the end of the previous iteration.

After the forecasting step, the computed hydraulic heads at the measurement locations in the forecasted ensemble of state vectors are compared with the collected "real" hydraulic head measurements. The ensemble of state vectors is then updated (with respect to hydraulic conductivity) by

$$\mathbf{x}_t^u = \mathbf{x}_t^f + \mathbf{K_G}(\mathbf{D} - \mathbf{H}\mathbf{x}_t^f) \tag{3.10}$$

$$\mathbf{D} = (\mathbf{h}_1, \mathbf{h}_2, \cdots, \mathbf{h}_N) \tag{3.11}$$

$$\mathbf{h}_i = \mathbf{h}^* + \boldsymbol{\epsilon}_i \tag{3.12}$$

where $\mathbf{x}_t^u$ is the matrix containing the ensemble of updated state vectors, of dimensions $(m + N_k) \times N$, and $\mathbf{x}_t^f$ is the corresponding matrix of state vectors resulting from the forecasting step; $\mathbf{D}$ is the matrix of measurement data perturbed by noise, of dimensions $m \times N$; $\mathbf{h}_i$ is a vector of perturbed measurements; $\mathbf{h}^*$ is the vector

of real measurements; and $\boldsymbol{\epsilon}_i$ is a vector of measurement errors added to the real measurements in order to create perturbed measurements. Each element in the error vector $\boldsymbol{\epsilon}_i$ is randomly selected from a normal distribution with a zero mean and a variance defined by the input measurement error. Here, $\mathbf{R}$ is a matrix based on $\boldsymbol{\epsilon}_i$, that is:

$$\mathbf{R} = \frac{\mathbf{e}\mathbf{e}^{\mathrm{T}}}{N-1} \tag{3.13}$$

$$\mathbf{e} = (\boldsymbol{\epsilon}_1, \boldsymbol{\epsilon}_2, \cdots, \boldsymbol{\epsilon}_N) \tag{3.14}$$

Also, with reference to equation 3.10, $\mathbf{H}$ is the measurement operator which relates the state vector to the measurement points; it is in the form of $\mathbf{H} = [\mathbf{0} \mid \mathbf{I}]$, where $\mathbf{0}$ is an $m \times N_k$ null matrix and $\mathbf{I}$ is an $m \times m$ identity matrix. $\mathbf{K_G}$ is the Kalman gain derived from the minimization of the posterior error covariance of the ensemble of state vectors, that is:

$$\mathbf{K_G} = \mathbf{P}_t^f \mathbf{H}^{\mathrm{T}} (\mathbf{H}\mathbf{P}_t^f \mathbf{H}^{\mathrm{T}} + \mathbf{R})^{-1} \tag{3.15}$$

$$\mathbf{P}_t^f = \frac{1}{N-1} (\mathbf{x}_t^f - \overline{\mathbf{x}}_t^f)(\mathbf{x}_t^f - \overline{\mathbf{x}}_t^f)^{\mathrm{T}} \tag{3.16}$$

where $\mathbf{P}_t^f$ is the error covariance matrix of the ensemble of forecasted state vectors, and $\overline{\mathbf{x}}_t^f$ is the ensemble mean of $\mathbf{x}_t^f$, that is, $\overline{\mathbf{x}}_t^f = \mathbf{x}_t^f \mathbf{1}_N$, where $\mathbf{1}_N$ is a matrix in which each element is equal to $1/N$.

At the end of the iteration process, the ensemble mean is considered to be the best estimate of the hydraulic conductivity field, and the pore pressures generated using this result are passed to the slope stability analysis in Section 3.2.2 and utilised to generate correlated strength parameters in Section 3.2.3. The implementation of this aspect is undertaken utilising the subroutine found in Section 5 of Evensen (2003).

3.3. Model performance

In this section, an illustrative example is presented, to show how the proposed approach can affect the uncertainty in the calculated slope stability via the use of only hydraulic measurement data.

Figure 3.2 shows the geometry of an embankment overlying a foundation. The embankment is 4 m high, with upstream and downstream side slopes of $1{:}2$. It is 4 m wide at the crown and 20 m wide at its base. The upstream water level is 4 m above the base of the embankment and the downstream water level is at 0 m. The soil foundation is 40 m wide and 5 m deep, and the lateral and bottom boundaries of the foundation are assumed to be impermeable.

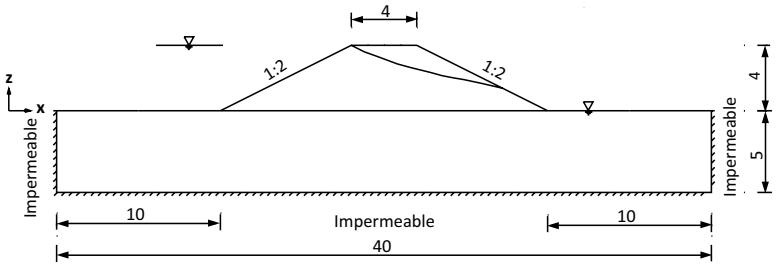

Figure 3.2: Geometry of the embankment and foundation (dimensions in m).

3.3.1. Application of EnKF in stochastic seepage

Results

As previously stated, the results of an arbitrary realisation have been selected to represent the actual spatial variability of hydraulic conductivity at the site, which means that the hydraulic conductivity is known at all points, that is, in contrast to a real situation where it would not be known everywhere. In the analysis, the embankment is assumed to be homogeneous, whereas the foundation is heterogeneous. This is for simplicity, to enable a better understanding of the performance of the model. Moreover, the hydraulic conductivity is assumed to be isotropic, that is, the same in the vertical and horizontal directions, again for simplicity. The FE mesh size is 1.0 by 1.0 m, as shown in Figure 3.5(e), and the elements are 4-noded bi-linear elements with four Gaussian integration points. The cell size in the random field is 0.5 by 0.5 m, which means that each of the four integration points are assigned a different cell value from the random field. Hence 800 hydraulic conductivity values are generated in the foundation layer for the inverse analysis.

Initially 500 realisations were generated for the ensemble. The mean and standard deviation (log-normal distribution) of the hydraulic conductivity for the random field generation were both selected to be 10^{-6} $\mathrm{m/s}$. The scale of fluctuation was selected to be anisotropic (Lloret-Cabot et al., 2014) and within realistic bounds, with the vertical and horizontal scales of fluctuation for the foundation being 1.0 and 8.0 m, respectively (Hicks and Onisiphorou, 2005; Firouzianbandpey et al., 2014; Cho and Park, 2010; Suchomel and Mašín, 2010). It is anticipated that these initial values can be estimated from laboratory tests, or soil databases, where sufficient similar material is available. Such tests have previously been utilised to generate input statistics for RFEM analyses or parameter variations in parametric FEM analyses. Moreover, the initial estimated scale of fluctuation and degree of anisotropy of the heterogeneity could be estimated from CPT data (e.g. Lloret-Cabot et al., 2014).

The realisation selected to provide the measured data is shown in Figure 3.3(a), with the discrete nature of the hydraulic conductivity values in the figure being due to single values being assigned to each Gauss point. Figure 3.3(b) shows that the initial estimate, based on the mean of 500 realisations, approximates to the input mean of $k = 10^{-6}$ $\mathrm{m/s}$. Figures 3.4(a) and 3.4(b) show the error in the hydraulic head values, generated by the initial estimation of the hydraulic conductivity and

the updated hydraulic conductivity, respectively, that is:

$$\boldsymbol{\epsilon}_{initial} = \mathbf{h}_{initial} - \mathbf{h}_{reference} \tag{3.17}$$

$$\boldsymbol{\epsilon}_{updated} = \mathbf{h}_{updated} - \mathbf{h}_{reference} \tag{3.18}$$

where $\boldsymbol{\epsilon}_{initial}$ and $\boldsymbol{\epsilon}_{updated}$ are the initial and updated errors in hydraulic head, respectively, and $\mathbf{h}_{reference}$, $\mathbf{h}_{initial}$ and $\mathbf{h}_{updated}$ are the hydraulic heads calculated from the reference hydraulic conductivity field, and the initial and updated estimations of the hydraulic conductivity field, respectively. Figures 3.4 (c)–(e) show the reference, initial and the updated pore water head distributions. It is seen that the geometry of the system controls the overall shape of the distribution, with only relatively minor perturbations due to the heterogeneity. However, these perturbations are large enough (~ 0.3 m) to give more information on the local hydraulic conductivity distribution.

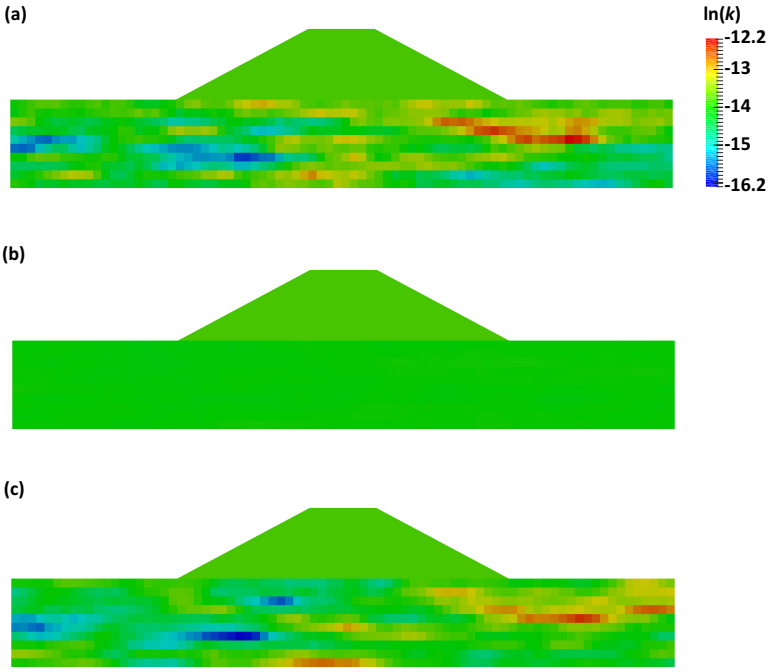

Figure 3.3: Initial and updated estimations of the logarithmic hydraulic conductivity, $\ln(k)$, field compared to the reference case (k in m/s): (a) reference field of $\ln(k)$ in the foundation; (b) initial estimation of $\ln(k)$ field (taken to be the mean of the ensemble) and (c) updated estimation of $\ln(k)$ field after inverse analysis (mean of the ensemble).

The number of synthetic measurements used in the analysis was first chosen to be 88, with the locations of the measuring points shown in Figure 3.5(a) as solid dots. Three further patterns of measuring points were also used, that is, 44 (Figure

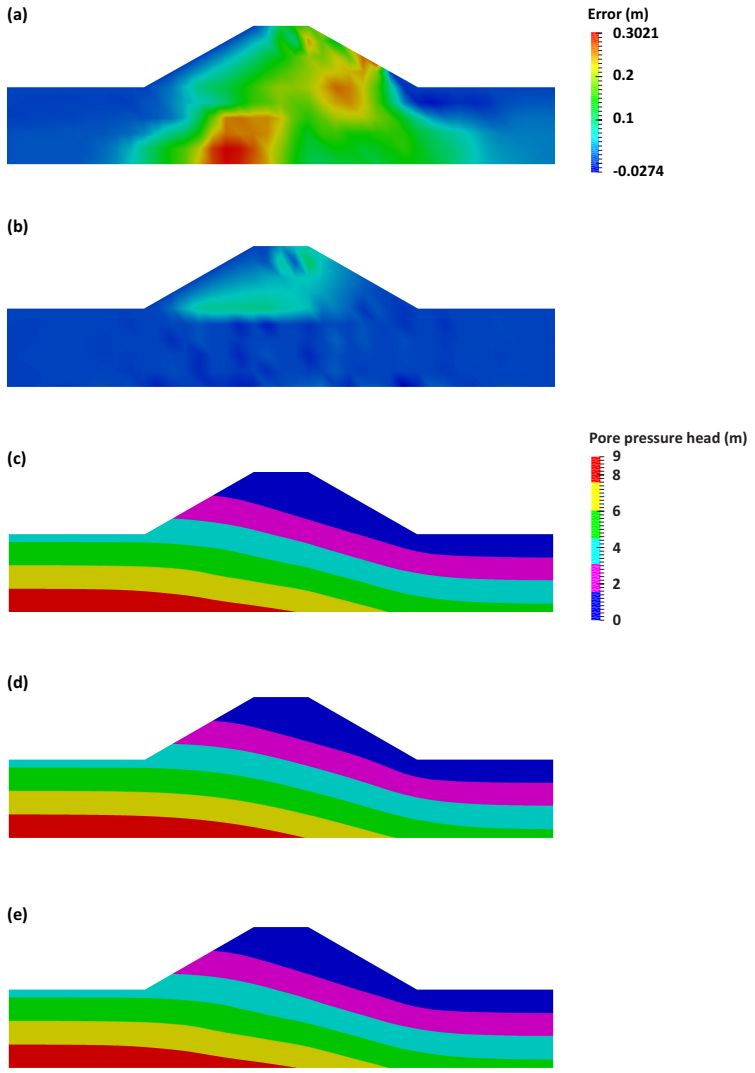

Figure 3.4: Error in hydraulic head (in meters) based on the initial and updated hydraulic conductivity fields relative to the reference hydraulic conductivity field: (a) error between reference and initial hydraulic conductivity fields; (b) error between reference and updated hydraulic conductivity fields; (c) reference pore pressure head field; (d) initial pore pressure head field and (e) updated field.

5(b)), 24 (Figure 3.5(c)) and 12 (Figure 3.5(d)) points, where the full column of synthetic measurements is used in each measurement configuration. The element and local Gauss point numbering are given in Figure 3.5(e). All monitoring points for the synthetic measurements have been located in the foundation, for two reasons: (i) for long term field measurements, ensuring that the points are saturated increases the reliability of the sensors; and (ii) the foundation of an embankment

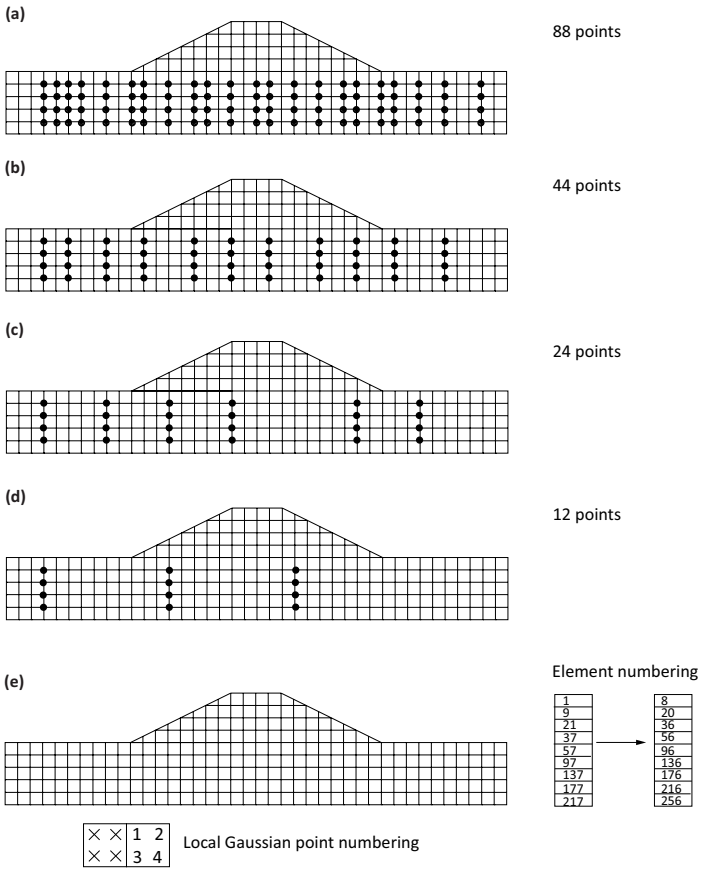

Figure 3.5: Locations of measuring points: (a) measurement point locations for 88 observation points; (b) measurement point locations for 44 observation points; (c) measurement point locations for 24 observation points; (d) measurement point locations for 12 observation points and (e) mesh, element and local Gauss point numbering.

is more likely to be highly heterogeneous.

Each element in $\boldsymbol{\epsilon}_i$ (equation 3.12) has been selected from a normal distribution, with a zero mean and a variance chosen to be 10^{-6} m^2, for the hydraulic head measurement. The variance is related to the precision of the measurement tools. A variance of 10^{-6} m^2 means that the accuracy of the synthetic measurements of hydraulic head are required to be ± 0.003 m (i.e. 3σ).

In this illustrative example, the authors use 50 iteration steps of the EnKF. The updated estimated hydraulic conductivity field (the average of the final updated values of the 500 ensemble members), arising from the EnKF results, is shown in Figure 3.3(c) and displays a clear local variability. The hydraulic head errors resulting from this updated field are small, as shown in Figure 3.4(b). Figure 3.6 shows the comparison between the 800 reference values of the local hydraulic

conductivity field, the initial estimation of the local hydraulic conductivity field and the updated estimate of the local hydraulic conductivity field, based on averaging the 500 ensemble members. Figures 3.6(a)–(c) shows the comparisons at the ends of iteration steps 1, 5 and 50, respectively, while the sequential numbering of the Gauss points used in Figures 3.6(a)–(c) is shown in terms of depth in Figure 3.6(d). It can be seen that the estimation of the local hydraulic conductivity field improved quickly. After 5 iterations, there is no significant change in the estimation.

Sensitivity analysis of EnKF

A sensitivity analysis has been undertaken to study the influence of various aspects. In order to evaluate the final results, the root mean square error (RMSE) of the hydraulic head has been used. This is defined as

$$\mathrm{RMSE} = \sqrt{\frac{1}{N_h}\sum_{ii=1}^{N_h}\left(h_{ii}^{t} - h_{ii}^{e}\right)^2} \tag{3.19}$$

where N_h is either the number of unknown hydraulic head values in the foundation layer (i.e. the total number of nodes in the foundation), or the number of measurement points (i.e. m), and superscripts t and e represent the true and estimated values, respectively. The lower the RMSE, the better the result. For this analysis the hydraulic conductivity, although being the variable updated, has not been used in the RMSE calculation due to the steady state calculations used. Specifically, due to the steady state nature of the simulations, the results of the hydraulic conductivity are not unique; only the relative differences between the hydraulic conductivities at different points are. Hence, it is the hydraulic head values which have been used and optimised in the EnKF.

Measurement error. Figure 3.7 shows the RMSE resulting from different measurement error variances. The solid lines represent the RMSE values when only the measurement points are taken into account, whereas the dotted lines include all of the unknown hydraulic head values in the foundation layer. In all cases, the size of the ensemble was 500 members. Considering the RMSE for only the measured points, the error is generally seen to reduce with each iteration step. When the input variance of the measurement error is equal to or lower than 10^{-6} m^2, the RMSE for the measured points reduces to almost zero and has therefore been used in the further analyses presented in this chapter. This clearly illustrates that the method is able to optimise the results based upon the measured data. Considering the RMSE for all the unknown hydraulic head values, in all cases the RMSE initially reduces before converging. Note that, in this method, for each iteration of the EnKF a different ensemble of random errors ($\boldsymbol{\epsilon}_i$ from equation 3.12) was used. An alternative algorithm was also examined where the same random ensemble was used; however, with this algorithm, the results were found not to converge for larger values of the measurement error. It is seen that, where the measurement errors are small, the majority of the improvement occurs within 10 iteration steps. For larger errors convergence is slower, although the improvement continues with more iteration steps for all cases.

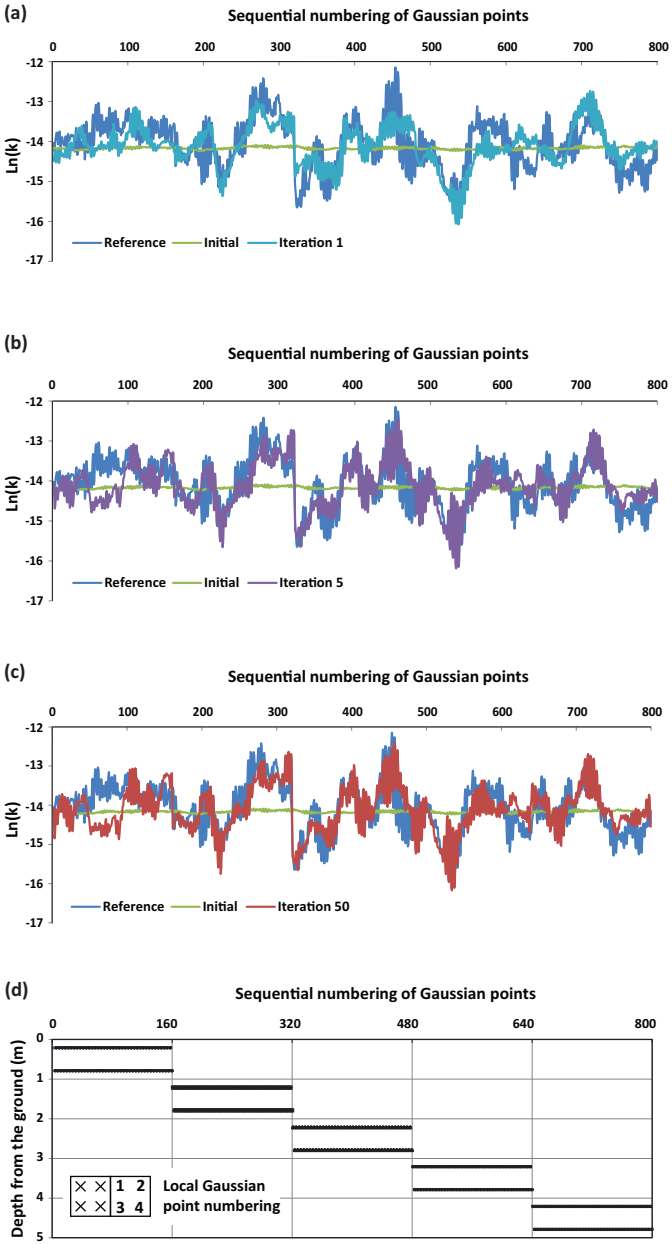

Figure 3.6: Comparison between the reference values, initial values and updated values of the local hydraulic conductivity at different EnKF iteration steps: (a) comparison at step 1; (b) comparison at step 5; (c) comparison at step 50 and (d) Gauss point numbering against depth.

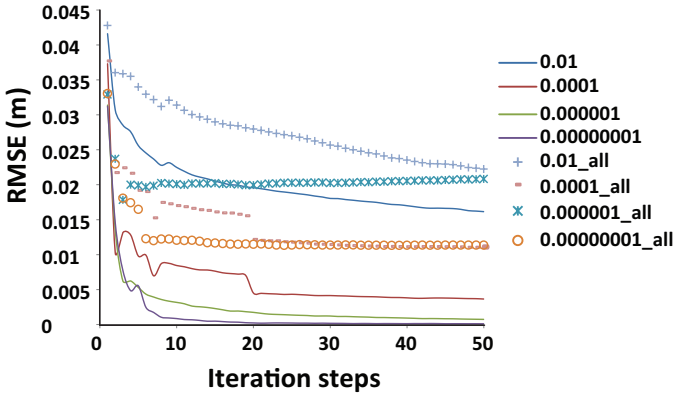

Figure 3.7: RMSE of hydraulic head for various input measurement error variances. Solid lines represent RMSE values with only the measurement points taken into account and the dotted lines include all of the unknown hydraulic head values in the foundation layer.

Ensemble size. Another important aspect of the EnKF is the size of the ensemble. Several cases with different sizes to see the influence have been analysed, although, in all cases, the input variance of the measurement error was 10^{-6} m^2. Figure 3.8 shows the RMSE for different ensemble sizes; once again, with the solid lines representing RMSE values based on only the measured points and the dotted lines for RMSE values based on all the unknown hydraulic head values in the foundation layer. Figure 3.8 shows that, when the size of the ensemble is too small (i.e. 200), the RMSE oscillates. It was found that, for the problem analysed, 500 ensemble members were sufficient, although for other problems this may not be the case.

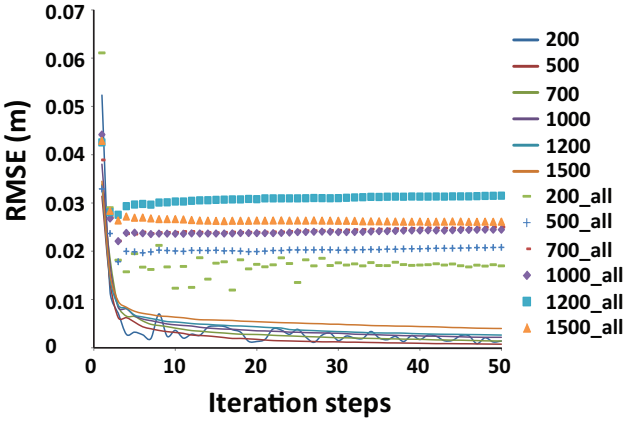

Figure 3.8: RMSE for different ensemble sizes.

3.3.2. Prediction of seepage uncertainty

Initially, there is only knowledge about the global distribution of hydraulic conductivity in the whole foundation and there is no information about the local variability of the hydraulic conductivity. Before the inverse analysis was applied, a stochastic seepage analysis was carried out to predict the seepage behaviour based on the global distribution of hydraulic conductivity.

Figure 3.9 shows the comparison of results from the stochastic seepage analysis before and after inverse analysis. It can be seen from Figure 3.9(a) that the range of inflows is reduced, which indicates an improvement in the estimation of the hydraulic conductivity. In Figure 3.9(b), it is seen that there is a significant change in the cumulative distribution function (CDF); in particular, an increase in the gradient indicates a reduction in the uncertainty. Note that, although the absolute values of the inflow are not important in this case, due to the steady state nature of the analyses, the reduction in uncertainty represents a much improved hydraulic conductivity field with respect to the local comparative variations.

3.3.3. Slope stability with improved seepage behaviour estimation

The improved prediction of pore water pressure in the foundation has been imported into the slope stability analysis. The slope stability has been computed based on the unimproved and improved pore pressure fields. The saturated unit weight of both the embankment and foundation is $20\ \mathrm{kN/m^3}$. The unsaturated unit weight of the embankment is $13\ \mathrm{kN/m^3}$. The Young's modulus and Poisson's ratio are $10^5\ \mathrm{kPa}$ and 0.3, respectively. The dilation angle is chosen to be zero, and so are the following chapters. The strength parameters (cohesion and friction angle) of the foundation follow truncated normal distributions (i.e. with any negative values discarded), whereas constant strength parameters are used for the embankment and these are selected to be equal to the mean values assumed for the foundation. The mean cohesion and friction angle are $10\ \mathrm{kPa}$ and 30^0, respectively. The coefficient of variation of cohesion is 0.2 (Arnold and Hicks, 2011) and the coefficient of variation of the friction angle is chosen to be 0.15 (Phoon and Kulhawy, 1999). The scale of fluctuation is related to the deposition process (Firouzianbandpey et al., 2014), so it is assumed that the scale of fluctuation of the cohesion and friction angle are equal to each other and also identical to the scale of fluctuation of the hydraulic conductivity. However, note that this assumption is not implicit to the method and that the method is also applicable to the case where different scales of fluctuation exist for different parameters. The cross-correlations are included using the method defined in Section 3.2.3.

Before the stochastic analysis of slope stability, a mesh convergence analysis was undertaken using the mean strength parameters. The FOS of the slope calculated by the strength reduction method for the mesh used here (element size of 1.0 by $1.0\ \mathrm{m}$) was 1.95 and a denser mesh discretization (element size of 0.5 by $0.5\ \mathrm{m}$) resulted in a calculated FOS of 1.97. Therefore, considering the balance between accuracy and efficiency, the mesh size of 1.0 by $1.0\ \mathrm{m}$ was considered suitable for this analysis. It should be noted that, as a non-associated (dilation angle of

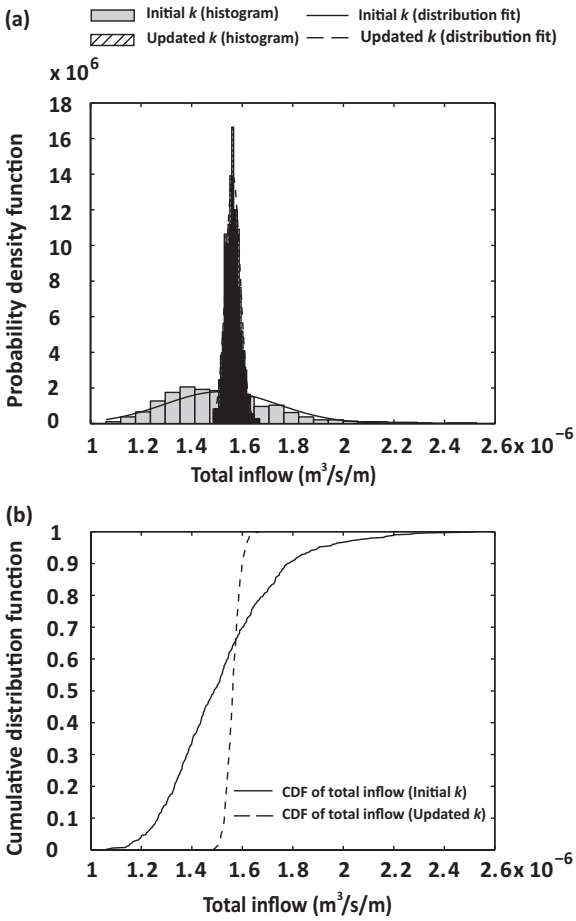

Figure 3.9: Probability distributions of the total inflow based on the initial and updated hydraulic conductivity fields, based on 500 realisations (ensemble members): (a) PDF of total inflow and (b) CDF of total inflow.

zero) elastic-perfectly-plastic Mohr–Coulomb model was used to represent the soil, there will be a degree of mesh dependence. This mesh dependence in FEM when using simple/complex constitutive models, which may be overcome by using (for example) non-standard continua, has been investigated by others, e.g. Conte et al. (2010); Tschuchnigg et al. (2015).

The distribution of FOS from the slope stability analysis without improvement of the pore pressure prediction, and for uncorrelated strength parameters, is shown in Figure 3.10 in light grey and approximated by a normal distribution. The distribution of FOS for the slope with the updated hydraulic conductivity (based on the measured data), for uncorrelated strength parameters, is shown hatched.

The mean and standard deviation of the FOS in the original case are 1.95 and

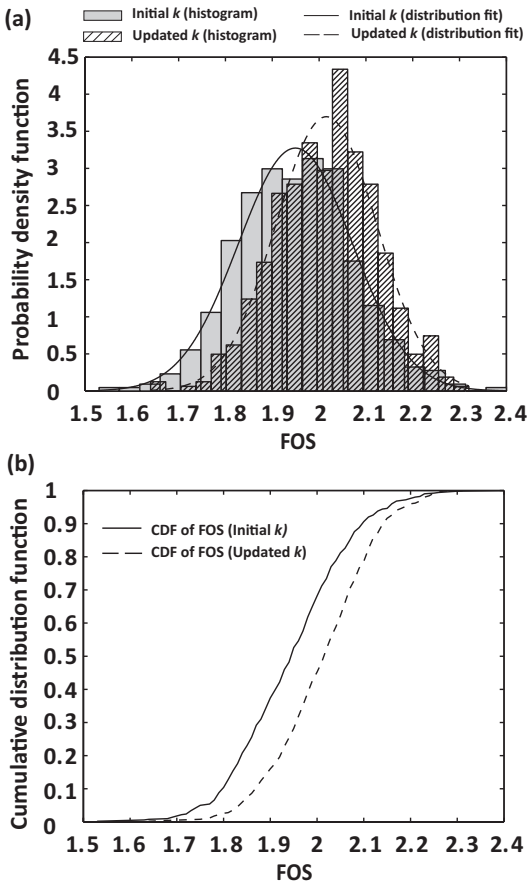

Figure 3.10: Probability distributions of FOS based on the initial and updated pore pressure fields, based on 500 realisations: (a) PDF of FOS and (b) CDF of FOS.

0.12, whereas the mean and standard deviation of the FOS in the updated case are 2.02 and 0.11. Hence there is a modest reduction in the uncertainty and an increase in the computed slope reliability when considering updated pore pressure simulations. Note that the increase in the mean FOS is due to the specific distribution of pore pressures within the foundation layer and the associated changes in shear strength; for another spatial distribution of pore pressure, it could be possible for the mean FOS to decrease when using updated pore pressure simulations. The slight reduction in the standard deviation is explained by a reduction in the possible effective stress variations in the analysis, due to the constrained hydraulic conductivity field.

3.3.4. Slope stability by using improved hydraulic conductivity estimation and strength parameters cross-correlated with hydraulic conductivity

In this section, the previous improved estimations of pore pressure are again imported into the slope stability analysis. However, due to the cross-correlation proposed between hydraulic conductivity and strength parameters, and between the shear strength components themselves, updated strength parameters have also been used in the slope stability analysis.

This section proposes that the hydraulic conductivity can be correlated with the shear strength properties of the soil. While little experimental data have previously been analysed in this manner, both properties have been investigated in terms of porosity and particle size. Relevant literature has been reviewed in Section 2.2.2 of Chapter 2.

The correlation matrix that has been used, for illustrative purposes, is

$$\rho = \begin{bmatrix} 1 & -0.5 & -0.2 \\ \rho_{\ln k,c} & 1 & -0.5 \\ \rho_{\ln k,\phi} & \rho_{c,\phi} & 1 \end{bmatrix} \tag{3.20}$$

As reviewed in the previous literature, it is proposed that, as a soil gets denser, the permeability will decrease and the friction angle and cohesion will increase (e.g. Bartetzko and Kopf, 2007; Carman, 1937; Thevanayagam, 1998). Moreover, a lower permeability may also be apparent if there are more smaller, for example, clay particles, which may then result in a higher cohesion. Therefore, a negative cross-correlation between hydraulic conductivity and both the friction angle and cohesion has been considered. The effect of the cross-correlation has been investigated in detail in Section 3.3.5. As for the cross-correlation between cohesion and friction angle, Arnold and Hicks (2011) indicated that normally there is a negative correlation between these two strength parameters. Rackwitz (2000) suggested that the correlation coefficient between friction angle and cohesion is negative and around -0.5, although El-Ramly et al. (2006) and Suchomel and Mašín (2010) found that the cross-correlation between cohesion and tangent of friction angle is -0.06 and -0.0719, respectively, for the same marine clay. Therefore, in this study, two different cases were analysed; one considered the cross-correlation between cohesion and friction angle, and the other did not.

It can be seen, in Figure 3.11, that there is a further reduction in slope stability uncertainty when the cross-correlations between the hydraulic and strength parameters are accounted for. The mean and standard deviation of FOS, which are based on the updated hydraulic conductivity and cross-correlated strength parameters with hydraulic conductivity, are (a) 1.97 and 0.10 when the cohesion and friction angle are uncorrelated ($\rho_{c,\phi} = 0$); and (b) 2.00 and 0.06 when the cohesion and friction angle are negatively correlated ($\rho_{c,\phi} = -0.5$). Figure 3.11(c) summarises the results in the form of cumulative distribution functions. It can be seen that the reliable FOS, for example, at the 95% confidence level, increases from 1.76 for the initial distribution of hydraulic conductivity, to 1.82 for the updated distribution of hydraulic conductivity, to 1.90 when the shear strength properties are

cross-correlated.

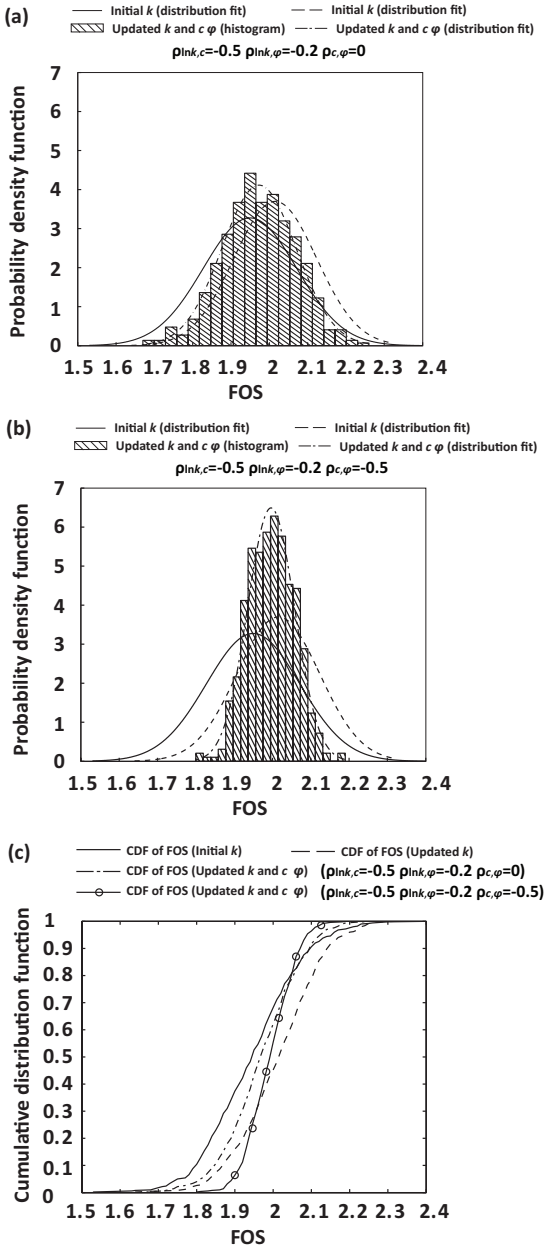

Figure 3.11: Probability distributions of FOS for four different cases: (a) PDF of FOS ($\rho_{\ln k,c} = -0.5$, $\rho_{\ln k,\phi} = -0.2$, $\rho_{c,\phi} = 0$); (b) PDF of FOS ($\rho_{\ln k,c} = -0.5$, $\rho_{\ln k,\phi} = -0.2$, $\rho_{c,\phi} = -0.5$) and (c) CDF of FOS.

3.3.5. Sensitivity of the numerical approach

This section focuses on the sensitivity of the numerical approach with respect to both the number of synthetic measurements and the degree of cross-correlation between the hydraulic conductivity and strength parameters.

Number of measurement points

In the previous illustrative example, the number of measurement points is 88. In order to investigate the influence of the number of measurement points, three further configurations of measurement points have been considered; these are for 12, 24 and 44 points, at the locations shown in Figure 3.5.

It can be seen from Figure 3.12 that, when the number of measurement points is 12, the RMSE of hydraulic head for the measured points is higher than in the other three cases, indicating more error. Figure 3.13 shows the standard deviation of the inflow (the sums of the fluxes flowing into the model domain) against the number of measurement points. As the number of measurement points increases, the standard deviation of the calculated inflow decreases. However, it can be seen that, even when the number of measurement points is small, that is, 12, there is still a significant reduction in the standard deviation, illustrating that the hydraulic conductivity field is better captured.

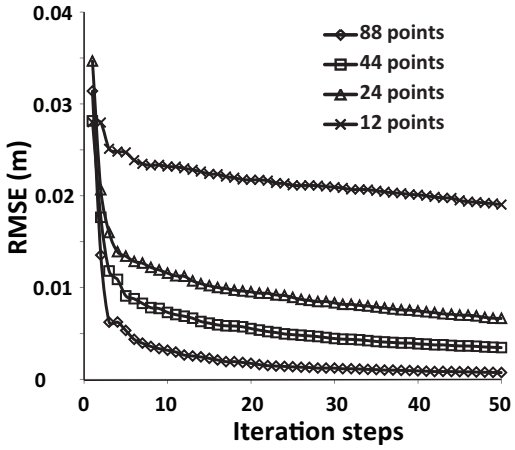

Figure 3.12: RMSE of hydraulic head for different numbers of measurement points.

Influence of cross-correlation between hydraulic conductivity and strength parameters

This section studies the sensitivity of the FOS distribution to different correlation coefficients. Table 3.1 gives the scenarios which have been studied. Scenario 1 is to keep $\rho_{\ln k,c}$ constant and change $\rho_{\ln k,\phi}$. Scenario 2 is the opposite. Scenarios 1 and 2 do not take account of the cross-correlation between cohesion and friction angle. In Scenario 3, the cohesion and friction angle are cross-correlated.

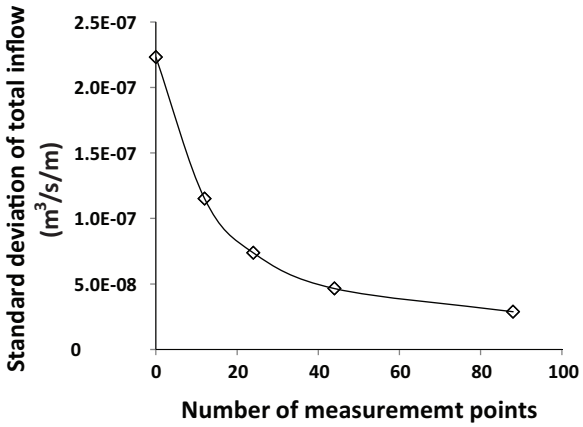

Figure 3.13: Standard deviation of total inflow for different numbers of measurement points.

Table 3.1: Scenarios for the sensitivity analysis of the cross-correlation coefficients.

Scenario	Analysis	$\rho_{\ln k,c}$	$\rho_{\ln k,\phi}$	$\rho_{c,\phi}$	μ_{FOS}	σ_{FOS}
1	1	-0.5	-0.5	0	1.954	0.079
	2	-0.5	-0.2	0	1.973	0.097
	3	-0.5	-0.1	0	1.980	0.101
	4	-0.5	0.2	0	2.002	0.108
	5	-0.5	0.5	0	2.028	0.109
2	6	-0.3	-0.2	0	1.983	0.103
	7	0	-0.2	0	2.000	0.107
	8	0.3	-0.2	0	2.020	0.107
	9	0.5	-0.2	0	2.034	0.106
3	10	-0.5	-0.2	-0.5	1.996	0.062
	11	-0.5	-0.2	-0.2	1.982	0.085

In the case which does not utilise inverse analysis, $\mu_{\mathrm{FOS}} = 1.95$ and the standard deviation of FOS is 0.122. The μ_{FOS} for the case which utilises inverse analysis, but does not take account of cross-correlation between any of the parameters, is 2.02 and the standard deviation of FOS is 0.108. Table 3.1 shows that there can be a further improvement in μ_{FOS} and the standard deviation, irrespective of the cross-correlation.

It can be seen in Figure 3.14(a) that, in Scenario 1, when the cross-correlation $\rho_{\ln k,\phi}$ increases, μ_{FOS} also increases. The increase in μ_{FOS} is related to the hydraulic conductivity in the foundation. In Figure 3.3(a), the "real" values of hydraulic conductivity near the embankment toe, through which the slip surface passes, are relatively large compared to those in other areas of the foundation. After using inverse analysis, the improved estimation of the hydraulic conductivity also gives higher local values in this area. Therefore, when $\rho_{\ln k,c}$ is constant and $\rho_{\ln k,\phi}$ changes

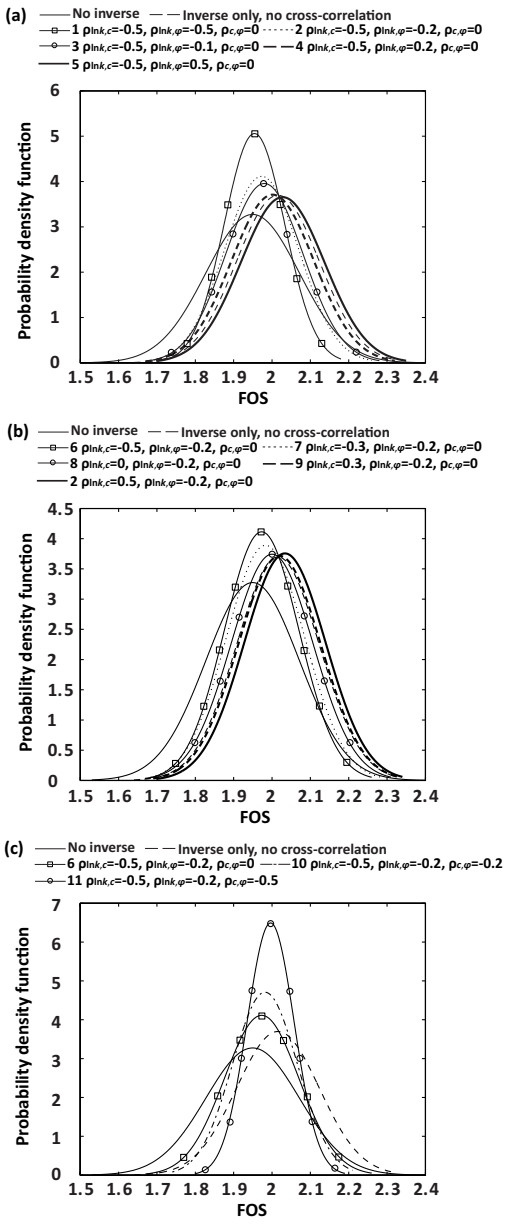

Figure 3.14: Fitted normal distributions of FOS for different coefficients of cross-correlation: (a) influence of $\rho_{\ln k,\phi}$; (b) influence of $\rho_{\ln k,c}$ and (c) influence of $\rho_{c,\phi}$.

from negative to positive values, it means that the friction angle, which is cross-correlated with the improved estimation of k, increases near the embankment toe. The increase of friction angle results in an increase of shear strength which causes

the higher calculated FOS. Meanwhile, Table 3.1 shows that the standard deviation also increases with $\rho_{\ln k,\phi}$. The shear strength is the combined effect of cohesion and friction angle, so when $\rho_{\ln k,\phi}$ increases and $\rho_{\ln k,c}$ is negative and constant, the range of shear strength becomes wider with the increase of the correlation coefficient. The uncertainty in FOS is strongly related to the range of shear strength; hence, the wider the range of shear strength, the larger the standard deviation of FOS. In Figure 3.14(b), the variations of the mean and standard deviation of FOS for Scenario 2 are similar to those for Scenario 1.

In Figure 3.14(c), when the cohesion and friction angle are negatively cross-correlated, the standard deviation of FOS can be further reduced compared to the case in which the cohesion and friction angle are uncorrelated.

In this section, it has been shown that the cross-correlation can play an important role in the final distribution of FOS; in particular, by reducing the uncertainty and thereby generally increasing the FOS corresponding to a confidence level of, for example, 95%. Further research on the values of the cross-correlations, in general, is needed.

3.4. Conclusions

In this chapter, a method to reduce the uncertainty in slope stability analyses via field observations, inverse analysis and the RFEM is presented. It is shown, via the use of a synthetic dataset, that the method can be used to reduce the uncertainty in calculated factors of safety and, in general, reduce the calculated probabilities of failure. It is anticipated that this may contribute significantly to the assessment of existing geotechnical infrastructure.

The main workflow is to first make use of the hydraulic measurements (i.e. pore pressures) to directly improve the estimation of local hydraulic conductivity via inverse analysis. The updated hydraulic conductivity can generate better predictions of the seepage behaviour in the domain. Meanwhile, due to the cross-correlation between hydraulic parameters and strength parameters, the strength parameters (i.e. cohesion and friction angle) can be indirectly updated based on the updated hydraulic conductivity. The updated predictions of both seepage behaviour and strength parameters are simultaneously imported into the slope stability analysis. It is shown that the slope stability computation can not only be improved by the better prediction of the seepage behaviour (i.e. the uncertainty reduced), but also be further improved by cross-correlating the hydraulic and strength parameters. This represents an improvement from previous research in which the hydraulic parameters were updated based on hydraulic measurements and the strength parameters were updated based on displacements.

This method is extended to include time dependency in Chapter 4, as a further step to reduce uncertainty in predictions and reduce the amount of measurement data points required.

4

Sequential Reduction of Slope Stability Uncertainty Based on Temporal Hydraulic Measurements via the Ensemble Kalman Filter

A data assimilation framework, utilising measurements of pore water pressure to sequentially improve the estimation of soil hydraulic parameters and, in turn, the prediction of slope stability, is proposed. Its effectiveness is demonstrated for an idealised numerical example involving the spatial variability of saturated hydraulic conductivity, k_{sat}. It is shown that the estimation of k_{sat} generally improves with more measurement points. The degree of spatial correlation of k_{sat} influences the improvement in predicted performance, as does the selection of initial input statistics into the data assimilation, thereby supporting an initial site investigation as part of the data acquisition process.

This chapter has been submitted to *Computers and Geotechnics*.

4.1. Introduction

The slope stability of an embankment subjected to cyclic water level fluctuation is crucial in geotechnical engineering (Huang et al., 2014; Polemio and Lollino, 2011; Serre et al., 2008), with the distribution of pore water pressure (PWP) under seepage being particularly relevant in any slope stability assessment (Cho, 2012; Zhu et al., 2013). To accurately estimate the PWP, a precise determination of the soil hydraulic parameters is required. However, because it is not realistic to conduct in-situ testing everywhere, some uncertainty remains due to the spatial variability of material properties between measurement locations. This causes difficulty in accurately predicting the seepage behaviour and distribution of pore pressures, and, thereby, the embankment stability.

Data assimilation, which can utilise field measurements, is one method of improving the prediction of slope behaviour, because it can improve the estimation of soil parameters. Most previous studies related to slope back-analysis (or data assimilation) have focused on soil shear strength parameters (Gilbert et al., 1998; Ledesma et al., 1996b; Zhang et al., 2010), in which the utilised measurements were mainly displacement or stress/strain. PWP measurements are seldom used in geotechnical engineering, although, in hydrology, it has already been proven that such measurements improve the estimation of hydraulic parameters (Zhou et al., 2014). In geotechnical engineering, the improved accuracy of hydraulic parameters not only benefits the estimation of PWP but also the prediction of slope stability (Vardon et al., 2016).

A limited number of studies have investigated the influence of improved hydraulic parameters on slope stability, although they have usually ignored the spatial variability of parameter values. For example, Zhang et al. (2016) applied the Bayesian method to back-calculate hydraulic parameters by utilising PWP measurements and investigated the effect of uncertainty in the parameters on the prediction of slope stability, but without incorporating spatial variability. In contrast, Vardon et al. (2016) linked the ensemble Kalman filter (EnKF) (Evensen, 1994, 2003) with the random finite element method (RFEM) (Griffiths and Fenton, 1993) in steady state seepage to back-calculate the hydraulic conductivity based on PWP measurements. They cross-correlated hydraulic conductivity with the strength parameters (cohesion and friction angle) and investigated the influence of the improved hydraulic conductivity on the distribution of the factor of safety (FOS). Meanwhile, Jafarpour and Tarrahi (2011) indicated that an imprecise knowledge of the spatial continuity could induce erroneous estimations of soil property values, whereas Pasetto et al. (2015) investigated the influence of sensor failure on the estimation of k_{sat}, focusing on two cases with two correlation lengths. The results demonstrated that the identification of k_{sat} was more accurate for the larger correlation length. Hommels et al. (2001) compared the EnKF with the Bayesian method, and concluded that the EnKF was easier to implement and could sequentially improve the estimation of parameters once further data became available.

This chapter accounts for the spatial variability of k_{sat}, which plays a dominant role in rainfall infiltration as pointed out by Rahardjo et al. (2007). In addition, the EnKF is applied to improve the estimation of the k_{sat} field by using (in this

instance, numerically generated) 'measurements' of PWP. Due to the existence of spatial variability, the spatial correlation length and arrangement and number of measurement points can have an influence on the data assimilation. Therefore, these aspects are also investigated.

The chapter is organised as follows. Firstly, the formulations of stochastic transient seepage, the EnKF and slope stability are introduced. Then, a synthetic example is analysed, to demonstrate the sequential reduction of the uncertainty in k_{sat} and the influence on the subsequent prediction of slope stability. Finally, an investigation into the influence of the pointwise statistics and spatial continuity of k_{sat} on the data assimilation process via the EnKF, utilising synthetic data, has been undertaken.

4.2. Formulation

4.2.1. Framework of the overall analysis

Chapter 3 utilised hydraulic measurements in steady-state seepage to reduce slope stability uncertainty via the EnKF. The formulation of the numerical approach was also given. This chapter extends the research to transient seepage, as illustrated by the framework shown in Figure 4.1.

With reference to Figure 4.1 (a), the analysis starts by generating an initial ensemble of realisations of the spatial variation of k_{sat}, based on the probability distribution and scales of fluctuation of k_{sat} (i.e. multiple random field realisations of k_{sat} are generated). The initial ensemble of k_{sat} is imported into a stochastic transient seepage process. When the time t reaches t_1, the measurements that have been acquired from the field can be used in the data assimilation process; that is, the EnKF is applied to improve the estimation of k_{sat} for all realisations in the ensemble, based on the measured data. The slope reliability can also be calculated, although, as it is the first time the EnKF is used in the transient seepage process, there is no immediate improvement in the estimated pore pressure. The two options are represented by calculation boxes A and B in Figures 4.1 (b) and 4.1 (c), respectively. The analysis then continues until the time reaches t_2, whereupon the computation of pore water pressure resulting from the improved estimation of k_{sat} (calculated at t_1) can be used to compute the slope reliability. At the same time the EnKF can again be applied to get an updated estimation of k_{sat}, since new PWP measurement data have been acquired. As the analysis proceeds still further, the data assimilation continues to t_3, t_4 and so on, with calculation box A or B being followed at each stage.

4.2.2. Slope stability assessment under transient seepage

The governing equation of 2D transient unsaturated–saturated flow is based on mass conservation, as described in Chapter 5. To solve it, both the soil water retention curve (SWRC), which describes the relationship between the suction head, h_s, and the volumetric water content, θ, and the saturated–unsaturated hydraulic conductivity relationship are necessary. The Van Genuchten–Mualem model (Mualem, 1976; van Genuchten, 1980) has been used to describe the relationship between

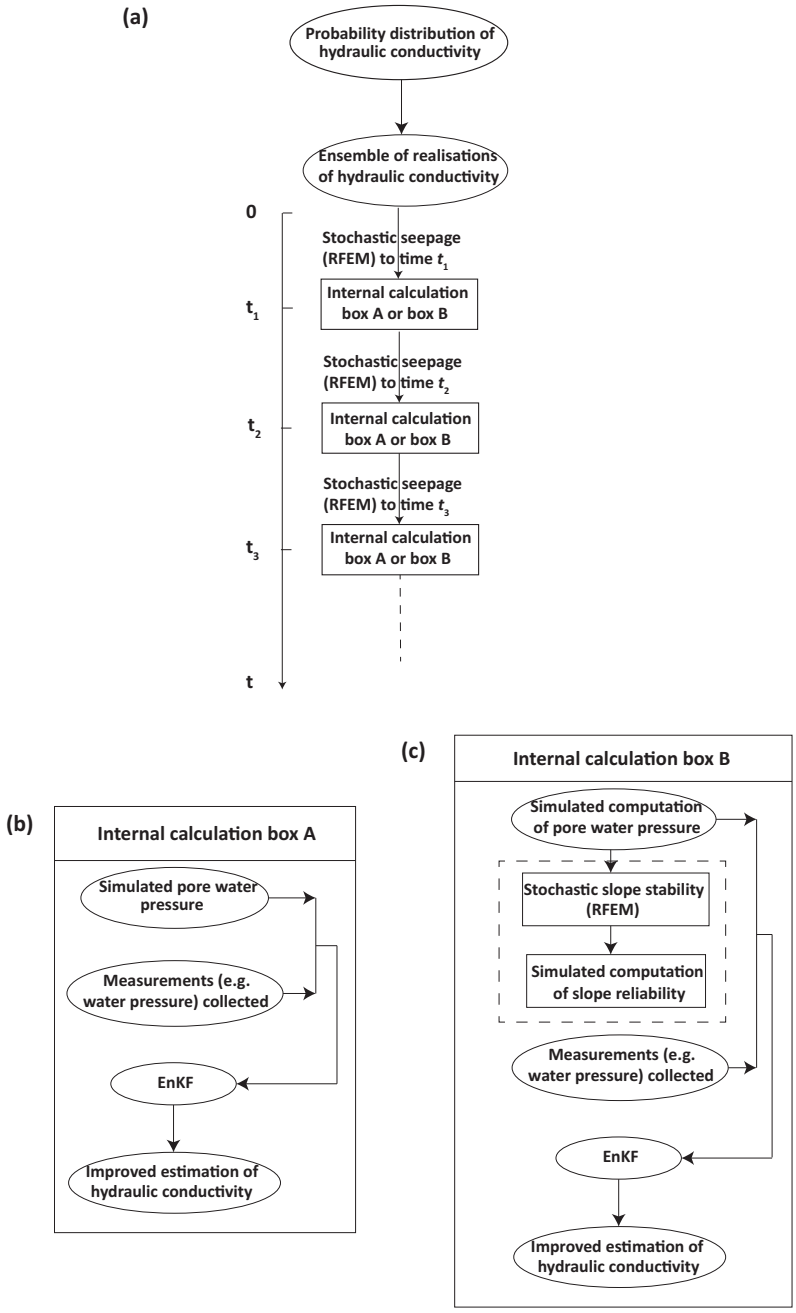

Figure 4.1: Framework of the numerical approach incorporating transient seepage: (a) Overall flow chart; (b) Details of calculation box A; (c) Details of calculation box B.

h_s and θ. In this chapter, the effect of hysteresis is not taken into account, in order to simplify the computation. This behaviour is explored in Chapter 5. The hydraulic conductivity of an unsaturated soil can also be derived using the van Genuchten (1980) model. Figures 4.2 (a) and 4.2 (b) show the volumetric water content and hydraulic conductivity of the unsaturated soil, respectively, as functions of the suction head.

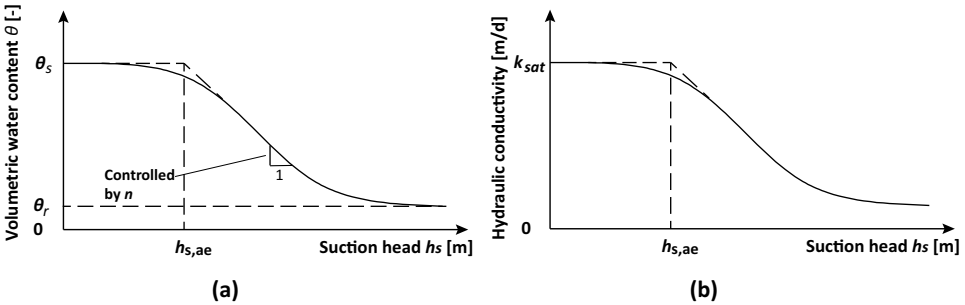

Figure 4.2: The relationships between suction head and (a) volumetric water content and (b) hydraulic conductivity.

As in Chapter 5, Bishop's effective stress, incorporating the influence of both suction and water content, has been combined with the extended Mohr–Coulomb failure criterion to calculate the shear strength.

4.2.3. Soil parameter random fields

The spatial variability of soil parameters is simulated by the generation of random fields, which are based mainly on the statistical distributions and spatial correlations of the parameters. The distribution of a soil parameter is often assumed to be normal or log-normal, and characterised by the mean and standard deviation. In this paper, the distribution of k_{sat} is considered to be log-normal (Griffiths and Fenton, 1993; Zhu et al., 2013), so that the natural log of k_{sat}, $\ln k_{sat}$, follows a normal distribution. The spatial correlation of soil parameters is here characterised by the SOF, l, which is the distance over which parameters are significantly correlated. A more detailed description of the SOF is given in Fenton and Griffiths (2008).

In this chapter, the random fields have been generated using local average subdivision (LAS) (Fenton and Vanmarcke, 1990), using the computer module implemented by Hicks and Samy (2002b, 2004). After the random fields of soil parameters (in this case k_{sat}) have been generated, the values are imported into the finite element program at the Gauss point level and then used in computing the seepage and/or slope stability behaviour. The combined use of random fields and the finite element method (FEM) is often referred to as the random finite element method (RFEM).

4.2.4. Ensemble Kalman filter (EnKF)

The ensemble Kalman filter, developed by Evensen (1994, 2003), has been linked with RFEM using the implementation described in Chapter 3. The difference between this chapter and Chapter 3 is that, here, the measurement of PWP is from a transient seepage process, so that the analysis is able to capture additional information as time progresses. Theoretically, the EnKF can be applied at any time that measurements are acquired. However, because it requires a lot of computational effort, in this chapter, the EnKF has been applied at selected practical time steps during the transient seepage process. During each application of the EnKF, no subsampling methods have been applied; the recorded data at the specific timestep have been selected, i.e. selective data thinning has been used.

4.3. Illustrative analysis

An idealised embankment subjected to cyclic water level fluctuation has been taken as an example to demonstrate the behaviour of the proposed approach; that is, in sequentially improving the estimation of k_{sat} by using PWP measurements and thereby the influence of the updated hydraulic parameters on the prediction of slope stability.

The geometry of the embankment is shown in Figure 4.3. Its height is 12 m, and the width of the crest and base are 4 m and 52 m, respectively. The embankment experiences a water level fluctuation on the upstream side, with WL1 and WL2 being the highest and lowest water levels. The downstream water level remains at foundation level ($z = 0$ m). The bottom boundary is impermeable and fixed.

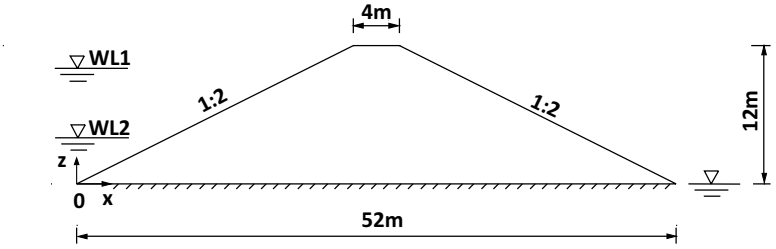

Figure 4.3: Geometry of the embankment.

The water level fluctuation has been simulated by the summation of two sinusoidal curves (Figure 4.4). $T_1 = 1000$ days is the time period of sinusoidal 1 (component 1 in Figure 4.4) and T_2 is the time period of sinusoidal 2 (component 2 in Figure 4.4), in which $T_1 = 3T_2$. The small arrows in the figure indicate the times at which the pore water measurement data were acquired and the EnKF applied, while the numbers along the top of the figure indicate which application of the EnKF the arrows refer to. The slope stability analyses have been done directly before the 2nd, 4th, 6th, 8th, 10th and 12th data assimilations.

In the embankment, the heterogeneity of k_{sat} has been characterised by its probability distribution, i.e. as characterised by the mean, μ, and standard deviation, σ, of k_{sat}, and by the SOF. The mean and coefficient of variation of k_{sat}

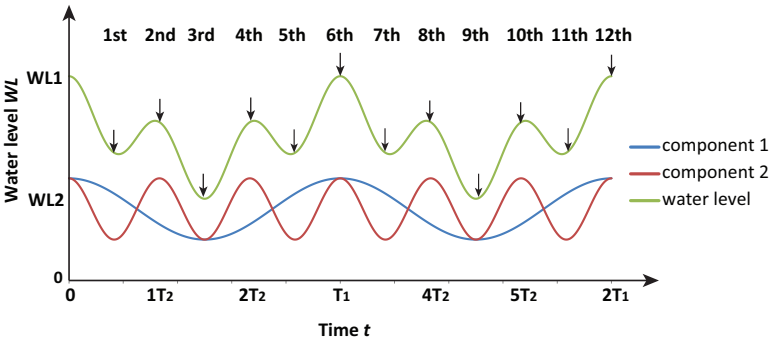

Figure 4.4: Water level fluctuation simulated by two sinusoidal curves.

are assumed to be 1.0×10^{-8} m/s and 1.0, respectively, whereas the vertical and horizontal SOFs of k_{sat} are assumed to be $l_v = 1.0$ m and $l_h = 8.0$ m, respectively. The mechanical parameters and other hydraulic parameters are assumed to be deterministic and are listed in Table 4.1.

Table 4.1: Parameter values for the illustrative example.

Parameter	Symbol	Unit	Value
VGM parameter for the curve	α_d	m^{-1}	0.1
Fitting parameter for VGM model	n	-	1.226
Saturated volumetric water content	θ_s	-	0.38
Residual volumetric water content	θ_r	-	0.0038
Stiffness	E	kPa	1.0×10^5
Poisson's ratio	ν	-	0.3
Effective cohesion	c'	kPa	15
Effective friction angle	ϕ'	^{0}	20
Specific unit weight	G_s	-	2.02

Note: VGM denotes the Van Genuchten–Mualem model, described in Section 4.2.2

LAS has been used to generate 1000 random fields as initial ensemble members. It has also been used to generate a single reference realisation, based on the same statistics as used for the ensemble. This is to represent 'real' values of hydraulic conductivity (as might be obtained from the field) and has been used in the seepage analysis to produce 'real' data of PWP to be assimilated.

Two indicators are used to evaluate the performance of the EnKF:

$$\mathrm{RMSE} = \sqrt{\frac{1}{N_k}\sum_{j=1}^{N_k}\left(\left(\ln k_{sat}^j\right)^r - \left(\ln k_{sat}^j\right)^e\right)^2} \tag{4.1}$$

$$\text{SPREAD} = \sqrt{\frac{1}{N_k}\sum_{j=1}^{N_k} \text{VAR}(j)} \tag{4.2}$$

where RMSE is the root mean square error and SPREAD is a measure of the uncertainty of the ensemble members, and in which j is the Gauss point number, N_k is the number of random field cells in the embankment, superscripts r and e indicate the 'real' and ensemble mean values, respectively, and $\text{VAR}(j)$ is the ensemble variance for each unknown k_{sat}, computed over all the ensemble members.

4.4. Results

4.4.1. Example analysis

This section demonstrates the capability of the EnKF in sequentially improving the estimation of the spatially varying k_{sat}, as well as the subsequent prediction of slope stability.

Estimation of k_{sat} via the EnKF

The number of measurement points used in the EnKF is 63, and the locations are shown in Figure 4.11 and Table 4.2. Figure 4.5 shows the comparison between the reference $\ln k_{sat}$ field, and the initial and improved estimations of the same field. It is seen that, after data assimilation, the estimated local variability of k_{sat} is significantly improved.

Figure 4.6 shows the reduction of the RMSE and ensemble spread of k_{sat}. Whereas the RMSE decreases quickly in the first few assimilation steps and becomes stable thereafter, the SPREAD decreases continuously. Based on Equation 4.1, the decrease in RMSE indicates that the estimation of k_{sat}, i.e. the ensemble mean of k_{sat}, becomes closer to the 'real' value. Based on Equation 4.2, the decrease in SPREAD indicates that the variability of k_{sat} at each Gauss point becomes smaller.

Figure 4.7 compares, for each Gauss point in the finite element mesh, the ensemble mean of $\ln k_{sat}$ with the reference $\ln k_{sat}$. The straight diagonal line in the figure indicates a perfect match between the two quantities. Therefore, the closer to the line a circle (representing a Gauss point value) is, the closer the ensemble mean k_{sat} of this point is to the reference k_{sat}. The colour of the circle represents the numbering of the Gauss points, i.e. from 1 to 2784. In addition, the size of the circle indicates the ratio of the horizontal to vertical coordinates of the points, i.e. x/z. Figure 4.7 shows the ensemble means of $\ln k_{sat}$ getting closer to the reference $\ln k_{sat}$ as the number of assimilation steps increases.

Prediction of the slope stability

The improved estimation of k_{sat} results in an improvement in the estimation of PWP. This influences the effective stress, which, in turn, influences the prediction of slope stability. Figure 4.8 shows the distributions of FOS with and without data assimilation, i.e. the probability density function (PDF) and cumulative distribution

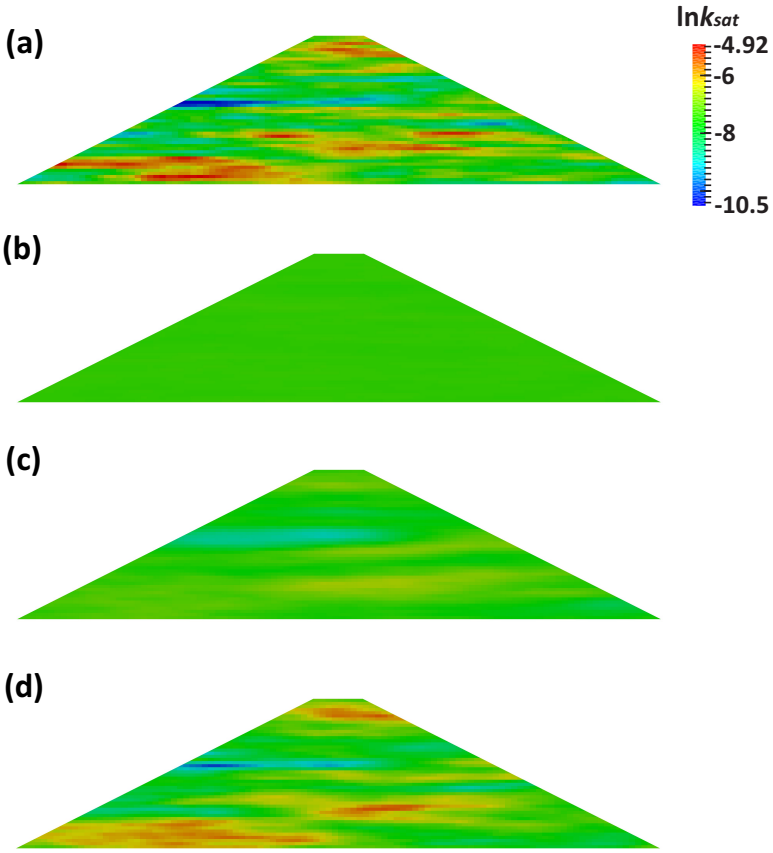

Figure 4.5: Improved estimation of $\ln k_{sat}$ field ($l_v = 1$ m and $l_h = 8$ m): (a) Reference field; (b) Initial estimation before assimilation; (c) Improved estimation after 1st assimilation step; (d) Improved estimation after 11th assimilation step.

function (CDF) at different times, as well as the corresponding improved $\ln k_{sat}$ random fields. The solid vertical line represents the 'real' FOS calculated using the PWP derived from the reference k_{sat} field. It is seen that the prediction of slope stability can be improved via data assimilation using PWP measurements, due to the standard deviation of the FOS decreasing compared to the original distribution. This is mainly due to the decreased ensemble spread of k_{sat} (Figure 4.6), which reduces the uncertainty in the estimation of PWP and, in turn, the uncertainty in the slope stability.

Note that Figure 4.8 (e) shows the mean of the predicted FOS just before the 10th assimilation step to be less accurate than before the 8th assimilation (Figure 4.8 (d)). This is because the error between the 'real' PWP and computed PWP increases. The error is defined as:

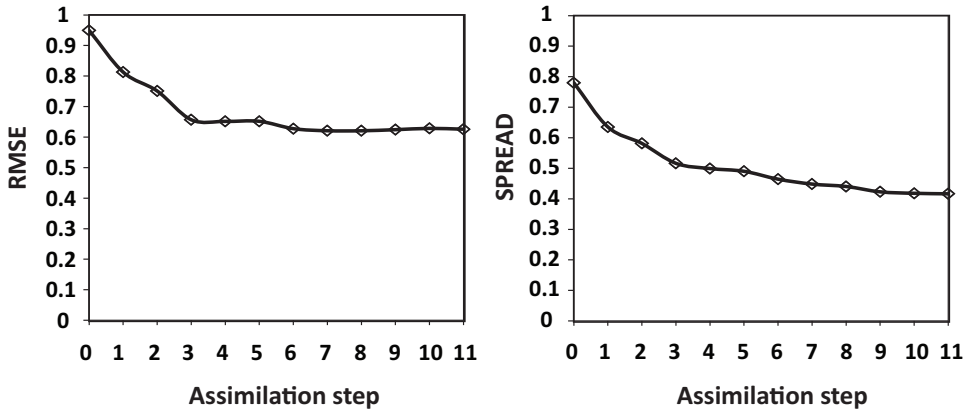

Figure 4.6: RMSE and SPREAD as a function of assimilation step.

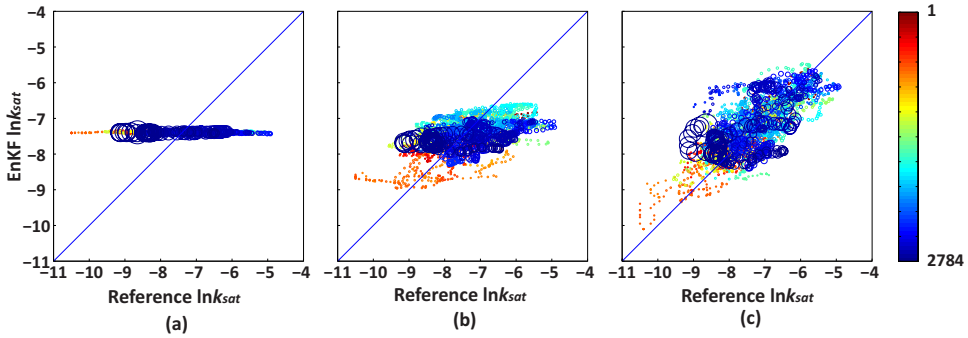

Figure 4.7: Ensemble mean $\ln k_{sat}$ versus reference $\ln k_{sat}$: (a) before data assimilation; (b) after 1st data assimilation step; and (c) after 11th data assimilation step.

$$\text{Error} = \sqrt{\frac{1}{nn}\sum_{j=1}^{nn}\frac{1}{N}\sum_{i=1}^{N}\left(\text{PWP}_{i,j}^{e} - \text{PWP}_{j}^{r}\right)^2} \tag{4.3}$$

where nn is the number of element nodes, N is the number of ensemble members, and PWP^e and PWP^r are the computed PWP and 'real' PWP based on the reference hydraulic conductivity field, respectively. Figure 4.9 shows the variation of Error (in terms of PWP head) with time. It is seen that the Error increases at $t = 5T_2$, causing the mean of the FOS in Figure 4.8 (e) to move to the right relative to the 'real' solution and the standard deviation of the FOS to increase. The Error increase is due to the increased uncertainty in the PWP, which is due to the transient drying–wetting seepage process. The uncertainty in the PWP changes with time, partly due to the non-linearity of the SWRC and partly because some soils are still drying while others could be wetting. Figures 4.8 (f), 4.8 (l) and 4.8 (r) are the

results at $t = 2T_1$, revealing that the mean of the predicted FOS starts getting closer to the reference FOS again.

To further illustrate this, the computation of the seepage process and slope stability have been extended to $8T_2$. Figure 4.10 (a) shows the variation of the computed mean FOS and reference FOS with time, and Figure 4.10 (b) shows the variation of the standard deviation of FOS with time, with and without data assimilation. As expected, the standard deviation is significantly smaller when incorporating data assimilation, although it fluctuates with time as the process continues (due to the fluctuating external loading).

4.4.2. Sensitivity to the number of measurement points

Estimation of k_{sat}

The estimation of the spatial variability of k_{sat} requires PWP sensors to be installed to capture the local variability. In this section, the influence of different numbers of measurement points on the estimation of k_{sat} is investigated. These points are assumed to be located at selected finite element nodes, as shown in Figure 4.11 (b), in which the numbers indicated below the embankment are the allocated serial numbers of the columns of measurement points. In order to investigate the influence of the number of measurement points, different numbers of measurement points were used by selecting different combinations of columns. The details are in given Table 4.2.

Table 4.2: Scenarios of different numbers of measurement points.

Scenario	Columns selected	Number of measurement points
1	$\pm 12, \pm 10, \pm 8, \pm 6, \pm 4, \pm 2, 0$	155
2	$\pm 12, \pm 9, \pm 6, \pm 3, 0$	103
3	$\pm 10, \pm 5, 0$	63
4	$\pm 7, 0$	45
5	$\pm 12, 0$	25
6	Points in $\pm 10, \pm 5, 0$ ("—")	8
7	Points in $\pm 5, 0$ ("/")	3

Note: $\pm$ indicates both positive and negative column numbers, the symbol '—' and '/' indicates the position of the points in scenarios 6 and 7, respectively.

The input mean and standard deviation of k_{sat} are the same as in the previous section, as are l_v and l_h. Figure 4.12 shows the influence of the number of measurement points on the estimation of k_{sat}. It is seen that the RMSE and SPREAD decrease with increasing number of measurement points, albeit with less of an impact on the RMSE above 63 points.

Estimation of slope stability

The influence of the number of measurement points on the prediction of slope stability is shown in Figure 4.13. It can be seen that, counter-intuitively, the uncertainty in the FOS for 63 measurement points is slightly less than that for 103

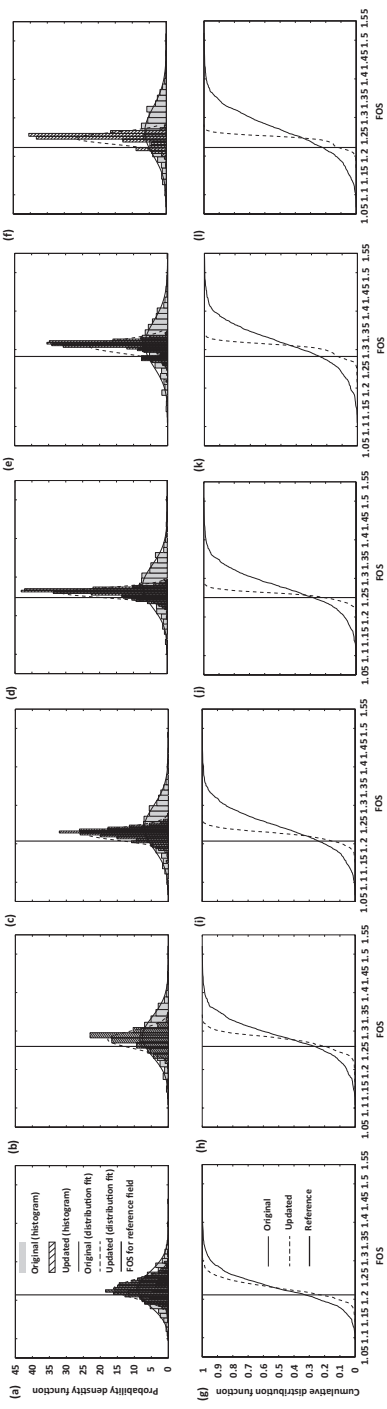

Figure 4.8: Improved prediction of the distribution of FOS: (a) - (f) PDF before 2nd, 4th, 6th, 8th, 10th and 12th assimilations; (g) - (l) CDF before 2nd, 4th, 6th, 8th, 10th and 12th assimilations; (m) - (r) updated $\ln k_{sat}$ field after 1st, 3rd, 5th, 7th, 9th and 11th assimilations.

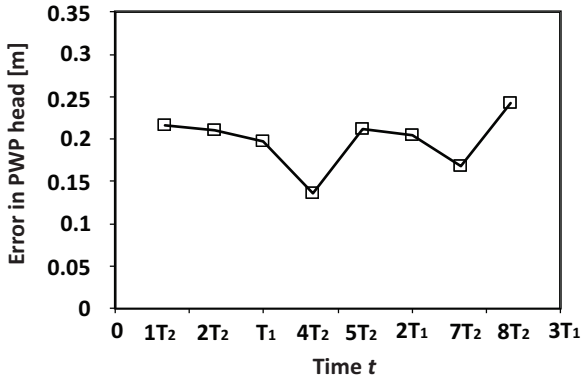

Figure 4.9: Error in PWP versus time.

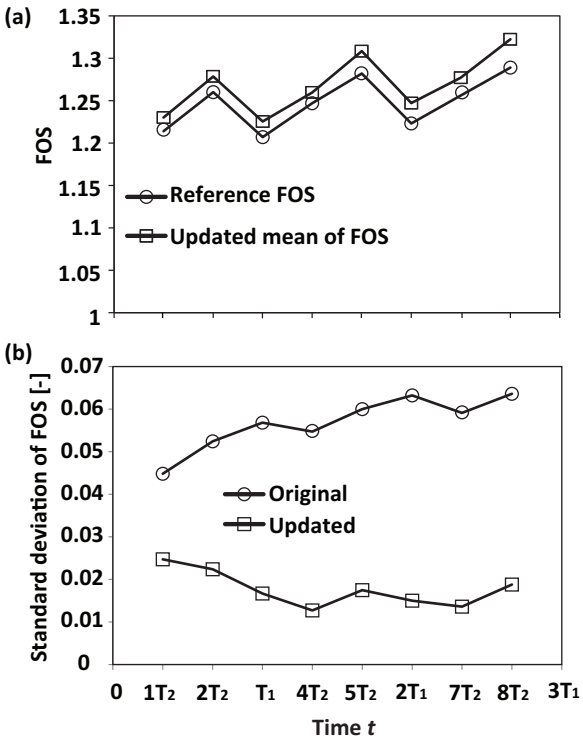

Figure 4.10: FOS and standard deviation of FOS versus time for the original and updated ensembles.

measurement points. This is because the uncertainty in the FOS is also influenced by the measurement locations. To illustrate this, Figure 4.14 shows a comparison between two different configurations of 63 measurement points: the original configuration defined in Table 4.2, and a second in which the 63 points are located in

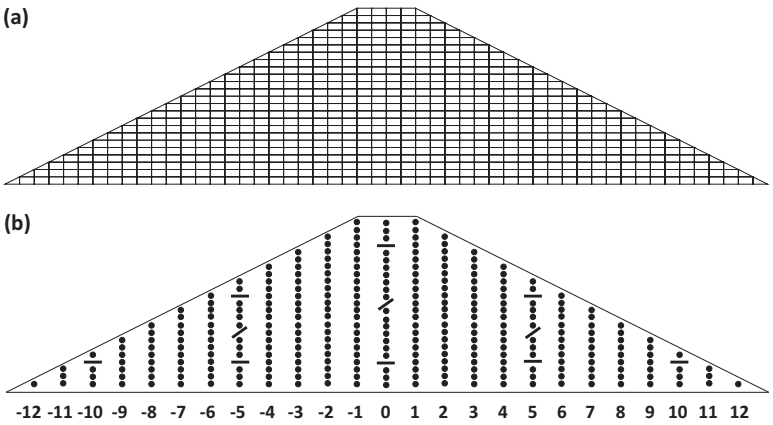

Figure 4.11: FE mesh (a) and location of measurement points (b).

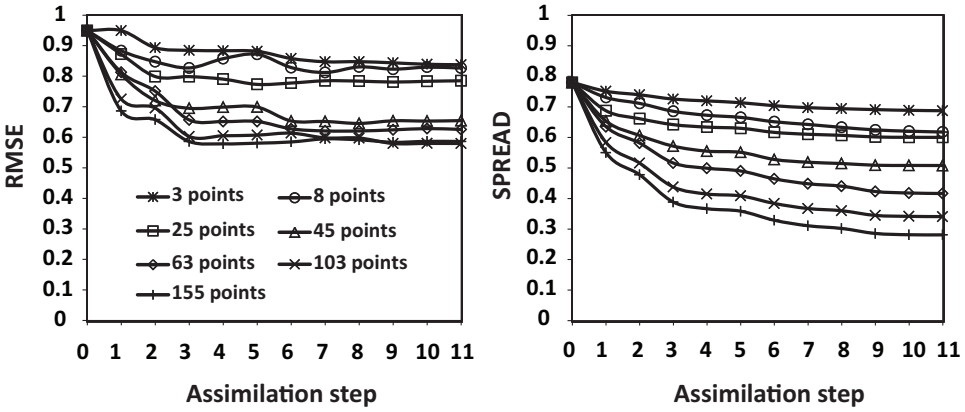

Figure 4.12: Sensitivity of RMSE and SPREAD to the number of measurement points.

Columns 0, $pm3$ and $pm12$. The uncertainty in the FOS for the second configuration is greater due to the different spatial distribution of measurements throughout the embankment as a whole.

4.4.3. Influence of spatial continuity on the data assimilation

The spatial continuity has been proven to be influential in the estimation of k_{sat} when the EnKF is applied in the data assimilation process (Chen and Zhang, 2006; Jafarpour and Tarrahi, 2011; Pasetto et al., 2015). When the SOF is large, the local k_{sat} is more likely to be correlated over a relatively long distance. Therefore, it is hypothesized that, for the same number of measurement points, when the SOF (l) is larger, the assimilated results should give a better estimation of k_{sat}. This has been investigated for both isotropic and anisotropic random fields.

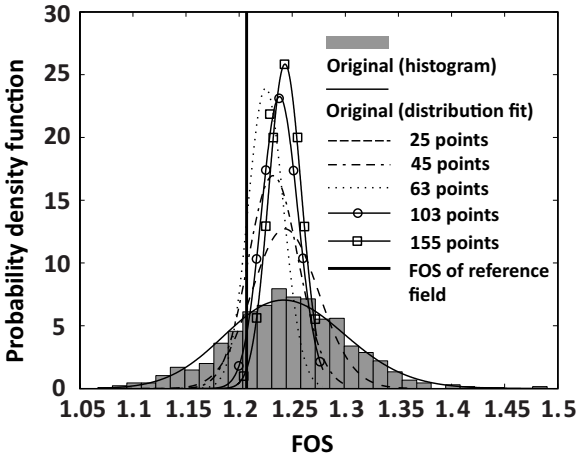

Figure 4.13: Influence of the number of measurement points on the distribution of FOS.

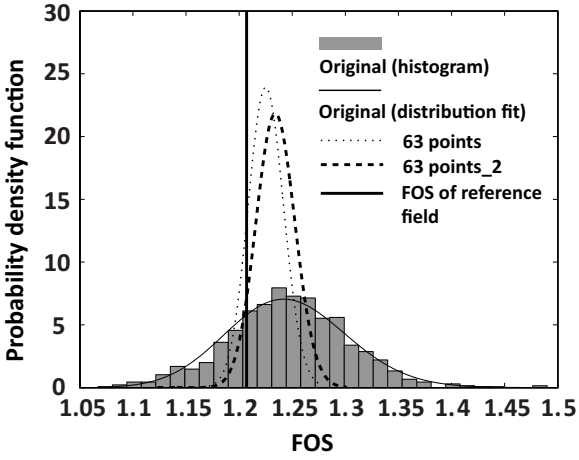

Figure 4.14: Comparison of FOS distributions for two different configurations of 63 measurement points.

Isotropic fields

For isotropic random fields, l_v is equal to l_h. Three different values have been studied here, i.e. $l_v = l_h = 2, 8, 64$ m, as illustrated by typical random fields shown in Figures 4.16 (a), 4.17 (a) and 4.18 (a), respectively. It is seen that, with an increase in the SOF, the domain becomes nearer to a homogeneous field.

Figure 4.15 shows that the RMSE and SPREAD for the three SOFs decrease with an increase in the number of assimilation steps. Moreover, when the SOF is larger, the RMSE is smaller which indicates the updated estimation of k_{sat} is more accurate. The SPREAD is also less for a larger SOF. Figures 4.16–4.18 compare the reference and updated $\ln k_{sat}$ fields for different values of l.

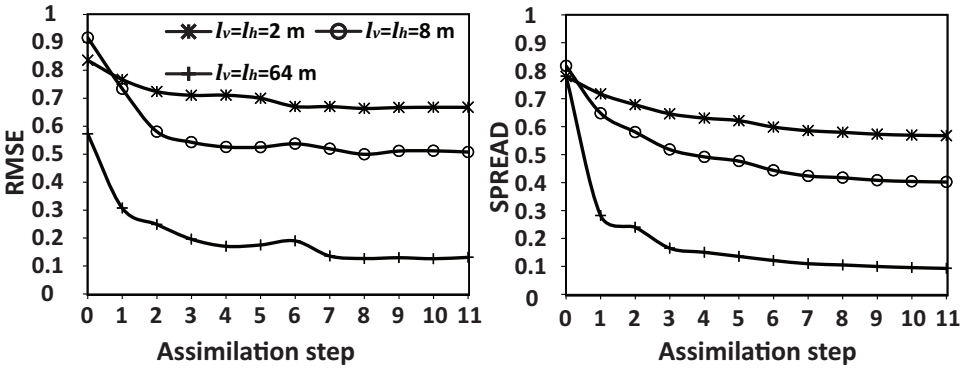

Figure 4.15: Variation of RMSE and SPREAD with SOF for isotropic random fields.

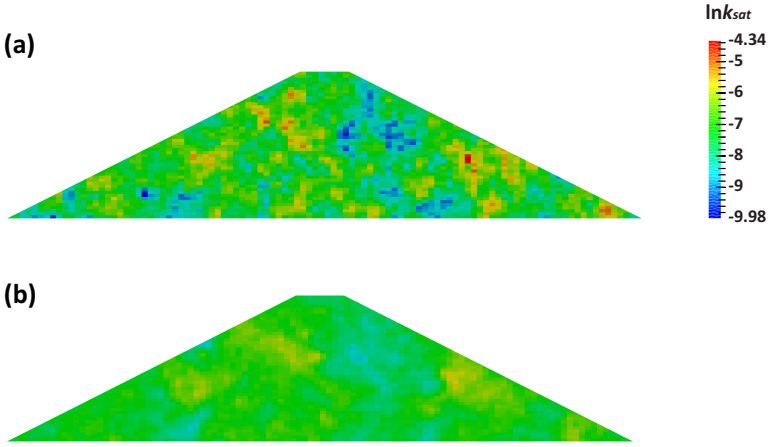

Figure 4.16: Improved estimation of $\ln k_{sat}$ field ($l_v = l_h = 2$ m): (a) Reference field; (b) Improved estimation after 11th assimilation step based on 63 measurement points.

Figure 4.19 shows that the original standard deviation of the FOS increases with an increase in SOF. When the EnKF is applied, by comparing the original and updated standard deviations, it is seen that the reduction of the standard deviation of the FOS is greatest for the largest SOF.

Anisotropic fields

In practice, due to the depositional process of soil, the horizontal SOF tends to be larger than the vertical SOF. In this section, the vertical SOF is assumed to be constant, i.e. $l_v = 1$ m, and the horizontal SOF is $l_h = 2, 8, 64$ m. The larger l_h leads to horizontal passages of lower resistance to water flow. Figures 4.5 (a), 4.21 (a) and 4.22 (a) show typical random fields for the three horizontal SOFs.

In Figure 4.20, the number of measurement points is 63, except for $l_h = 2$ m when two different numbers of measurement points are compared, i.e. 63 and 103.

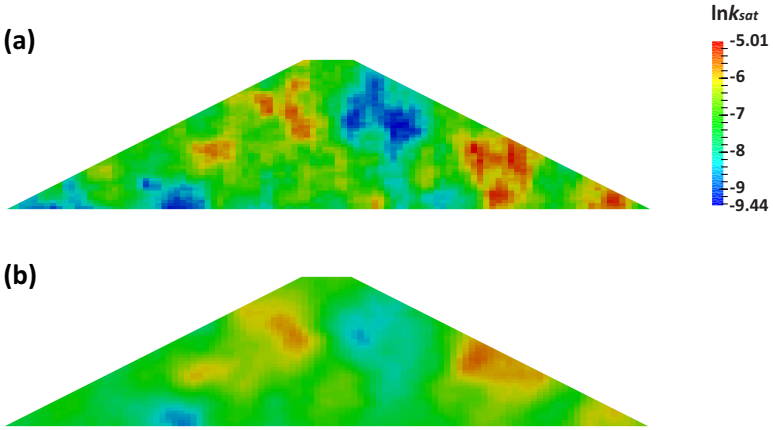

Figure 4.17: Improved estimation of $\ln k_{sat}$ field ($l_v = l_h = 8$ m): (a) Reference field; (b) Improved estimation after 11th assimilation step based on 63 measurement points.

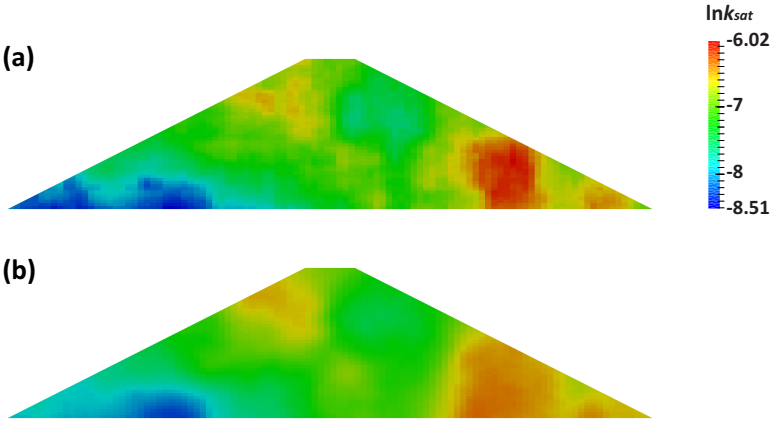

Figure 4.18: Improved estimation of $\ln k_{sat}$ field ($l_v = l_h = 64$ m): (a) Reference field; (b) Improved estimation after 11th assimilation step based on 63 measurement points.

It was found that, when $l_h = 2$ m, the RMSE does not decrease monotonically when 63 measurement points are used. Since the horizontal SOF is small, indicating that the soil property values are correlated over a small distance, more measurement points have also been considered for this case. Figure 4.20 shows that the RMSE decreases when 103 measurement points are used. For $l_h = 8$ and 64 m, the RMSE decreases with increasing number of assimilation steps. The SPREAD decreases with the number of assimilation steps and the extent of the reduction increases with an increase in l_h (and with an increase in the number of measurement points).

Figures 4.21 and 4.22 compare the reference and updated $\ln k_{sat}$ fields for $l_h = 2$ and 64 m, respectively. The case with $l_h = 8$ m is shown in Figure 4.5.

In Figure 4.23, when the EnKF is not applied there is no significant difference in

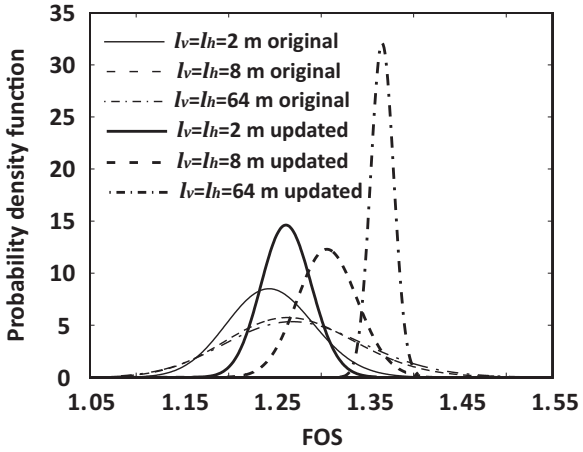

Figure 4.19: Comparison between the original and updated distributions of FOS for different l.

the standard deviations of the FOS. However, when the EnKF is applied, it is seen that the reduction in the standard deviation of the FOS is significant and is highest for $l_h = 8$ m. This indicates that the reduction of the uncertainty does not simply increase with an increase in the horizontal SOF.

4.4.4. Influence of initial ensemble statistics

So far, the generated ensembles have been based on the same spatial statistics as used to generate the 'real' field. This section investigates the impact (on the analysis) of generating ensembles from inaccurate input statistics.

Influence of inaccurate SOF

In the previous analyses, the SOF of k_{sat} was used to generate the initial ensemble members via LAS. Chen and Zhang (2006) briefly analysed the influence of an

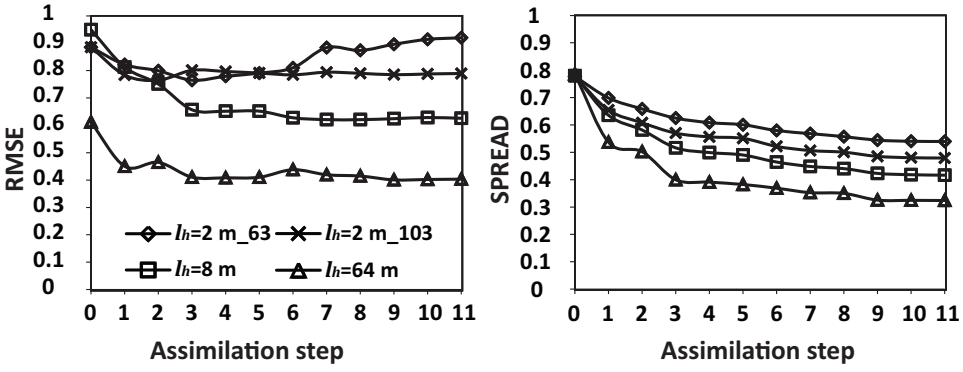

Figure 4.20: Variation of RMSE and SPREAD with SOF for anisotropic random fields.

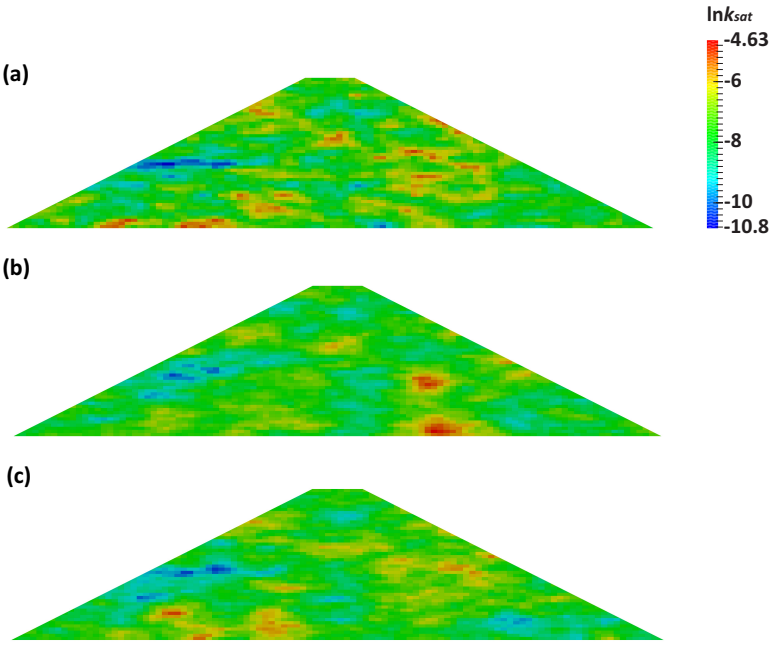

Figure 4.21: Improved estimation of the $\ln k_{sat}$ field ($l_v = 1$ m and $l_h = 2$ m): (a) Reference field; (b) Improved estimation after 11th assimilation step based on 63 measurement points; (c) Improved estimation after 11th assimilation step based on 103 measurement points.

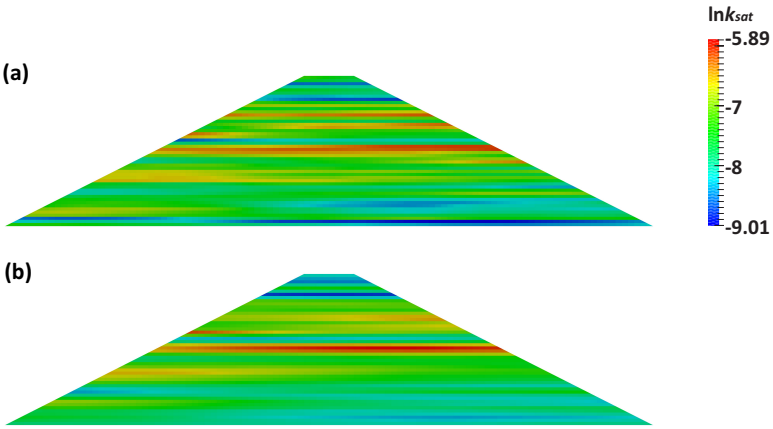

Figure 4.22: Improved estimation of the $\ln k_{sat}$ field ($l_v = 1$m and $l_h = 64$m): (a) Reference field; (b) Improved estimation after 11th assimilation step based on 63 measurement points.

inaccurate integral scale (similar to the SOF) and found that a small deviation (i.e. of 20%) in its value had no significant impact on the assimilation results. However, they also pointed out that wrong information on the statistical anisotropy could

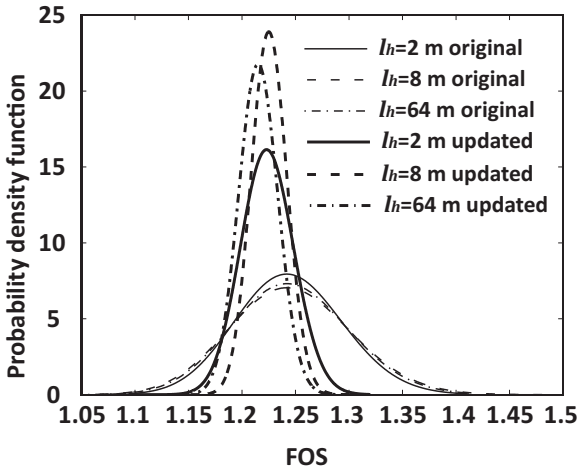

Figure 4.23: Comparison between the original and updated distributions of FOS for different l_h (l_v = 1 m).

have a long-lasting effect on the updated $\ln k_{sat}$ field and that the effect is difficult to eliminate. Therefore, this section analyses a few cases in which l_h is assumed to deviate from the 'real' value, i.e. 50% smaller, 50% larger and 100% larger. In addition, a limiting case where the SOF is assumed to be infinity has been analysed, so that the generated initial ensemble members are based only on the probability distribution of k_{sat}, i.e. on the mean and standard deviation.

Figure 4.24 shows the comparison of the RMSE and SPREAD between the cases, whereas Figure 4.25 shows the reference and updated $\ln k_{sat}$ fields corresponding to the 11th assimilation step, which can be compared with the updated field based on the correct SOF of $l_h = 8$ m in Figure 4.5 (d). Figure 4.25 (b) shows that no spatial variability is modelled in the updated $\ln k_{sat}$ field when the starting SOF is infinity. Moreover, Figure 4.24 (b) shows that the SPREAD with no spatial variability decreases to zero, which implies that the updated estimation of k_{sat} does indeed converge to a single value. Therefore, it can be concluded that the EnKF cannot determine the local variability of k_{sat} without the input of spatial variability in the ensemble members. This can be explained by the calculation of the Kalman gain. If no spatial correlation is initially considered, i.e. the field is homogeneous, in each state vector the corresponding values of hydraulic conductivity will be the same (because k_{sat} is the same throughout the mesh). Then the Kalman gain gives a uniform change in the update of k_{sat}, since there is only a uniform property value in each ensemble. Therefore, the Kalman gain results in the same updates for all local k_{sat} for each ensemble, so that the algorithm is not able to search for local variability of k_{sat} in the reference field.

Influence of inaccurate mean and standard deviation

The influence of the initial mean and standard deviation of k_{sat} has also been investigated, as the initial bias has an influence on the updated estimation of k_{sat}

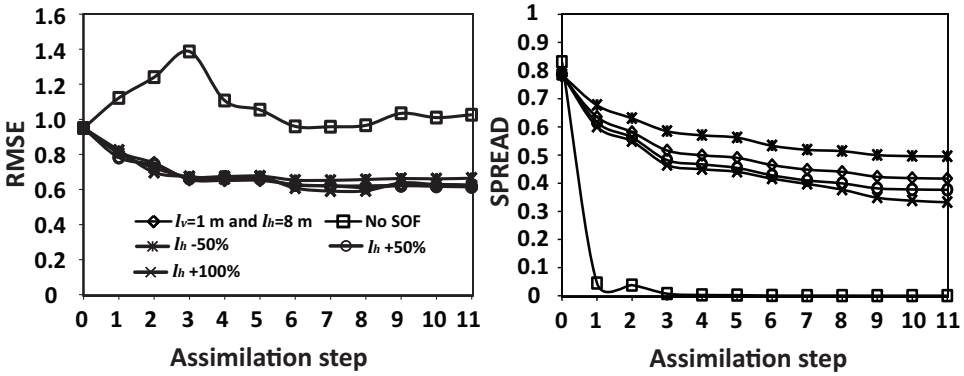

Figure 4.24: Influence of inaccuracy in l_h on variation of RMSE and SPREAD.

(Dee and Da Silva, 1998). First, only the value of the mean was changed. Then, the values of both the mean and standard deviation were changed. Table 4.3 lists the inaccurate values used in the data assimilation process. In both cases, accurate SOFs were used.

Table 4.3: Inaccurate mean and standard deviation of k_{sat} used in the EnKF.

Case		Mean (m/s)	Standard deviation (m/s)	l_v (m)	l_h (m)
Accurate		1.0×10^{-8}	1.0×10^{-8}	1	8
Inaccuarate	1	5.0×10^{-8}	1.0×10^{-8}		
	2	5.0×10^{-8}	5.0×10^{-8}		

Figures 4.26 and 4.27 compare results between using accurate and inaccurate initial conditions. It is seen that, if only the mean value is inaccurate, there is a big error in the updated estimation of k_{sat} (see Figure 4.27 (b)). This may be explained by Figure 4.28, which shows the three input distributions of k_{sat} with different means and standard deviations. It is seen that, when the mean is inaccurate and the standard deviation is relatively small, there is almost no overlap between the area under the solid line (representing the correct distribution) and the dash–dotted line (representing the inaccurate distribution). The results indicate that, when the initial mean is uncertain, it is better to choose a larger standard deviation in order to get acceptable back-calculated results. This is because, if the initial estimation of the mean and standard deviation is inaccurate, choosing a larger standard deviation for generating the initial ensemble enables the realisations to cover a larger range of values, which, in turn, helps in searching out the correct values of k_{sat} during the data assimilation process. Note that, in Figure 4.28, the distribution curve of k_{sat} based on accurate statistics almost overlaps with the distribution curves of k_{sat} taken from the reference field (Figure 4.27 (a)) and the estimated field (Figure 4.27 (c)).

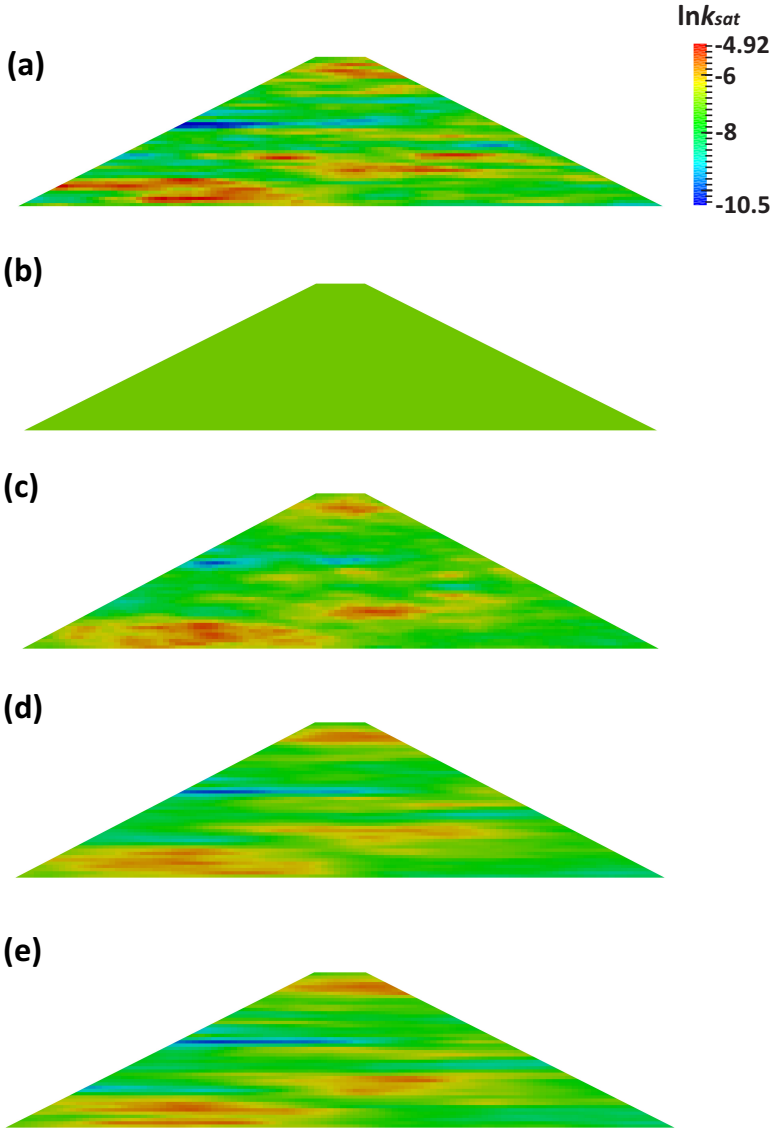

Figure 4.25: Improved estimation of $\ln k_{sat}$ field based on 63 measurement points and various estimates for l_h relative to $l_h = 8$ m: (a) Reference field; (b) Improved estimation (no SOF); (c) Improved estimation (l_h −50%); (d) Improved estimation (l_h +50%); (e) Improved estimation (l_h +100%).

4.5. Comparison between static and temporal measurements

This section compares the difference between using static measurements from steady-state seepage and temporal measurements from a transient seepage pro-

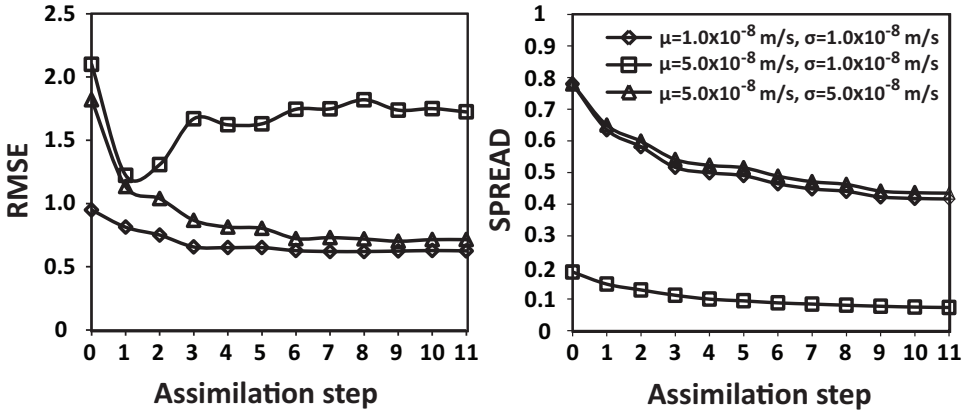

Figure 4.26: Variation of RMSE and SPREAD for cases with accurate and inaccurate initial conditions.

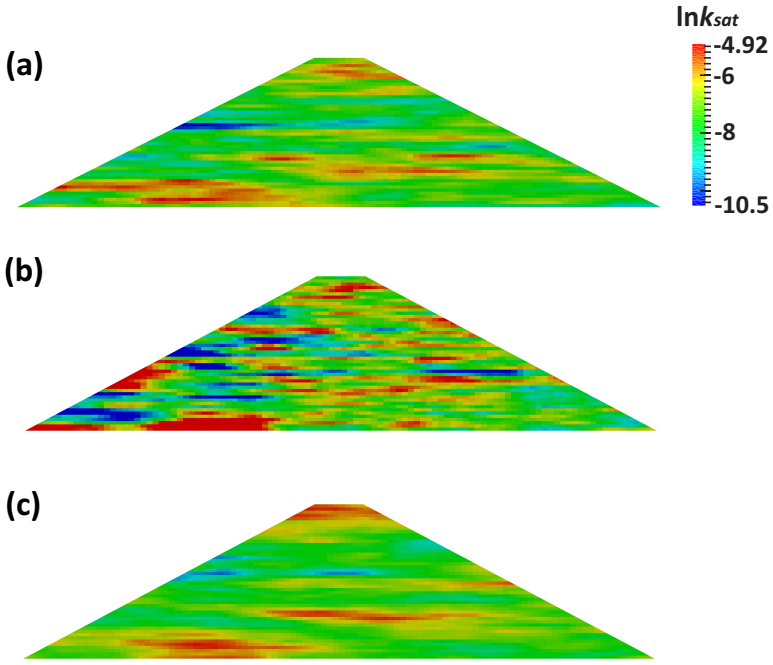

Figure 4.27: Improved estimation of $\ln k_{sat}$ field with inaccurate initial conditions: (a) Reference field; (b) Improved estimation after 11th assimilation step with inaccurate mean only; (c) Improved estimation after 11th assimilation step with both inaccurate mean and standard deviation.

cess. For the static measurements, the water level is assumed to be constant at WL1 and the PWP measurements are used to iteratively update the estimation of k_{sat}.

Figure 4.29 shows the variation of RMSE and SPREAD for the cases using tempo-

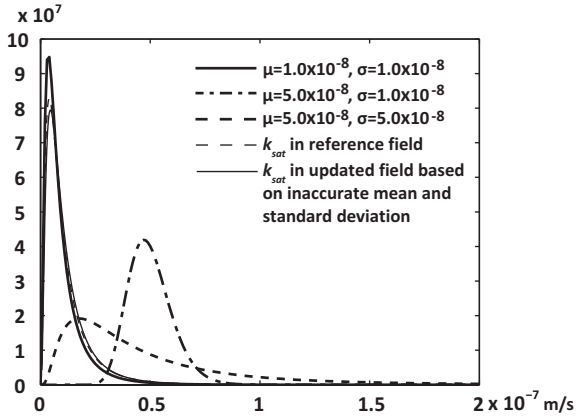

Figure 4.28: Distributions of k_{sat} for different means and standard deviations.

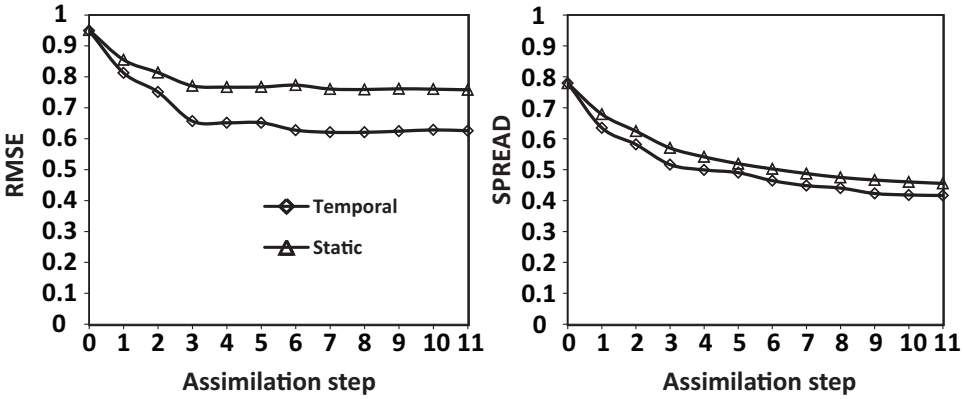

Figure 4.29: RMSE and SPREAD for static and temporal measurements.

ral and static PWP measurements, while Figure 4.30 shows the updated estimation of the $\ln k_{sat}$ field for the two cases. The two figures demonstrate the improvement is better when using temporal measurements, due to more information being available for tuning the results.

4.6. Conclusions

It has been shown that the measurement of PWP can contribute to an improved estimation of k_{sat}. In the transient seepage process, once the measurement of PWP is acquired, the EnKF can be used to improve the estimation of k_{sat} and, thereby, the estimation of seepage behaviour and slope stability. Significantly, the temporal analysis gives more information for tuning results than a steady-state analysis as implemented in Chapter 3. It has been found that the accuracy of the estimation of k_{sat} increases with an increasing number of measurement points, although the

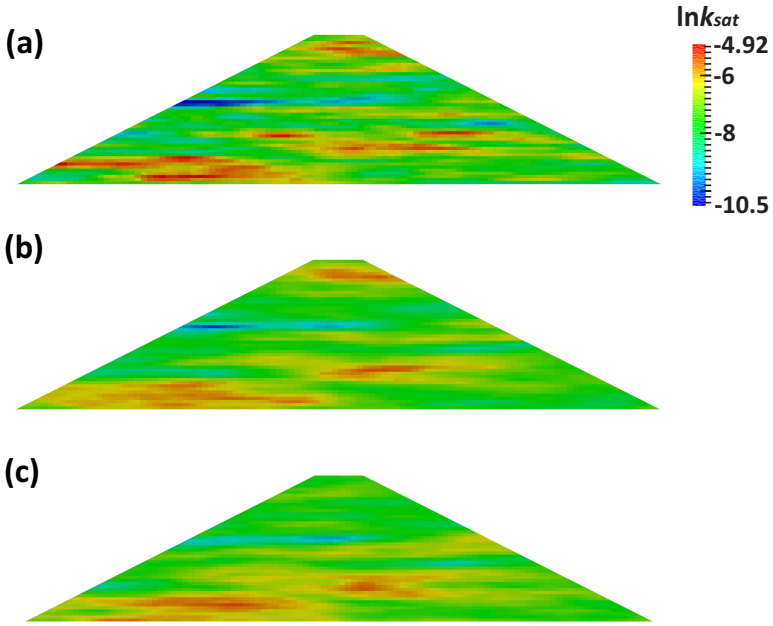

Figure 4.30: Improved estimation of $\ln k_{sat}$ field: (a) Reference field; (b) Improved estimation after 11th assimilation step using temporal measurements; (c) Improved estimation after 11th assimilation step using static measurements.

uncertainty reduction in the FOS does not monotonically increase with the increasing number. However, it should be noted that, whatever the number of measurement points, the uncertainty in the slope stability can be reduced to a certain extent.

It has also been found that the spatial continuity of k_{sat}, as reflected by the magnitude of the SOF used in random field simulations, has an influence on the estimation of k_{sat} and thereby on the estimation of slope stability. The RMSE of k_{sat} is smaller for a larger l for the same number of measurement points. In addition, the SPREAD of k_{sat} reduces as l gets larger. These results indicate that, when the soil parameters are correlated over a longer distance, the improvement in the estimation of k_{sat}, when using the EnKF based on the same number of measurement points, is greater. For slope stability and isotropic spatial variability, the reduction of the uncertainty in the FOS increases with an increasing l. However, for anisotropic spatial variability (for l_v constant and relatively small compared to the height of the embankment), the reduction of the uncertainty in the FOS does not simply increase with an increasing degree of anisotropy, i.e. l_h / l_v , for the analyses presented in this chapter. In addition, although the original standard deviation of the FOS is almost the same for the three values of l_h considered, the updated standard deviation of the FOS shows significant differences for the different l_h.

Last but not least, the initial ensemble statistics of k_{sat} have been investigated. It was found that the EnKF cannot work out the local variability of k_{sat} based only

on the measurement data; that is, without considering the spatial variability in the input ensemble. However, even a relatively inaccurate estimation of the SOF, as input for the initial ensemble, can give an updated estimation of k_{sat} that is almost identical to that obtained using the correct SOF. In addition, when the variation of k_{sat} is not captured well, it is better to assume a larger standard deviation for k_{sat}. This is so that the initial ensemble covers a greater range of values, which helps when searching the parameter space during the assimilation process.

The chapter has only utilised synthetic data to validate the proposed framework, so further work is needed to apply this method to a real project with real measurements.

5

Combined Effect of Hysteresis and Heterogeneity on the Stability of an Embankment under Transient Seepage

The stability of most earth embankments is strongly influenced by the water content of the soil. The water content directly influences the suction or pore pressure in the soil, as well as the mass of material, thereby affecting the stress state and strength, and leading to changes in the stability. These aspects are coupled by the so-called soil water retention behaviour, which is observed to be a hysteretic phenomenon. Moreover, soils are known to be spatially variable or heterogeneous in nature, which can lead to preferential flow paths and stronger or weaker zones. In this chapter the behaviour of a heterogeneous earth embankment subjected to cyclic water level fluctuation, including the impact of hysteresis, is investigated. The soil property values governing the unsaturated hydraulic response of the embankment are considered as spatially random variables, with the mechanical property values considered deterministic in order to isolate the impact of the hydraulic behaviour. The Monte Carlo Method (MCM) is used to conduct probabilistic analyses and an assessment of the relative influence of material properties illustrates that the saturated hydraulic conductivity, k_{sat}, plays a dominant role in the slope stability. Moreover, in the initially drying condition, the average FOS and the 95th percentile FOS of the slope considering hysteresis are smaller than those without considering hysteresis, at all times, while the

This chapter has been published in *Engineering Geology*, 219: 140-150 (2017) (Liu et al., 2017) and initial results in *IOP Conference Series: Earth and Environmental Science*, 26(1): 012013 (2015) (Liu et al., 2015b).

variability of the FOS considering hysteresis is larger than that when not considering hysteresis. In practice, this means that slopes under seepage conditions, which are assessed to have a low FOS, should be assessed including the hysteretic behaviour to ensure stability.

5.1. Introduction

Slopes under seepage conditions, with both saturated and unsaturated zones, are common and of great concern in geotechnical engineering (Chen and Zhang, 2006; Rahardjo et al., 2010). The saturated–unsaturated seepage in the slope has a significant impact on the slope stability, via changes in shear strength and volumetric weights, and is strongly related to the water retention behaviour of the unsaturated soil (Gui et al., 2000; Le et al., 2012; Zhu et al., 2013; Zhang et al., 2015, 2016).

The soil water retention curve (SWRC) describes the relationship between the suction head, h_s, and a measure of the water content, in this chapter the volumetric water content (VWC), θ, and in addition impacts the hydraulic conductivity, k, which further affects the distribution of pore water pressure (PWP) in the soil (Lam et al., 1987; Yang et al., 2012a). Hysteresis in the water retention behaviour of unsaturated soils describes a non-unique relationship between h_s and θ, and thus also between h_s and k (Jaynes, 1984; Pham et al., 2005; Wu et al., 2012). Moreover, due to the existence of hysteresis, the VWC in the soil under cyclic drying and wetting processes may exhibit a significantly different response as compared to the non-hysteretic case (Ma et al., 2011). Indeed, the differences in the PWP and VWC induced by the hysteresis in the SWRC contribute to a hysteretic shear strength response which affects the stability and reliability of the slope (Bishop, 1960).

However, to simplify seepage analyses the effect of hysteresis is commonly ignored (e.g. Tsaparas et al., 2002; Le et al., 2012), even though it may generate inaccurate predictions of the distributions of PWP and VWC. Tami et al. (2004) investigated the variation in the suction profile in a soil column with a hysteretic SWRC. It was found that, due to the hysteresis, the suction at the newly reached steady state after a certain period of infiltration was significantly affected by the initial water content prior to the infiltration process. Yang et al. (2012a) studied the variation of matric suction and VWC in a soil column under cyclic precipitation and evaporation. It was found that the computed results were closer to the experimental results when considering hysteresis.

Recently, several researchers have investigated the effect of hysteresis on the stability of soil slopes. Ebel et al. (2010) pointed out that simulations ignoring hysteresis could underestimate the potential for landslides. Ma et al. (2011) conducted an experimental and numerical study of a soil slope to assess the effect of hysteresis, both on the hydraulic response and the slope stability. It was found that the distribution of water content was influenced by hysteresis and that the calculated FOS of the slope considering hysteresis recovered quickly after rainfall and was larger than that without considering hysteresis for any given time.

Most research that includes the effect of hysteresis focuses on homogeneous soils. Conversely, if the heterogeneity of soil property values is taken into account, the impact of hysteresis is typically not accounted for (Arnold and Hicks, 2010, 2011; Zhu et al., 2013). However, Nakagawa et al. (2012) highlighted the importance of considering both hysteresis and heterogeneity in the simulation of unsaturated flow by comparing numerical results with experimental data. Very few studies have incorporated hysteresis and heterogeneity in the assessment of slope stability. Yang et al. (2012b) accounted for the effect of hysteresis and spatial variability of soil

property values, i.e. of the saturated hydraulic conductivity and some SWRC fitting parameters, in a one-dimensional infiltration problem. It was shown that the combined effect of hysteresis and heterogeneity of soil property values increased the uncertainty in the estimation of the ability to prevent penetration in soil covers, compared to the non-hysteretic but heterogeneous case. Zhang (2007) incorporated both hysteresis and heterogeneity into the stability analysis of a 2D slope under cyclic precipitation and evaporation, with the analysis starting on the wetting SWRC. The results suggested that simulations without considering the effect of hysteresis may underestimate the slope reliability.

This chapter investigates the slope stability of an embankment under transient seepage, i.e. due to a cyclic external water level. However, it extends the research of Chapter 4 in that the effects of both hysteresis and heterogeneity of the soil property values on the seepage response are considered. First, the mechanical and stochastic model framework for slope stability under saturated–unsaturated seepage is briefly introduced. Next, the numerical implementation of the framework is explained, and a specific example then utilised to investigate the impact of considering hysteresis for a homogeneous embankment. Finally, the effect of spatial variability of the soil property values is considered, by conducting a probabilistic analysis of the slope stability and comparing the results of the hysteretic and non-hysteretic cases.

5.2. Formulation

5.2.1. Governing flow equation

The governing equation of 2D transient unsaturated–saturated flow is based on mass conservation. In the flow analysis, the soil skeleton is considered to be rigid, which means that any volume change during the seepage process is not accounted for. Therefore, the governing flow equation, in incremental form, is (e.g. Celia et al., 1990)

$$\frac{\partial}{\partial x}\left(k_x \frac{\partial h_{PWP}}{\partial x}\right) + \frac{\partial}{\partial z}\left(k_z \frac{\partial h_{PWP}}{\partial z} + k_z\right) = C(h_{PWP}) \frac{\partial h_{PWP}}{\partial t} \tag{5.1}$$

where k_x and k_z are the hydraulic conductivities in the x and z directions, respectively, h_{PWP} is the PWP head, t is time and $C(h_{PWP}) = \partial\theta/\partial h_{PWP}$ is the specific moisture capacity function with θ being the VWC. The same description of mass conservation can be used for heterogeneous porous media (e.g. Gui et al., 2000) with an appropriate selection of hydraulic conductivities at each location.

5.2.2. Water retention behaviour

The SWRC is a function relating the suction head, h_s, with θ. The suction head is defined as the negative component of h and is represented by

$$h_s = -h_{PWP} = s/\gamma_w = (u_a - u_w)/\gamma_w \tag{5.2}$$

where s is the matric suction, u_a is the pore air pressure, which is assumed to be atmospheric in this paper, u_w is the PWP and γ_w is the unit weight of water.

The van Genuchten (1980) model is frequently used to describe the SWRC (e.g. Gui et al., 2000; Sivakumar Babu and Murthy, 2005; Phoon et al., 2010) as it can give a good approximation of the experimental results of many soil types (e.g. Han et al., 2010). It is given by

$$\begin{aligned} S &= \frac{\theta-\theta_r}{\theta_s-\theta_r} = \frac{1}{[1+(\alpha|h_{PWP}|^n)]^m} \quad h < 0 \\ S &= 1 \qquad\qquad\qquad\qquad\qquad\qquad\quad h \geq 0 \end{aligned} \tag{5.3}$$

where S is effective degree of saturation, α is a parameter which is approximately the inverse of the air-entry suction head, $h_{s,ae}$, and θ_s and θ_r are the saturated and residual VWC, respectively (see Figure 5.1 (a)). Due to the hysteretic behaviour described by the water retention curve, the main wetting and drying curves have different values of α, i.e. $\alpha_w \approx 1/h_{s,ae,w} > \alpha_d \approx 1/h_{s,ae,d}$. The model parameter n defines the slope of the water retention curve, which is here assumed to be identical for the main wetting and drying responses, and m is a curve fitting parameter which is here approximated (Mualem, 1976) by

$$m = 1 - 1/n \tag{5.4}$$

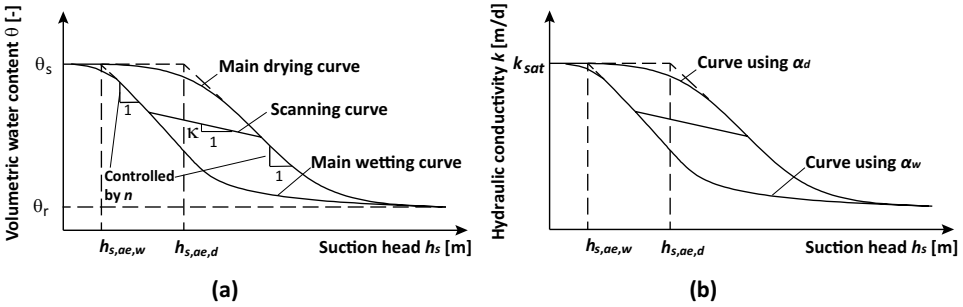

Figure 5.1: The relationships between suction head and; (a) VWC, and (b) hydraulic conductivity.

The hydraulic conductivity of the unsaturated soil is typically a function of the effective degree of saturation (Figure 5.1 (b)). It can be derived from the SWRC by using the van Genuchten (1980) model, for which one common expression is

$$k = k_{sat}\sqrt{S}\left[1-\left(1-S^{n/(n-1)}\right)^m\right]^2 \tag{5.5}$$

where k_{sat} is the saturated hydraulic conductivity of the soil. It can be seen from Figure 5.1 that, due to the hysteresis in the SWRC, there will be also hysteresis in the hydraulic conductivity function with respect to the suction head.

Jaynes (1984) compared four methods of modelling hysteresis in the water retention behaviour, i.e. in approximating the curves between the main wetting and drying curves, referred to as scanning curves, (see Figure 5.1 (a)), and found that the performance of the four methods were equally good in the numerical simulation of hysteretic flow. Furthermore, the author pointed out that, due to simplicity,

linear scanning curves were often used in numerical analyses. Therefore, as this paper is not considering a specific soil, this approach has been adopted here to describe the transition from wetting to drying and vice versa (Figure 5.1 (a)), utilising parameter κ to define the gradient of the curves.

5.2.3. Slope stability assessment

Slope stability equilibrium is solved using a linear elastic, perfectly plastic material model. Bishop's effective stress combined with the extended Mohr–Coulomb failure criterion has been used to model the shear strength (Bishop, 1960):

$$\tau_{ss} = c' + \sigma_t \tan\phi' + \chi s \tan\phi' \tag{5.6}$$

where τ_{ss} is the shear strength, c' and ϕ' are the effective cohesion and friction angle, χ is a scalar parameter defining the suction-induced effective stress, s is the matric suction and α_t is the total stress normal to the sliding plane (Cai and Ugai, 2004). In this chapter, the suction stress, χs, is defined as

$$\begin{aligned} \chi s = Ss = \tfrac{\theta-\theta_r}{\theta_s-\theta_r} s \quad & s > 0 \\ \chi s = Ss = s \quad & s \leq 0 \end{aligned} \tag{5.7}$$

where the suction stress is assumed to equal the effective degree of saturation (Vanapalli et al., 1996). When the suction is negative, i.e. there is a positive PWP, the conventional effective stress is used.

The unit weight, γ, of the unsaturated soil is a function of θ (Tsai and Chen, 2010) and can be expressed as

$$\gamma = [(1-\theta_s)\,\rho_w G_s + \rho_w \theta]\, g \tag{5.8}$$

where ρ_w is the density of water, G_s is the specific gravity of the soil particles and g is the gravitational acceleration.

5.2.4. Spatial variability of soil properties

The heterogeneity of the soil is considered by some soil property values being spatially random variables following normal or lognormal distributions. The point statistics of the variables are described by the distribution type, mean, variance and cross-correlation between different variables. The COV is a normalised measure of the variability, defined as Equation 2.1.

The soil property values are also spatially correlated due to the deposition process. The scale of fluctuation, l, is the distance over which parameter values are significantly correlated (Fenton and Vanmarcke, 1990). In addition, the deposition process causes different scales of fluctuation in the horizontal and vertical directions. Hence, the ratio of the horizontal scale of fluctuation to the vertical scale of fluctuation is referred to as the degree of anisotropy of the heterogeneity, ξ (Hicks and Samy, 2002b, 2004), i.e.

$$\xi = \frac{l_h}{l_v} \tag{5.9}$$

where l_h and l_v are the horizontal and vertical scales of fluctuation, respectively.

For more information about the statistics of soil property values, the reader may refer to Phoon and Kulhawy (1999).

5.3. Numerical implementation

5.3.1. Slope stability under transient seepage

The flow and slope stability analyses both use finite element (FE) programs that have been developed based on Smith et al. (2013); that is, using 4-node quadrilateral elements for the flow analysis and 8-node quadrilateral elements for the slope stability analysis. First, a flow analysis is performed and the variation of suction stress and VWC with time, i.e. $\chi s(t)$ and $\theta(t)$, are computed. Next, the suction stress and VWC from the flow analysis are imported into the slope stability FE programand mapped onto the Gauss points for computing the effective stresses due to gravitational (self-weight) loading.

The governing flow equation has been solved by using the modified Picard iteration method (Celia et al., 1990; Lehmann and Ackerer, 1998). In the flow analysis program, the VWC for the main drying and wetting curves is computed via Equation 5.3. The water retention behaviour along the linear scanning curve is computed via an algorithm proposed by Yang et al. (2011a), in which the VWC at the current time, $t+1$, is determined as a function of the current change in suction head and the previous VWC, i.e. $\theta^{t+1} = f(\Delta h_s^{t+1}, \theta^t)$.

If the PWP at the Gauss point is negative, the soil unit weight is updated by Equation 5.8 in the FE slope stability analysis; otherwisethe unit weight is equal to the saturated unit weight. The strength reduction method (Griffiths and Lane, 1999) has then been applied to compute the FOS of the slope. In this method, the FOS is defined as the factor by which the original shear strength is reduced in order to cause the slope to fail (see Equations 3.3 and 3.4).

5.3.2. Probabilistic simulation

For modelling soil heterogeneity, the Local Average Subdivision (LAS) method (Fenton and Vanmarcke, 1990) has been used to generate stationary, spatially correlated, random fields of soil parameter values. In this chapter, the exponential Markov correlation function has been used to model the correlation between the parameter values at different locations:

$$\rho(\tau) = exp\left(-\frac{2}{l}\tau\right) \tag{5.10}$$

where τ is the lag distance between two points at different locations in space within the random field, and l is the scale of fluctuation.

The Monte Carlo Method (MCM) has been used to investigate the characteristics of the slope stability under stochastic transient seepage. Each Monte Carlo simulation involves multiple realisations of the problem, in which each random field is based on the same set of statistics, but yields a unique representation of the spatial variation in a material property. Individual random fields are generated for each

soil parameter in standard normal space, and then transformed into physical space. The random field cell values of the parameters, generated by LAS, are mapped onto the finite element mesh at the Gauss point level.

In this investigation, for the purpose of comparing non-hysteretic and hysteretic responses, 1000 realisations was found to be sufficient, as well as being consistent with other studies, e.g. Griffiths and Fenton (2004), Hicks and Spencer (2010) and Santoso et al. (2011).

5.4. Slope stability example

A heterogeneous embankment subjected to cyclic external water level fluctuation has been taken as an example to demonstrate the influence of the combined effect of hysteresis and heterogeneity on slope stability. For comparative purposes, the investigation has also included non-hysteretic and homogeneous analyses.

The geometry of the embankment is shown in Figure 5.2. Its height is $12\ \mathrm{m}$, and the width of its crest and base are $4\ \mathrm{m}$ and $52\ \mathrm{m}$, respectively. The embankment experiences a water level fluctuation on its upstream side. WL1 and WL2 are the highest and lowest water levels, whereas line A–A (at $x = 34\ \mathrm{m}$) and point B (at $x = 28\ \mathrm{m}$) denote the observation cross-section and point where results are recorded. The downstream water level remains at foundation level ($z = 0\ \mathrm{m}$), and the bottom boundary of the embankment is impermeable and fixed.

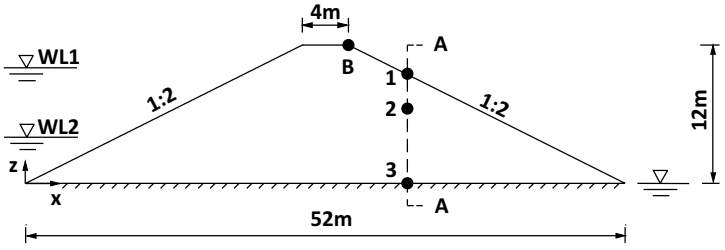

Figure 5.2: Geometry of the embankment.

The water level fluctuation with time has been simulated by the summation of two sinusoidal curves with two different frequencies (denoted by functions C_1 and C_2 in Figure 5.3). For both curves, the mean and amplitude are $3.5\ \mathrm{m}$ and $3\ \mathrm{m}$ respectively, whereas the time period of C_1, termed T_1 (and equal to 10 days), is three times that of C_2. The resulting water level fluctuation, shown by the green line in Figure 5.3, has a maximum water level of $10\ \mathrm{m}$ (WL1) and a minimum water level of $4\ \mathrm{m}$ (WL2).

The parameter values of the deterministic homogenous case, in which the spatial variability of parameters is not included, are listed in Table 5.1, with the SWRC properties following Yang et al. (2011a) and the mechanical properties following Hicks and Spencer (2010). The specific gravity is typical of an organic soil, i.e. ~ 2, as is the hydraulic conductivity, at $1 \times 10^{-6}\ \mathrm{m/s}$. The SWRC is given in Figure 5.4. In the non-hysteretic case, the drying property values are used (as explained in Section 5.5.1). For the heterogeneous case, in which several hydraulic parameters

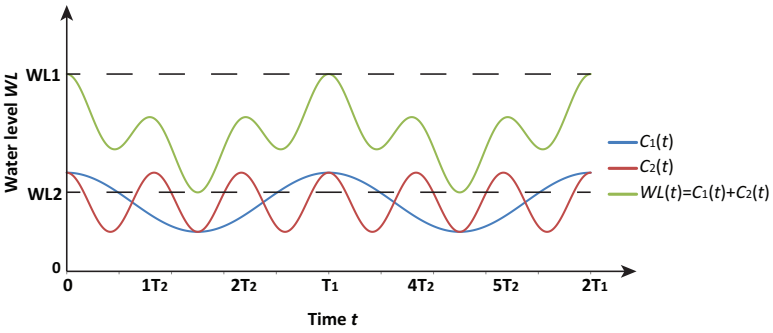

Figure 5.3: Water level fluctuation simulated by the sum of two sinusoidal curves.

are spatially random, the distributions of these parameters are listed in Table 5.2. Nielsen et al. (1973), Freeze (1975) and ASCE (2008) have shown that k_{sat} can be assumed to be log-normally distributed, and a $COV_{k_{sat}}$ of 0.9 to 1.0 was reported in Nielsen et al. (1973). α_d has also been described as log-normally distributed (Carsel and Parrish, 1988; Russo and Bouton, 1992; De Rooij et al., 2004) and, in Carsel and Parrish (1988), COV_{α_d} is from 0.203 to 1.603. Russo and Bouton (1992) suggested a normal distribution for n, while Carsel and Parrish (1988) indicated that COV_n is from 0.033 to 0.203. De Rooij et al. (2004) showed that the distribution of θ_s is log-normal, while Carsel and Parrish (1988) reported that COV_{θ_s} is from 0.15 to 0.355. In De Rooij et al. (2004), COV_{θ_r} is equal to 0.031 and the distribution is assumed to be log-normal.

Table 5.1: Parameter values for the homogenous case.

Parameter	Symbol	Unit	Value
Saturated hydraulic conductivity	k_{sat}	m/d	0.0864
VGM parameter for the main drying (and non-hysteretic) curve	α_d	m^{-1}	0.1
VGM parameter for the main wetting curve	α_w	m^{-1}	0.2
Fitting parameter for VGM model	n	-	1.226
Saturated VWC	θ_s	-	0.38
Residual VWC	θ_r	-	0.0038
Slope of the scanning curve	κ	-	0.00006
Stiffness	E	kPa	1.0×10^5
Poisson's ratio	ν	-	0.3
Effective cohesion	c'	kPa	15
Effective friction angle	ϕ'	^{0}	20
Specific unit weight	G_s	-	2.02

Note: VGM represents the van Genuchten–Mualem model described in Section 5.2.2.

Table 5.2: Statistical distributions of the hydraulic parameters

Parameter	k_{sat}[m/d]	α_d[m^{-1}]	n[−]	θ_s[−]	θ_r[−]
Distribution	Lognormal	Lognormal	normal	Lognormal	Lognormal
μ	0.0864	0.1	1.226	0.38	0.0038
σ	0.0864	0.05	0.08	0.06	0.0002
COV	1.0	0.5	0.065	0.16	0.053

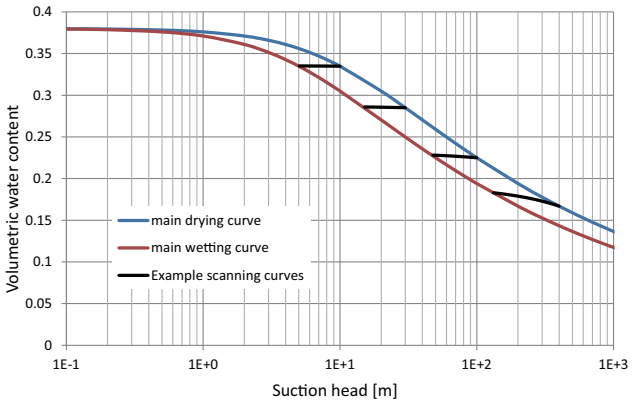

Figure 5.4: SWRC used in the analyses.

5.5. Results

In the following numerical investigation, the effects of hysteresis, parameter variation and heterogeneity are systematically investigated. In Section 5.5.1, hysteresis in isolation, i.e. a homogenous embankment, has been studied, in Section 5.5.2 the influence of the variable parameters is investigated and in Section 5.5.3 the impact of hysteresis on a spatially variable embankment has been presented. Table 5.3, summarises the items investigated in each sub-section.

Table 5.3: Outline of numerical investigation

Sub-section	Hysteresis	Parameter sensitivity	Spatial variability
5.1	✓		
5.2	✓	✓	
5.3	✓		✓

5.5.1. Influence of hysteresis on the seepage and stability of a homogeneous embankment

Several analyses were initially undertaken to find an optimal mesh size and time step which would ensure both accuracy and efficiency. A standard finite element size of 0.5 m (vertical) by 1.0 m (horizontal) was selected and the time step was chosen to be 0.05 d.

The hysteretic water retention behaviour significantly influences the water flow and soil suction distributions in the embankment, and thereby the slope stability. Figure 5.5 shows the variation of the FOS with time. It increases from the initial conditions, illustrating the benefit of undertaking transient analysis. For both the hysteretic and non-hysteretic cases, the FOS is seen to react to the change in water level, where, if the water level is high, the FOS is low and vice versa. Figure 5.5 shows that, at any instant in time, the FOS of the hysteretic case is always smaller than that of the non-hysteretic case, due to the selection of the main drying curve as the starting point of the transient seepage analysis for both cases. The reason for choosing the main drying curve is that Ebel et al. (2010) reported it to be the most easily measured in the laboratory and therefore the most frequently used. In addition, in the numerical example, the embankment first experiences water level drawdown, i.e. a drying process. If the non-hysteretic SWRC is instead taken to be the wetting curve, a difference in the FOS between the non-hysteretic and hysteretic cases would still exist, although the FOS of the hysteretic case would then be bigger than that of the non-hysteretic case.

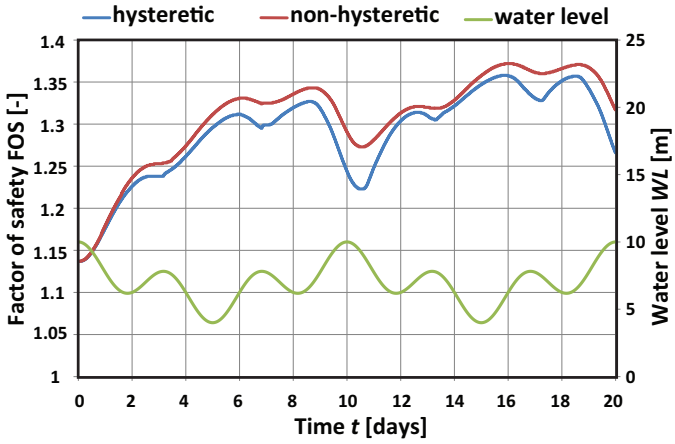

Figure 5.5: FOS variation with time.

In Figure 5.5, the hysteretic case reacts quicker to changes in water level due to the variation of VWC with suction moving along the scanning curve, and this, in general, leads to a more significant and faster reduction in the FOS when the water level rises. The largest difference coincides with the highest water level and lowest FOS (ignoring the first part which is affected by the initial conditions). It is emphasised that, in this analysis, all properties are constant throughout the domain

and no heterogeneity is considered. Section 5.5.3 provides a demonstration of the impact of considering heterogeneity alongside hysteresis.

Figure 5.6 compares the PWP head and VWC variation with time between the non-hysteretic and hysteretic cases, at three depths along cross-section A–A (see Figure 5.2). It can be seen that the VWC of the hysteretic case is usually larger or equal to that of the non-hysteretic case, and that the PWP head of the hysteretic case is also usually larger or equal to the non-hysteretic case. The larger the VWC, the larger the overturning moment due to the greater soil weight; in addition, the smaller suction head results in a smaller shear resistance to sliding. Therefore, the combined effects lead to the FOS in the hysteretic case being smaller than in the non-hysteretic case (Figure 5.5).

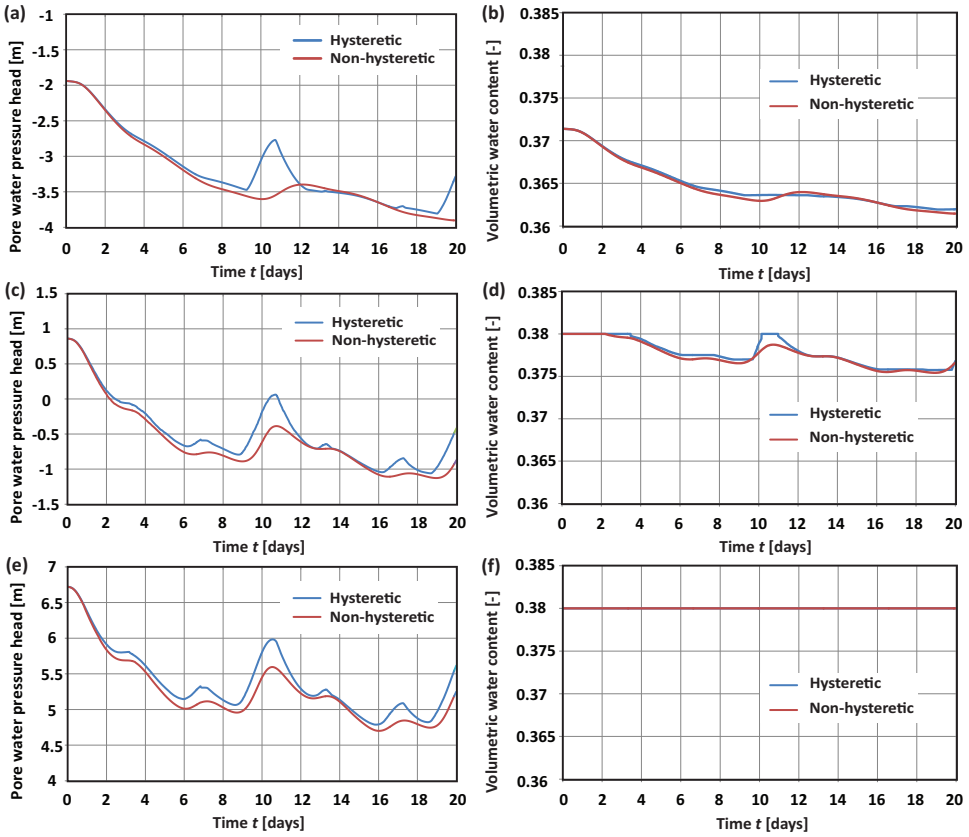

Figure 5.6: PWP head and VWC versus time at different depths (points 1 – 3 in Figure 5.2): (a) and (b) $z_1 = 9$ m; (c) and (d) $z_2 = 6$ m; and (e) and (f) $z_3 = 0$ m.

In Figure 5.6, it is seen that the PWP head in the hysteretic case can change more rapidly than that in the non-hysteretic case, due to the suction head moving along the scanning curves. In addition, it can be seen that the pore pressures are more sensitive to boundary condition (i.e. external water level) changes in the

hysteretic case, with a similar change for different depths as seen from the blue curves in the left plots of Figure 5.6. In the non-hysteretic case, the red curve describing the highest point (Figure 5.6 (a)) does not change significantly with a change of boundary condition, whereas that describing the lowest point is almost as sensitive as in the hysteretic case. The response delay of the non-hysteretic case during transient seepage can be explained by referring to the wetting and drying process in a soil column (Yang et al., 2011a, 2012a).

The state at any point in the slope domain may be categorised into three types: always unsaturated, saturated–unsaturated and always saturated. The suction variations at typical points representing these three cases are illustrated in Figure 5.7, which shows the variation of the VWC with suction for points 1–3 shown in Figure 5.2. Figures 5.7(a) and (b) denote point 1 which is always in the unsaturated condition; Figures 5.7(c) and (d) denote point 2 which changes between saturated and unsaturated conditions; and Figures 5.7(e) and (f) denote point 3 which is always in the saturated condition. In Figure 5.7, it can be noted that the suction in the hysteretic case shows larger variation than that in the non-hysteretic case, due to the suction head varying in the area enclosed by the main drying and wetting curves.

5.5.2. Relative importance of hydraulic parameters

To investigate the hydraulic parameters that are here represented by statistical distributions, i.e. $\boldsymbol{X} = [k_{sat},\ \alpha_d,\ n,\ \theta_s,\ \theta_r]$, a sensitivity analysis has been undertaken to assess their relative importance on the embankment response under both non-hysteretic and hysteretic conditions. Gardner et al. (1981) suggested the use of the correlation coefficient derived from Monte Carlo simulation to evaluate the relative importance of the input parameters on the output. Hence, one thousand values from the distribution of each parameter (Table 5.2) have been randomly sampled, and assembled into a 1000×5 input matrix:

$$\begin{bmatrix} \boldsymbol{X}_1 \\ \vdots \\ \boldsymbol{X}_{1000} \end{bmatrix} = \begin{bmatrix} k_{sat,1} & \alpha_{d,1} & n_1 & \theta_{s,1} & \theta_{r,1} \\ \vdots & & \ddots & & \vdots \\ k_{sat,1000} & \alpha_{d,1000} & n_{1000} & \theta_{s,1000} & \theta_{r,1000} \end{bmatrix} \tag{5.11}$$

No correlation is assumed between the parameters, although physically likely due to the dependence on grain size, minerology and density, as the purpose of this investigation is to assess which of the parameters is important in controlling the system response.

Each combination of the random values of the five parameters (one row in the matrix) were utilised in a transient seepage analysis (with the domain being taken as homogeneous). The Pearson correlation coefficient was then utilised to give a measure of the correlation between two variables, and is defined as

$$\rho_{x_i,\mathrm{FOS}} = \frac{COV(x_i, \mathrm{FOS})}{\sigma_{x_i}\sigma_{\mathrm{FOS}}} = \frac{E[(x_i - \mu_{x_i})(\mathrm{FOS} - \mu_{\mathrm{FOS}})]}{\sigma_{x_i}\sigma_{\mathrm{FOS}}} \tag{5.12}$$

where x_i is the ith random variable in $\boldsymbol{X}$, $\rho_{x_i,\mathrm{FOS}}$ is the Pearson correlation coefficient, $COV(x_i, \mathrm{FOS})$ is the covariance of the two variables, and σ_{x_i} and σ_{FOS} are the standard deviation of x_i and FOS, respectively.

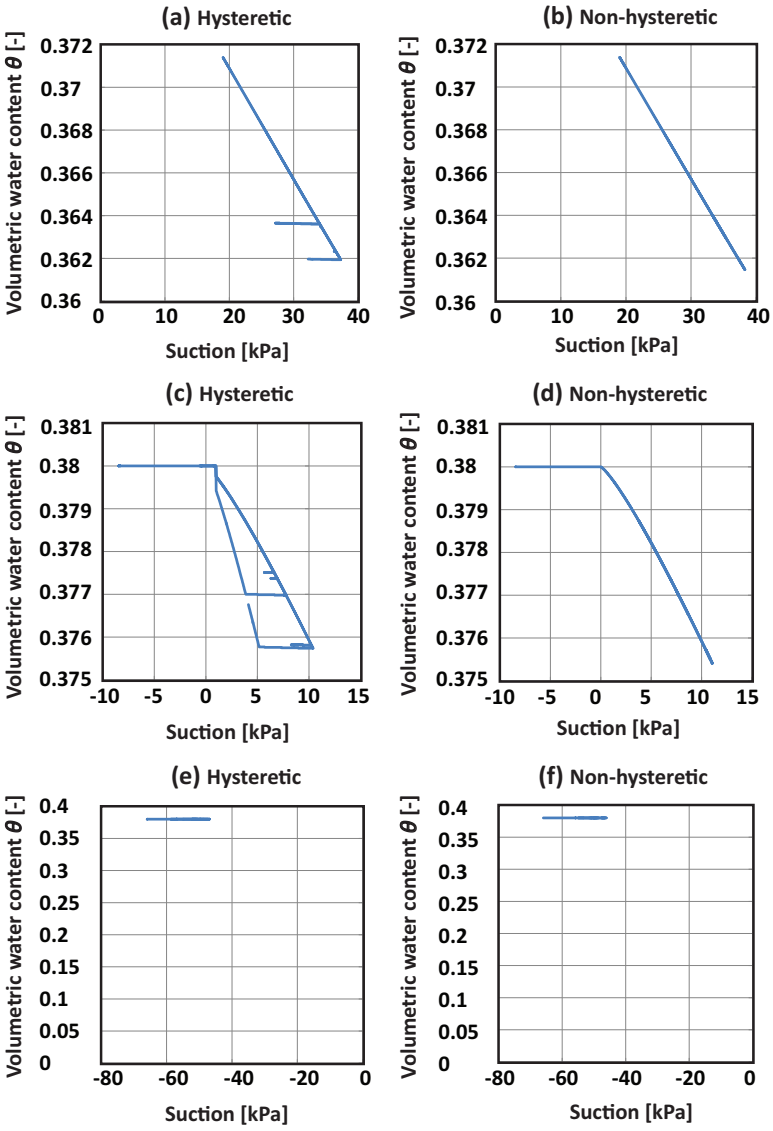

Figure 5.7: VWC versus suction at points along profile A–A at different depths: (a) and (b) $z_1 = 9$ m; (c) and (d) $z_2 = 6$ m; and (e) and (f) $z_3 = 0$ m.

Figure 5.8 shows the Pearson correlation coefficients between the FOS and different hydraulic parameters for the non-hysteretic case at time $t = 2\mathrm{T}_2$. The black values are for the entire data set and the red values are for FOS below 1.25. It can be seen that the FOS increases with an increase in k_{sat}, but decreases with increasing α_d, n and θ_s. The positive relationship between k_{sat} and FOS is because, when k_{sat} is large, the outflow of water is faster, leading to a higher FOS. The negative

correlations between FOS and α_d, n and θ_s may be explained with the aid of Figure 5.9, which illustrates the sensitivity of the SWRC equation to the different parameters, and by recalling that a lower FOS is generally obtained for higher VWC and lower suction. With reference to Figure 5.9, for curves ① and ②, the only difference is in the value of parameter θ_s, where $\theta_{s1} > \theta_{s2}$. An increase in θ_s means that the detained water in the embankment increases, which induces a lower FOS. For curves ② and ④, the only difference is parameter α_d, where $\alpha_{d2} < \alpha_{d4}$. For the same VWC, the suction is larger for α_{d2} and this causes a higher FOS. For curves ② and ③, the only difference is parameter n, where $n_2 < n_3$. For the same VWC, the suction is larger for n_2 and this causes a higher FOS. Figure 5.8 shows that θ_r has almost no influence on the FOS, because the suction cannot reach the range of values where the value of θ_r has a large influence. The values of the Pearson correlation coefficients for $\mathrm{FOS} < 1.25$ were calculated to investigate whether FOS closer to failure had similar correlations to those of the whole dataset. All trends are similar, in that positive correlations remain positive and vice versa, although the correlations are lower due to the removal of higher calculated FOS. However, there is still a strong positive correlation between FOS and k_{sat}.

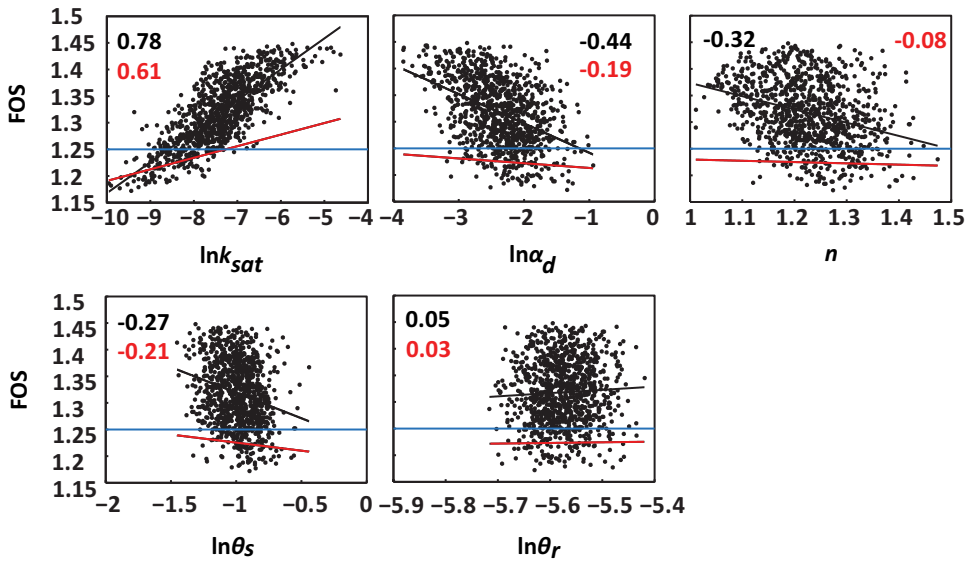

Figure 5.8: Correlation between FOS and different hydraulic parameters for non-hysteretic case at $t = 2\mathrm{T}_2$.

Figure 5.10 shows the correlation coefficients as a function of time. The left vertical axis applies to the solid lines and the right axis applies to the dashed lines. In Figure 5.10, the correlation coefficients significantly decrease for three hydraulic parameters, i.e. for k_{sat}, α_d and n, whereas the correlation for θ_s and θ_r remain fairly stable. This is due to the impact of the propagation of water in the embankment, induced by the upstream water level fluctuation, towards the downstream.

Parameter	Curves	Relation
θ_S	1, 2	$\theta_{S1} > \theta_{S2}$
α_d	2, 4	$\alpha_{d2} < \alpha_{d4}$
n	2, 3	$n_2 < n_3$

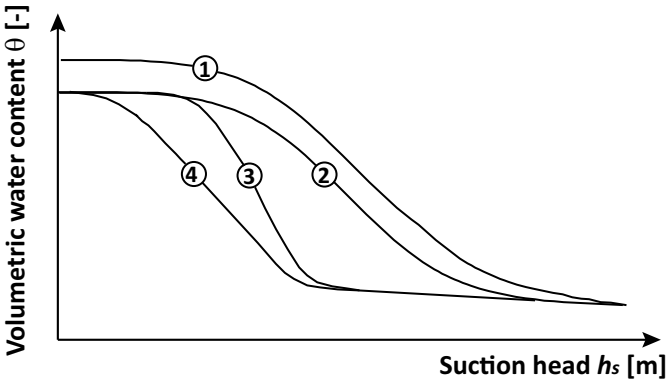

Figure 5.9: Sensitivity of the SWRC equation to model parameters.

At the end of the first main cylce ($\mathrm{T}_1 = 10$ d) the water level has returned to its highest point, so that the unsaturated zone in the sliding area has become smaller. In addition, the water flowing into the embankment due to the increasing external water level has not had time to drain out from the downstream side. These factors result in the FOS reducing, even when k_{sat} is relatively high and α_d and n are relatively small. Hence, when the data of the three parameters versus FOS, for $t = \mathrm{T}_1 = 3\mathrm{T}_2$, are plotted in the same way as in the first three plots in Figure 5.8 (though not shown here), the dots become more scattered and the correlation coefficients decrease.

As was seen in Figure 5.8, Figure 5.10 shows that the saturated hydraulic conductivity has the largest influence on the FOS, while the residual VWC has almost no influence. Indeed, the correlation coefficient between the FOS and k_{sat} remains high in comparison with the other parameters, even at its lowest point, which indicates that k_{sat} plays a dominant role in the final computation of the FOS. Therefore, only the heterogeneity of k_{sat} has been incorporated into the transient seepage analysis in the following section. This conclusion is also supported by other studies reported in literature. Rahardjo et al. (2007) pointed out that the saturated hydraulic conductivity played a dominant role in rainfall infiltration compared to other hydraulic parameters. Avanidou and Paleologos (2002) and Chen et al. (1994a,b) also suggested that the saturated hydraulic conductivity was the most important parameter in unsaturated heterogeneous soils. Zhang et al. (2005) studied rainfall-induced slope failure in a heterogeneous slope. In the study, only the saturated hydraulic conductivity, saturated volumetric water content, the parameter related to the air entry value and the slope of the water retention curve were considered to be variable, because these four parameters were considered to be important and influence the computation of slope stability. The residual volumetric water content

was considered to be not important.

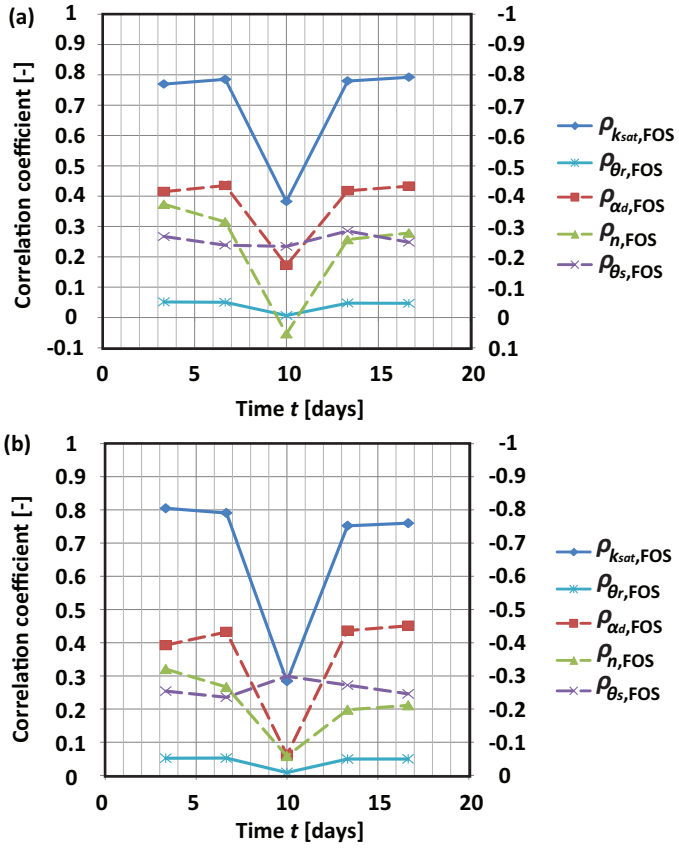

Figure 5.10: Correlation coefficients between FOS and different hydraulic parameters at several specific times: (a) non-hysteretic case and (b) hysteretic case.

5.5.3. Influence of hysteresis on the seepage and stability of a heterogeneous embankment

In this section, a spatially variable saturated hydraulic conductivity is used and both hysteretic and non-hysteretic SWRCs are considered; all other parameters are constant. As an indicative example, the scale of fluctuation, $l_{\ln k_{sat}}$, has been taken to be 1.0 m in both the vertical and horizontal directions, i.e. giving isotropic variability, and 1000 realisations have been performed. Note that, for more comprehensive conclusions on the influence of spatial variability, further studies are needed.

Influence of hysteresis on stochastic seepage

In Figure 5.11, the VWCs at Point B from Figure 5.2 at $t = \mathrm{T}_1 = 10$ d are compared (one dot from each realisation), with the blue dots representing the non-hysteretic

case and the red dots representing the hysteretic case. It can be seen from Figure 5.11 that the results of the hysteretic case show larger variation. The variation is also not limited along a single line in θ–h_s space, as in the non-hysteretic case, but varies in a wider area. Note that, because k_{sat} was the only randomized parameter, the main drying curve in the SWRC is the same for both the non-hysteretic and hysteretic cases. This means that, in the non-hysteretic case, the spatial variability can only cause the scattering of blue dots located along the main drying curve in the SWRC. However, in the hysteretic case, the hysteretic behaviour allows the suction to vary along the scanning curve. When the spatial variability is added into the hysteretic effect, this causes the suction to vary in the area enclosed by the main drying and wetting curves.

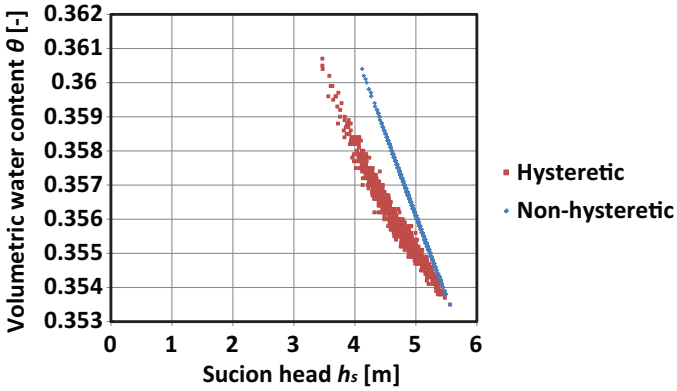

Figure 5.11: VWC versus suction head at Point B at $t = \mathrm{T}_1 = 10$ d based on 1000 realisations.

Influence of hysteresis on the stability of the heterogeneous slope

The factor of safety has been calculated for each realisation and a log-normal distribution fitted to the resulting ensemble distribution of FOS. Table 5.4 gives the mean μ_{FOS} and standard deviation σ_{FOS} of the FOS for both the non-hysteretic and hysteretic cases. The mean of the FOS at all times was smaller for the hysteretic case than for the non-hysteretic case. In addition, the standard deviation of the FOS was usually higher for the hysteretic case. The reason is that, in the hysteretic case, the hysteresis in the water retention behaviour induced much more variation in the PWP and VWC, because the PWP and VWC could vary in the area enclosed by the main drying and wetting curves. Therefore, the uncertainty in the FOS is larger for the hysteretic case.

Figure 5.12 shows the cumulative distribution functions (CDF) of FOS for both the non-hysteretic (dashed line) and hysteretic cases (solid line) at different times. The limit value of the FOS (dash-dotted line) represents the FOS calculated in a homogeneous non-hysteretic analysis based on the mean value of k_{sat}. From the results in Figure 5.12, it is seen that if a deterministic method is used to analyse the safety of the embankment slope, there is a high probability of overestimating the FOS (in this case, by up to 20% compared to a 95% reliability). Moreover,

Table 5.4: Statistical information of the FOS based on 1000 realisations

Case	Time t	μ_{FOS}	σ_{FOS}	Case	Time t	μ_{FOS}	σ_{FOS}
Hysteretic	$1\mathrm{T}_2$	1.199	0.0374	Non-hysteretic	$1\mathrm{T}_2$	1.221	0.0364
	$2\mathrm{T}_2$	1.233	0.046		$2\mathrm{T}_2$	1.278	0.045
	$\mathrm{T}_1 = 3\mathrm{T}_2$	1.182	0.0467		$\mathrm{T}_1 = 3\mathrm{T}_2$	1.245	0.0488
	$4\mathrm{T}_2$	1.232	0.049		$4\mathrm{T}_2$	1.274	0.0475
	$5\mathrm{T}_2$	1.253	0.0535		$5\mathrm{T}_2$	1.311	0.0529

based on the comparison between the solid and dashed lines, it can be concluded that, if only the heterogeneity is considered while the hysteretic effect in the SWRC is ignored, the computed probability of slope failure would be lower. This proves that, although the contribution to the variation in results due to the uncertainties in the material properties and the hysteresis can be different (the former factor could be larger if there are strong uncertainties in the parameters), both factors play an important role and should be considered in the analysis.

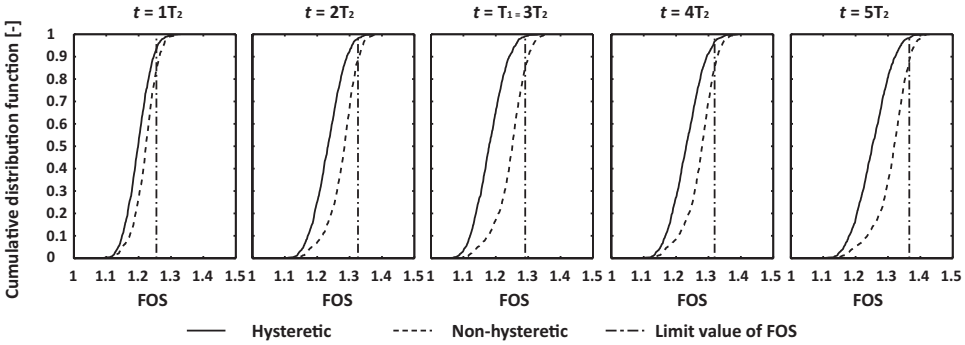

Figure 5.12: Cumulative distribution functions (CDFs) for both non-hysteretic and hysteretic cases at different times. The solid line is the CDF for the hysteretic case and the dotted line for the non-hysteretic case. The dash-dotted line shows the factor of safety calculated without considering heterogeneity or hysteresis.

5.6. Conclusions

The combined effect of hysteresis in the water retention behaviour and heterogeneity of an unsaturated soil on the stability of an embankment under transient seepage has been investigated. The stability and reliability of the embankment show significant differences with analyses which ignore either or both of these factors.

Under the influence of both hysteresis and heterogeneity, the PWP and VWC in the transient seepage process have a larger variation than would otherwise be the case. Considering slope stability, in the initially drying condition, the mean of the FOS for the hysteretic case is smaller than that of the non-hysteretic case. Moreover, the standard deviation of the FOS is usually larger. It has been found that,

due to hysteresis in the water retention behaviour, the influence of the heterogeneity of soil property values on slope stability could be amplified. Furthermore, in the sensitivity analysis of hydraulic parameters, it was found the saturated hydraulic conductivity, k_{sat}, plays a dominant role in slope stability compared to other hydraulic parameters. Further studies on the impact of spatial variability on these processes are needed to provide comprehensive conclusions.

6

Probabilistic Analysis of Seepage Velocity Distribution under Earth Embankments for Internal Stability

Internal stability, or piping, has been attributed as a major cause of dam and embankment failures. Current national prediction models to predict piping use the hydraulic gradient between the upstream and downstream water levels as an indicator. No explicit consideration is made regarding preferential pathways, although piping usually initiates from a discrete downstream location and recent research indicates that piping happens when the water velocity reaches a critical value. The local seepage velocity is strongly related to the inherent spatial variability, or heterogeneity, of the soil. Based on stochastic seepage analysis, local velocities in and under an embankment are investigated. The results show that, when the coefficient of variation of hydraulic conductivity is small, the location of the maximum local velocity is typically near the downstream toe of the embankment, as for a deterministic analysis. In contrast, increasing the coefficient of variation scatters the possible locations of the maximum local velocity. Two typical situations are identified: one situation where the maximum local velocity is close to the downstream ground surface, and the other where the maximum local velocity is far from the downstream ground surface and located near the center of the foundation soil layer. In the first situation it is easier to reach a critical value to initiate piping because the maximum local velocity is near the ground surface, but it is also relatively easy to protect against. In contrast,

Parts of this chapter have been published in *Proceedings of 5th International Symposium on Geotechnical Safety and Risk*, 671-676 (2015) (Liu et al., 2015a).

in the second situation it is easier to form a passage for piping development once piping is initiated. This is due to the velocity increasing towards the center of the foundation. Additional analyses have demonstrated that the heterogeneity of the hydraulic conductivity not only increases the exit gradient of the velocity, but also influences the global kinetic energy and kinetic energy distribution significantly.

6.1. Introduction

Piping has been attributed as a major cause of dam failures, with about half of all failures being due to piping (Foster et al., 2000). It usually happens in the presence of a water barrier, with a high water level on one side and a low level on the other. The hydraulic head difference induces a water flow in the structure (Sellmeijer and Koenders, 1991) and, when the flow reaches a critical rate, it starts to erode soil particles from the downstream surface (piping initiation). Subsequently, the internal erosion progresses in the upstream direction and a piping channel or slit is formed (piping development). Finally, if the piping process does not come to a halt, the erosion channels progress to the upstream surface, and then the erosion through the channels can accelerate significantly and the water barrier can be "undermined" and collapse.

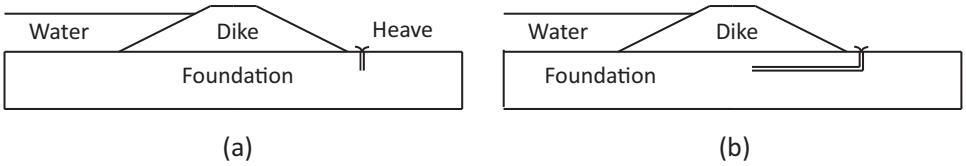

Figure 6.1: Sketch of piping initiation (a) and piping development (b).

Accurate analysis of whether piping is going to happen is essential in the design and management of water barriers. Figure 6.1 briefly shows the process of piping initiation and development. Current models to predict piping initiation and development are Bligh's model, Lane's model and Sellmeijer's model (Bligh, 1910; Lane, 1935; Sellmeijer and Koenders, 1991). The first two are empirical, whereas the latter is conceptual (Sellmeijer, 2006). However, all these models use the hydraulic gradient as an indicator of the state governing piping occurrence. Bligh's model relates the hydraulic head difference across the structure, H_c, to the length of the seepage path, L. The critical value of the ratio H_c/L is related to the soil type. Lane's model is similar to Bligh's model, except that it accounts for the horizontal and vertical seepage lengths separately, in order to account for the influence of the different permeabilities in the horizontal and vertical directions. In Sellmeijer's model, the critical value of H_c/L is related to additional factors, which include the sand bedding angle, the sand particle size and the geometry of the water barrier. However, piping normally initiates from a very local downstream position. Therefore, local bahaviour close to the downstream ground surface is important, and this is strongly related to the inherent heterogeneity of the soil.

Recent research has illustrated that hydraulic velocity is an indicator of piping potential (Sivakumar Babu and Vasudevan, 2008), and can be an improvement to using simply the hydraulic gradient (Richards and Reddy, 2012). The velocity is a function of both the hydraulic conductivity and hydraulic gradient. However, due to the heterogeneity of hydraulic conductivity, the hydraulic gradient across the entire structure cannot be seen as directly proportional to local velocity, and therefore the local velocity distribution within the domain is of interest and forms the main focus

of this chapter.

The chapter investigates the local velocity distribution under an earth embankment, induced by the spatial variability of the foundation hydraulic conductivity, and considers its influence on the potential for piping. Section 6.2 introduces stochastic seepage computed by RFEM. Section 6.3 presents stochastic analyses of velocity distribution, including a parametric study relating to the statistics of hydraulic conductivity. Section 6.4 includes a discussion on the influence of soil heterogeneity on piping. Section 6.5 calculates the exit gradient related to the piping initiation. Section 6.6 investigates the kinetic energy distribution in the whole domain under the influence of heterogeneity.

6.2. Stochastic seepage analysis

The local velocity distribution is computed in a seepage analysis. In this chapter, a 2D steady state seepage problem with constant boundary conditions has been analysed. The governing equation of steady state groundwater flow in 2D is shown in Equation 3.1.

The equation is spatially discretised using the FEM with the Galerkin weighted residual method. A no-flow condition in the unsaturated zone is assumed for simplicity and an iterative procedure (Chapuis and Aubertin, 2001; Chapuis et al., 2001) has been adopted to determine the phreatic surface and exit points on the downstream surface of the embankment.

6.3. Probabilistic analysis of seepage in and under an embankment

The example 2D steady state seepage problem analysed herein is shown in Figure 6.2. A $4\ \mathrm{m}$ high earth embankment is constructed on a $5\ \mathrm{m}$ deep foundation overlying a firm base. The width of the embankment crest and foundation are $4\ \mathrm{m}$ and $40\ \mathrm{m}$, respectively. The upstream and downstream side slopes are both $1{:}2$, and the upstream and downstream water levels are $4\ \mathrm{m}$ and $0\ \mathrm{m}$, respectively (where the coordinate origin is at the top left corner of the foundation). For simplicity, the embankment is considered to be homogenous and only the foundation is heterogeneous. This is also because the main focus is on the role of the foundation in the seepage process. Although the geometry of the embankment and foundation are symmetrical, the problem is not symmetrical because of the boundary conditions and the heterogeneous hydraulic conductivity profile in the foundation.

The hydraulic conductivity of the embankment and mean hydraulic conductivity of the foundation are both chosen to be $10^{-6}\ \mathrm{m/s}$, consistent with a sand material. Duncan (2000) suggested that the coefficient of variation ($COV_k = \sigma_k/\mu_k$) of hydraulic conductivity of saturated clay is $68-90\%$, whereas Zhu et al. (2013) suggested that, for saturated sand, it is $60-100\%$. However, in order to get a detailed overview of the influence of the coefficient of variation of hydraulic conductivity on the statistical characteristics of the maximum local velocity, a much wider range of COV_k was used; i.e. $COV_k = \sigma_k/\mu_k = 0.1, 0.5, 1.0, 2.0, 3.0, 4.0, 5.0, 6.0$. The degrees

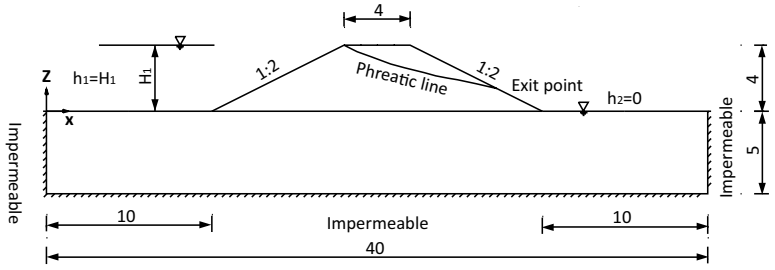

Figure 6.2: Geometry of the embankment and foundation (dimensions in m).

of anisotropy of the heterogeneity considered were $\xi = \theta_h/\theta_v = 1, 8, 20$ (where subscripts h and v refer to the horizontal and vertical directions, respectively), and the vertical scale of fluctuation has been fixed at $\theta_v = 1.0\ \mathrm{m}$. The mesh for the FEM computation uses four node quadrilateral elements of size $0.5\ \mathrm{m}$ by $0.5\ \mathrm{m}$, except for some distorted elements to model the upstream and downstream slope surfaces. The cell size in the random field generation is half of the FE mesh size, so that each of the four integration points in every finite element has a different cell value from the random field.

Figure 6.3 shows typical random fields of the hydraulic conductivity, k, for two degrees of anisotropy, in which the darker zones represent lower values of k. Figure 6.3 shows that, when the degree of anisotropy increases, the local variation of the hydraulic conductivity is not as great. Of course, when the COV_k increases, the range of the hydraulic conductivity also increases.

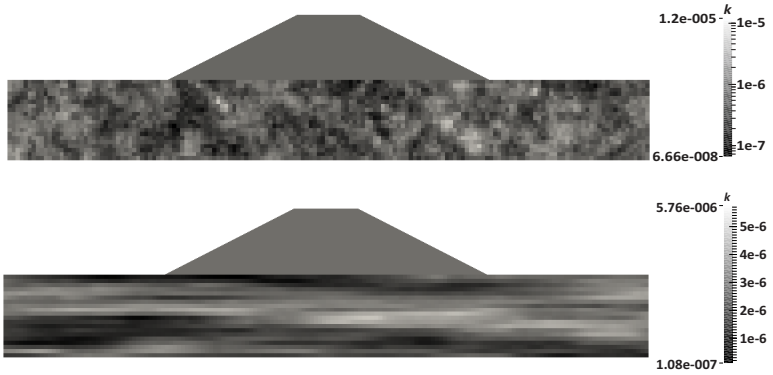

Figure 6.3: Example random fields for different hydraulic conductivity statistical values (unit: $\mathrm{m/s}$): (a) Typical random field for $COV_k = 1.0$ and $\xi = 1$; (b) Typical random field for $COV_k = 1.0$ and $\xi = 20$.

In each realisation, the velocity was calculated at the four integration points of each element, and the maximum local velocity within the foundation was identified. The statistical results of the velocity distributions for 500 and 1000 realisations were compared for selected values of the coefficients of variation and degrees of anisotropy (i.e. $COV_k = 1.0, 6.0$ and $\xi = 1, 8, 20$), and little difference was found in

the results of the mean and standard deviation of the maximum velocity (see Table 6.1). Therefore, 500 realisations were deemed adequate to get reasonable results for the complete range of input statistics considered. Figure 6.4 further illustrates the close agreement between using 500 and 1000 realisations, by showing example histograms of the maximum velocity, in which the continuous lines represent fitted lognormal distributions. It is seen that the lognormal distributions fit the histograms reasonably well. Figures 6.5 and 6.6 show the computed velocity distributions for two typical realisations.

Table 6.1: Mean and standard deviation of maximum velocities based on different numbers of realisations for different COV_k and ξ.

COV	ξ	500 realisations		1000 realisations	
		$\mu_{v_{max}}$ (m/s)	$\sigma_{v_{max}}$ (m/s)	$\mu_{v_{max}}$ (m/s)	$\sigma_{v_{max}}$ (m/s)
1.0	1	0.9741×10^{-6}	0.3663×10^{-6}	0.9724×10^{-6}	0.3497×10^{-6}
	8	0.9412×10^{-6}	0.3616×10^{-6}	0.9373×10^{-6}	0.3609×10^{-6}
	20	0.9231×10^{-6}	0.4073×10^{-6}	0.9143×10^{-6}	0.3770×10^{-6}
6.0	1	1.1338×10^{-6}	0.6495×10^{-6}	1.1335×10^{-6}	0.6189×10^{-6}
	8	1.1372×10^{-6}	0.8384×10^{-6}	1.1343×10^{-6}	0.8310×10^{-6}
	20	1.1678×10^{-6}	1.1687×10^{-6}	1.1561×10^{-6}	1.1488×10^{-6}

The mean, $\mu_{v_{max}}$, and standard deviation, $\sigma_{v_{max}}$, of the maximum local velocity are influenced by the statistical values of the foundation hydraulic conductivity. Figures 6.7 and 6.8 show that $\mu_{v_{max}}$ and $\sigma_{v_{max}}$ are functions of the coefficient of variation of the foundation hydraulic conductivity COV_k. In Figure 6.7, $\mu_{v_{max}}$ is not sensitive to ξ. The value of $\mu_{v_{max}}$ is larger than the deterministic maximum local velocity, $v_{maxd} = 6.86 \times 10^{-7}$ m/s, for all values of COV_k considered. This is due to the water preferring a path with a low resistance to flow through, and that, under the same hydraulic gradient, a lower resistance path causes a higher velocity. In a heterogeneous domain the local variation of the hydraulic conductivity is significant compared to the uniform hydraulic conductivity in a homogeneous domain (based on the mean). In Figure 6.7, $\mu_{v_{max}}$ initially increases with increasing COV_k, after which a slight decrease occurs. The velocity is a function of the hydraulic conductivity and hydraulic gradient. It can be seen from Figure 6.9 that, due to the lognormal statistics, the hydraulic conductivity distribution curves shift to the left with an increasing σ_k (indicated by an increasing COV_k). When σ_k is relatively small, i.e. $COV_k < 3$, the distribution becomes wider with an increase in σ_k. This means that the maximum value of the hydraulic conductivity increases, whereas the minimum value decreases. The increasing range of possible values for the hydraulic conductivity could cause the local hydraulic gradient to become larger, and this could be the reason for the local increase of velocity. However, when COV_k is greater than 4.0, the distribution curves become narrower. It can be seen from Figure 6.9 that the maximum value of the hydraulic conductivity also starts to decrease at higher values of COV_k, which may be the reason for the slight decrease of $\mu_{v_{max}}$ in Figure 6.7. Figure 6.8 shows that $\sigma_{v_{max}}$ increases monotonically with an increase in COV_k

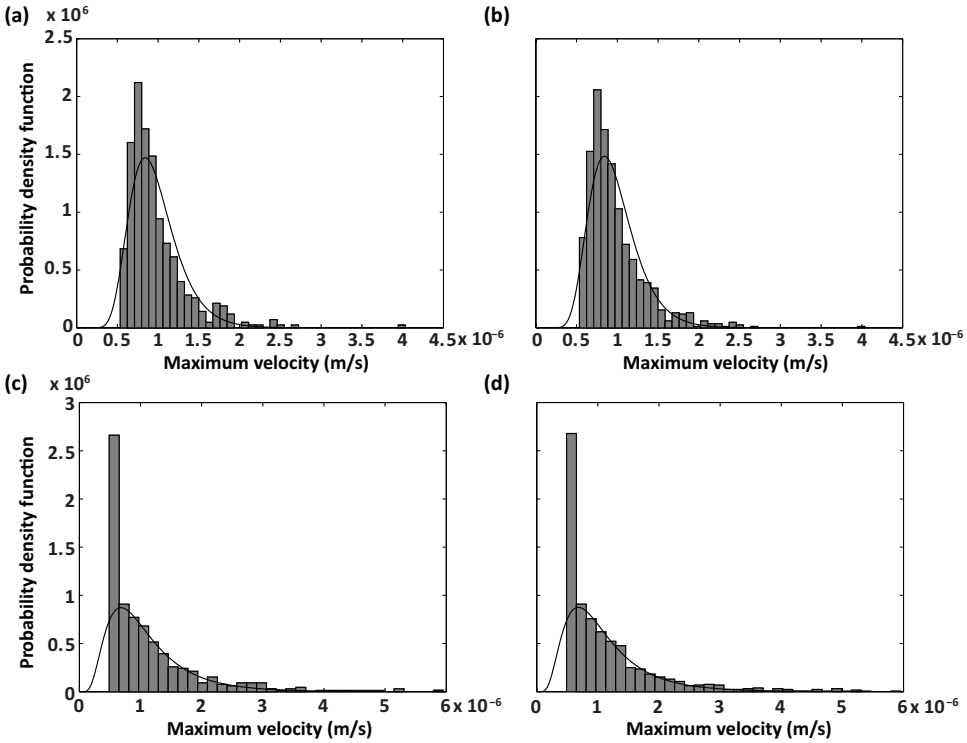

Figure 6.4: Probability density functions of the maximum velocity: (a) 500 realisations, $COV_k = 1.0$ and $\xi = 1$; (b) 1000 realisations, $COV_k = 1.0$ and $\xi = 1$; (c) 500 realisations, $COV_k = 6.0$ and $\xi = 8$; and (d) 1000 realisations, $COV_k = 6.0$ and $\xi = 8$.

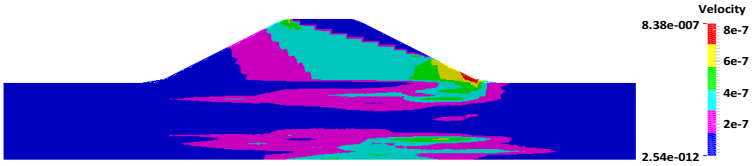

Figure 6.5: Typical realisation in which the maximum local velocity is close to the slope toe ($COV_k = 1.0$ and $\xi = 20$) (unit: m/s).

and that, for the same value of COV_k, $\sigma_{v_{max}}$ increases with an increase in ξ.

6.4. Brief discussion of local velocity distribution with reference to piping

The previous section analysed the general features of the local velocity distribution due to the spatial variability of the foundation hydraulic conductivity, e.g. the distribution of maximum local velocity based on 500 realisations and its sensitivity to

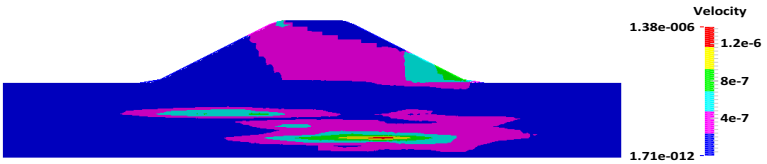

Figure 6.6: Typical realisation in which the maximum local velocity is near the centre of the foundation ($COV_k = 1.0$ and $\xi = 20$) (unit: $\mathrm{m/s}$).

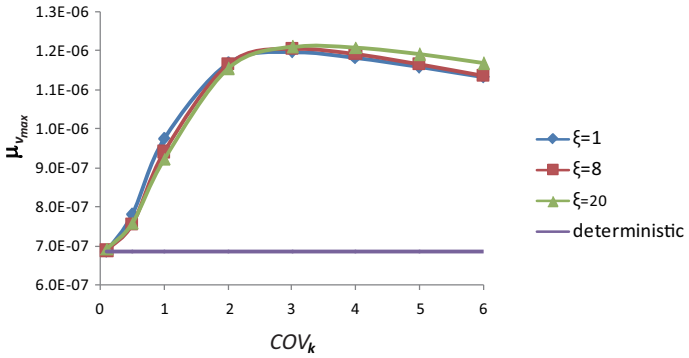

Figure 6.7: Mean of the maximum local velocity versus COV_k of the foundation.

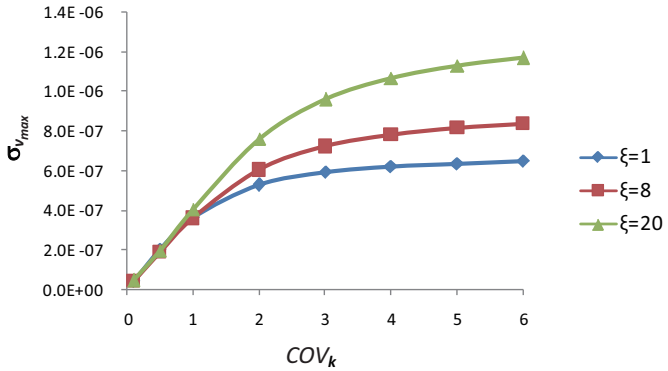

Figure 6.8: Standard deviation of the maximum local velocity versus COV_k of the foundation.

different input statistics. However, the value of the maximum local velocity is only one necessary condition for piping. Another factor is the location of the maximum local velocity.

This section investigates the location of the maximum local velocity in all realisations, which is strongly influenced by the variability of the foundation hydraulic conductivity. Among the realisations, those cases which have the maximum local

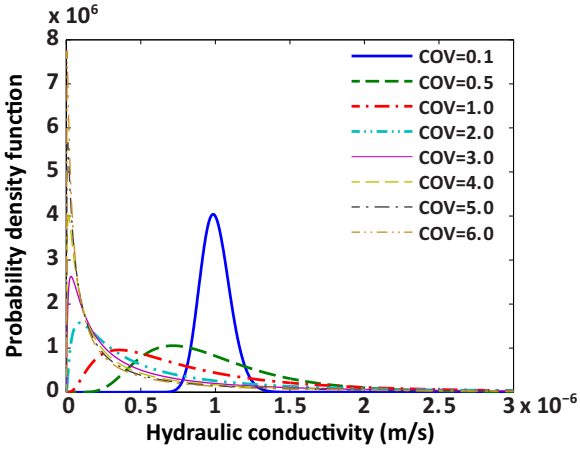

Figure 6.9: Probability density functions of hydraulic conductivity for different COV_k.

velocity near the ground surface on the downstream side are more inclined to initiate piping. Therefore, this section highlights several special situations in which different locations of the maximum local velocity are found.

When the COV_k of the foundation hydraulic conductivity is quite small, i.e. $COV_k = 0.1$, the locations of the maximum local velocity from 500 realisations are found to aggregate into a small area, independent of the degree of anisotropy, ξ. This area is located near the downstream slope toe, as seen in Figure 6.10. In the figure, coloured blocks are used to represent the Gauss points and different coloured blocks represent the frequency of occurrence of the maximum local velocity from 500 realisations. This aggregation is reasonable considering the small variation of the foundation hydraulic conductivity over the whole domain. When the variation of the foundation hydraulic conductivity is small, the whole field is similar to the homogeneous case. For a homogeneous field, the maximum local velocity is also at the downstream slope toe (as in Figure 6.10), and is controlled by the geometry and boundary conditions. A simple engineering solution that may be applied in this case is to provide toe protection.

Figure 6.10: Locations of the points with maximum local velocity from 500 realisations ($COV_k = 0.1$ and $\xi = 1$).

When the COV_k increases to 1.0 and the degree of anisotropy is $\xi = 20$ (or $\xi = 1,\ 8$), the locations of the maximum local velocity from 500 realisations are more scattered over the domain, as seen in Figure 6.11, although still focused towards the toe. This is due to the significant variation of the foundation hydraulic conductivity in the random fields. Among the 500 realisations, two typical situations can be identified. One is when the maximum local velocity happens close to the ground surface (Figure 6.5); the other is when the maximum local velocity happens under the dyke (Figure 6.6), at a wide variety of locations. Hence the location of the maximum local velocity is not as simple to determine as in the situation when the COV_k is small (i.e. $COV_k < 1.0$), in which the maximum local velocity aggregates into a small area near the downstream slope toe. For $COV_k > 1.0$, the spatial distribution of maximum velocity locations is similar to Figure 6.11, based on 500 realisations.

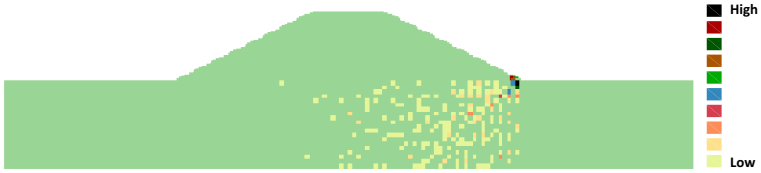

Figure 6.11: Locations of the points with maximum local velocity from 500 realisations ($COV_k = 1.0$ and $\xi = 20$).

Figure 6.5 shows that the maximum local velocity is close to the ground surface, whereas Figure 6.6 shows that the location of the maximum local velocity may be, in certain cases, far from the ground surface. As mentioned already, piping occurrence can be linked to critical hydraulic velocity. In the first situation it is easier to reach a critical value to initiate piping because the maximum local velocity is near the ground surface. In contrast, in the second situation it is easier to form and maintain a passage for piping development once piping has been initiated. This is due to the velocity towards the center of the foundation increasing. If piping has been initiated near the toe in the second situation, the higher velocity near the center of the foundation may worsen the situation and promote piping progression. Note that Kanning (2012) investigated the path of piping progression, by linking flow velocity with the spatial variability of soil grain size in developing a criterion for assessing the potential for soil erosion. Although not considered in this thesis, the linkage of spatial variability in both velocity (due to hydraulic conductivity) and grain size is a logical future step forward.

6.5. Exit gradient related to piping initiation

In the previous section, the influence of the spatial variability of hydraulic conductivity on the local velocity distribution has been qualitatively discussed in relation to the maximum local velocity and piping initiation or progression. This section will present a quantitative analysis related to the piping initiation.

Terzaghi (1922) proposed a theoretical criterion to calculate the critical exit gradient, i_c, for piping initiation. It is valid for internally stable soils (in which the grain-size distribution is good) and defined as

$$i_c = (1 - n_p)\left(\frac{\rho_s - \rho_w}{\rho_w}\right) \tag{6.1}$$

where n_p is the porosity, and ρ_s and ρ_w are the density of the soil solids and water, respectively.

Van Beek et al. (2014) presented an extensive survey, based on previous laboratory experiments and field tests relating to the study of piping and critical exit gradients. The results of i_c were compiled, with all values being around 1.0 to 1.1. Terzaghi's criterion does not include the effects of spatial variability. However, in the analysis of Van Beek et al. (2014), it was pointed out that spatial variability could be the cause of the scatter in the interpretation of experimental results (e.g. Figure 6.12 taken from Van Beek et al. (2014)).

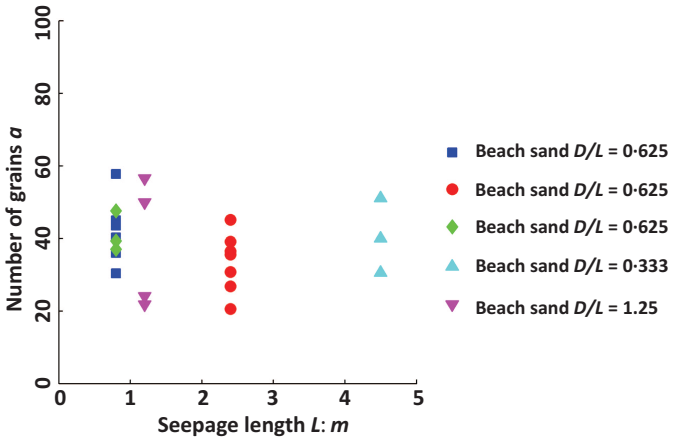

Figure 6.12: Calculated exit distance ($dx = a * d_{50}$) versus seepage length (Van Beek et al., 2014).

The distribution of local water velocity has been considered to be an index to predict piping in previous literature, because it accounts for the combined effect of hydraulic conductivity and hydraulic gradient. Therefore, instead of i_c, the critical local velocity, v_c, has been used here to predict piping initiation. The v_c is assumed to be derived from i_c and the mean hydraulic conductivity. Hence, in order to predict piping initiation, the local velocity along the downstream boundary (Figure 6.13) has been investigated.

In Figure 6.13, the local velocity in the hatched boundary area is used to predict piping initiation. The maximum local velocity in the hatched area, v^b_{max}, is compared to the calculated critical velocity, v_c, and the factor of safety (FOS) relating to piping initiation is defined as:

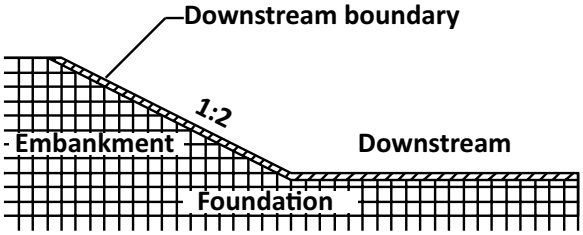

Figure 6.13: Downstream area relating to piping initiation.

$$\text{FOS} = \frac{v_c}{v_{max}^b} \tag{6.2}$$

where $v_c = \mu_k i_c = 1.0 \times 10^{-6} \times 1.0 = 1.0 \times 10^{-6}$ m/s, in which i_c has been selected to be 1.0 in this example.

Figure 6.14 shows the PDF and cumulative distribution function (CDF) of the FOS related to piping initiation when $COV_k = 1.0$ and $\xi = 1$. The vertical solid line in Figure 6.14 (a) indicates the FOS when the foundation is considered to be homogenous, i.e. $\text{FOS} = 1.0 \times 10^{-6}/6.86 \times 10^{-7} = 1.46$. It can be seen that the heterogeneity has a significant influence on the estimation of the FOS. In Figure 6.14 (b), when the FOS is smaller than 1.0 it is considered that piping initiation will occur, so that the probability of failure in this case is 17.6%. Figure 6.15 shows the comparison of the position of the v_{max}^b between the homogenous and heterogeneous cases. The solid and open circles represent the Gauss points of the finite elements, with the red open circle denoting the location of v_{max}^b for the homogenous case. For the heterogeneous case ($COV_k = 1.0$ and $\xi = 1$), the possible locations also include the blue open circles in Figure 6.15.

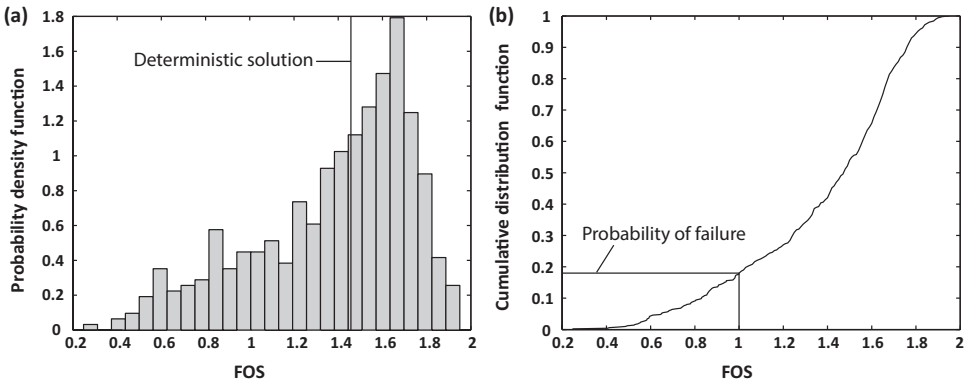

Figure 6.14: PDF and CDF of FOS related to piping initiation ($COV_k = 1.0$ and $\xi = 1$).

Figure 6.16 summarises the probability of failure as a function of both COV_k and ξ. For all cases, it is found that the probability of failure increases with increasing

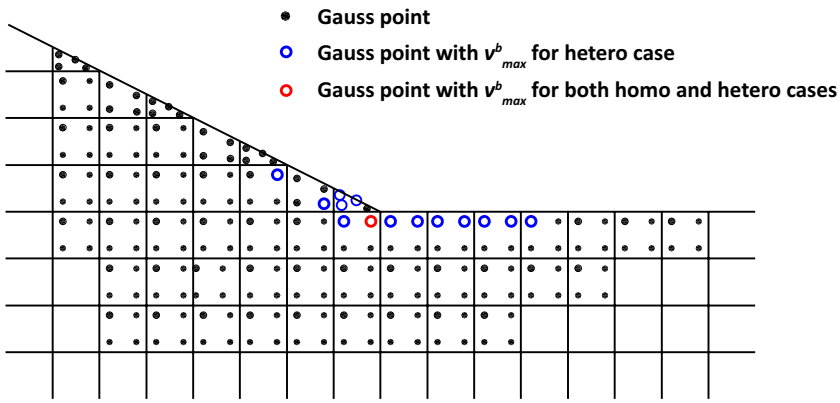

Figure 6.15: Close-up of the downstream toe area showing the locations of v^b_{max} as open circles (COV_k = 1.0 and ξ = 1).

COV_k when the COV_k is smaller than 1.0, but then decreases for larger values of COV_k. This can be explained based on the results of the previous sections. The reason for the increase is that, when COV_k is smaller than 1.0, the maximum local velocity of the whole domain, v_{max}, aggregates in a small area near the downstream slope toe. Specifically, it only occurs at a few Gauss points (see Figure 6.17 (a)) and, therefore, v_{max} is generally equal to v^b_{max} (relating to the hatched area defined in Figure 6.13). In addition, the variation of the hydraulic conductivity is limited within a smaller range when COV_k is small and v_{max} is dominated by the range of the hydraulic conductivity. Because of these two reasons, when COV_k increases from 0.1 to 1.0, the range of the hydraulic conductivity becomes larger so that it causes a higher maximum local velocity over the whole domain, which is the reason for the increase of v^b_{max}. The increase of v^b_{max} causes the increase in the probability of failure.

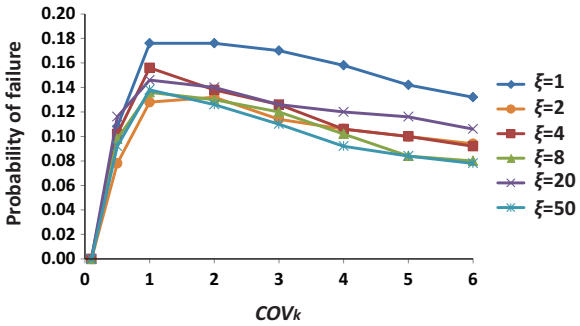

Figure 6.16: Probability of failure as a function of COV_k and ξ.

When COV_k is greater than 1.0, the location of v_{max} is scattered throughout the whole foundation. Meanwhile, there is no significant difference in the mean of v_{max}

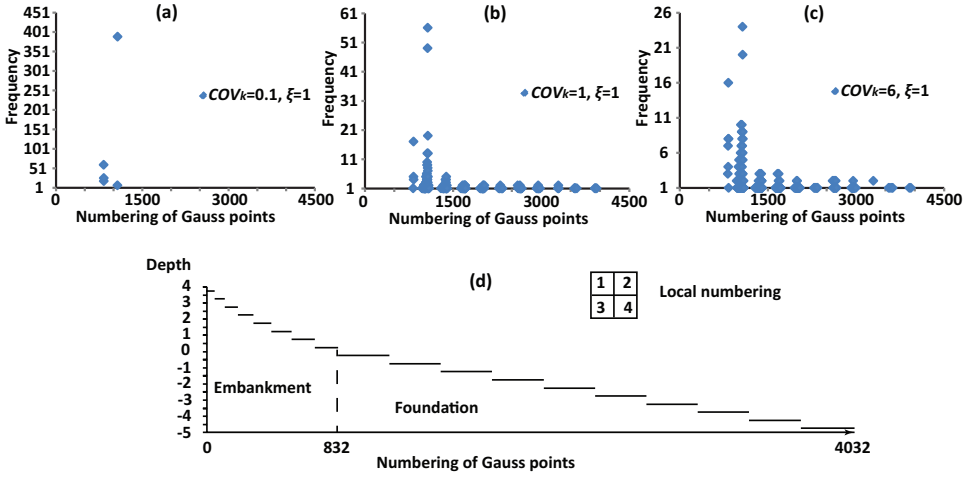

Figure 6.17: Frequency and locations of Gauss points with v_{max} for different COV_k.

when COV_k is greater than 1.0 (Figure 6.7). However, the scattering is much more obvious with the increase of COV_k (see Figure 6.17 (b) and (c)), which leads to a smaller v_{max}^b. Due to this reduction, the probability of failure initiation decreases when COV_k is greater than 1.0.

In Figure 6.16, there is no obvious tendency for a variation of the probability of failure of piping initiation with the degree of anisotropy for anisotropic cases, although there is a difference between the isotropic ($\xi = 1$) and anisotropic cases, i.e. there is a reduction when $\xi > 1$. The reason for the difference between isotropic and anisotropic cases may be that, for anisotropic fields, there could be preferential horizontal flow which would reduce the local velocity upwards. However, Figure 6.16 shows negligible difference between the anisotropic analyses possibly because of v_{max}^b being only studied in a thin layer of elements at the downstream boundary and the degree of anisotropy affecting the distribution of the hydraulic conductivity over the whole foundation. Fenton and Griffiths (2008) also found that the exit gradient of a water retaining structure shows no clear variation with the scale of fluctuation of the hydraulic conductivity (for their analyses based on isotropic spatial variability).

6.6. Influence of heterogeneity on the kinetic energy of seepage

Richards and Reddy (2014) proposed a method which uses the kinetic energy to predict the initiation of piping. In this section, the influence of the heterogeneity on the kinetic energy is investigated.

The local kinetic energy of the water, E_l, is defined as

$$E_l = \frac{1}{2} M_f v_s^2 \tag{6.3}$$

where M_f is the mass of fluid and v_s is the pore seepage velocity. The v_s is calculated from the computed Darcy flow velocity v:

$$v_s = \frac{q}{A_p} = \frac{vA}{A_p} = \frac{v}{n_p} \tag{6.4}$$

where q is the discharge, A_p is the area of the voids in the cross-section, and A is the total area of the cross-section.

Equations 6.3 and 6.4 can be combined as

$$E_l = \frac{1}{2} M_f v_s^2 = \frac{1}{2} \rho_w V n_p \left(\frac{v}{n_p} \right)^2 = \frac{1}{2} \rho_w V \frac{v^2}{n_p} \tag{6.5}$$

where V is the volume of soil and, since it is a 2D plane strain problem, $V = A$. The global kinetic energy E_g is the integral of E_l across the whole domain.

In Figure 6.18, the PDFs and CDFs of E_g, when $COV_k = 1.0$ and $\xi = 1,\ 20$, are shown. The vertical solid line indicates the value of E_g when the foundation is homogeneous, i.e. $E_{g,homo} = 1.07 \times 10^{-8}$ J. Figure 6.18 shows that heterogeneity of the hydraulic conductivity can result in a larger global energy compared to that of the homogeneous case. In addition, the largest value in the distribution can be significantly larger than the smallest value.

Figure 6.19 shows the distribution of E_l for the homogeneous case, whereas Figure 6.20 shows the realization of E_l, and the corresponding random field of hydraulic conductivity, for the realisation (out of 500) for which E_g is the maximum (for both sets of input statistics illustrated in Figure 6.18). It can be seen from the hydraulic conductivity field, in Figure 6.20 (b), that the higher local hydraulic conductivity forms a passage of preferential flow (indicated by the red line) which generates higher E_l (Figure 6.20 (a)). For comparative purposes, Figure 6.21 shows similar results for three other realisations when $COV_k = 1.0$ and $\xi = 1$, corresponding to E_g being the 2nd, 5th and 10th largest among the 500 realisations. In Figure 6.20 (d), the higher local hydraulic conductivity at the center of the foundation causes the higher E_l at the center (Figure 6.20 (c)). A comparison between Figures 6.19 and 6.20 shows that the heterogeneity of the hydraulic conductivity not only increases the value of the E_l, but also influences its spatial distribution significantly. In addition, it can be seen that the area of higher E_l in the heterogeneous foundation is larger than that in the homogeneous foundation, especially for the larger value of ξ.

The results in Figures 6.18 and 6.20 show that, for higher degree of anisotropy, the global kinetic energy is likely to increase and the connected elevated zones are also likely to increase, which increases the likelihood of piping to grow if initiated.

Figure 6.22 shows the variation of the mean of E_g against COV_k for $\xi = 1,\ 20$. For $\xi = 1$, the figure shows that the mean of E_g decreases with an increase in COV_k, and can be explained by the earlier Figure 6.9. As COV_k increases, the

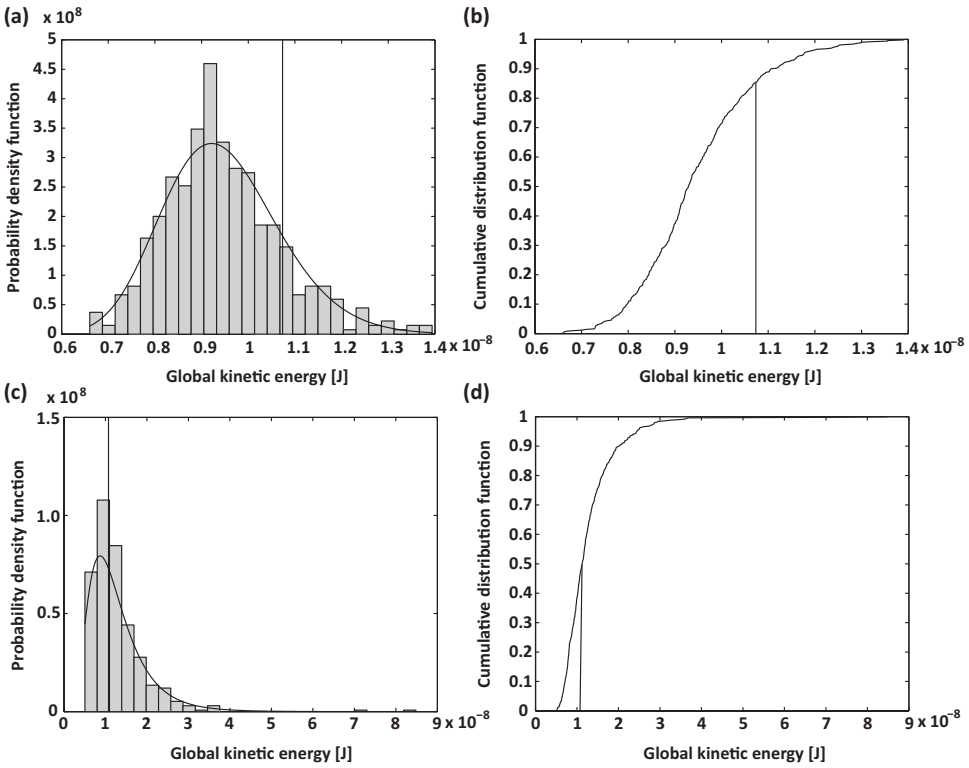

Figure 6.18: PDFs and CDFs of E_g: (a) PDF for $COV_k = 1.0$ and $\xi = 1$; (b) CDF for $COV_k = 1.0$ and $\xi = 1$; (c) PDF for $COV_k = 1.0$ and $\xi = 20$; and (d) CDF for $COV_k = 1.0$ and $\xi = 20$.

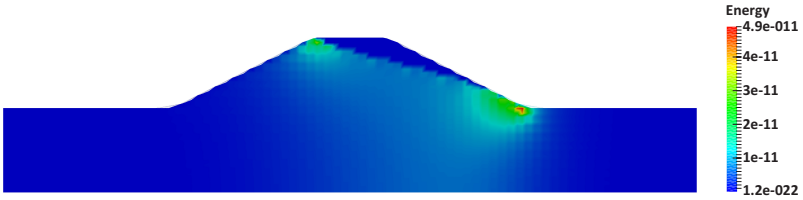

Figure 6.19: Distribution of E_l for homogeneous case (unit: J).

distribution of hydraulic conductivity shifts towards the left, so that smaller values of hydraulic conductivity are likely to be assigned to the random field cells. As E_g is the integral of E_l over the whole domain, the increased possibility of a small hydraulic conductivity decreases the value of E_g according to Equation 6.5. For $\xi = 20$, the connected elevated zone of kinetic energy increases due to the increased spatial correlation of hydraulic conductivity. This causes the mean of E_g to increase.

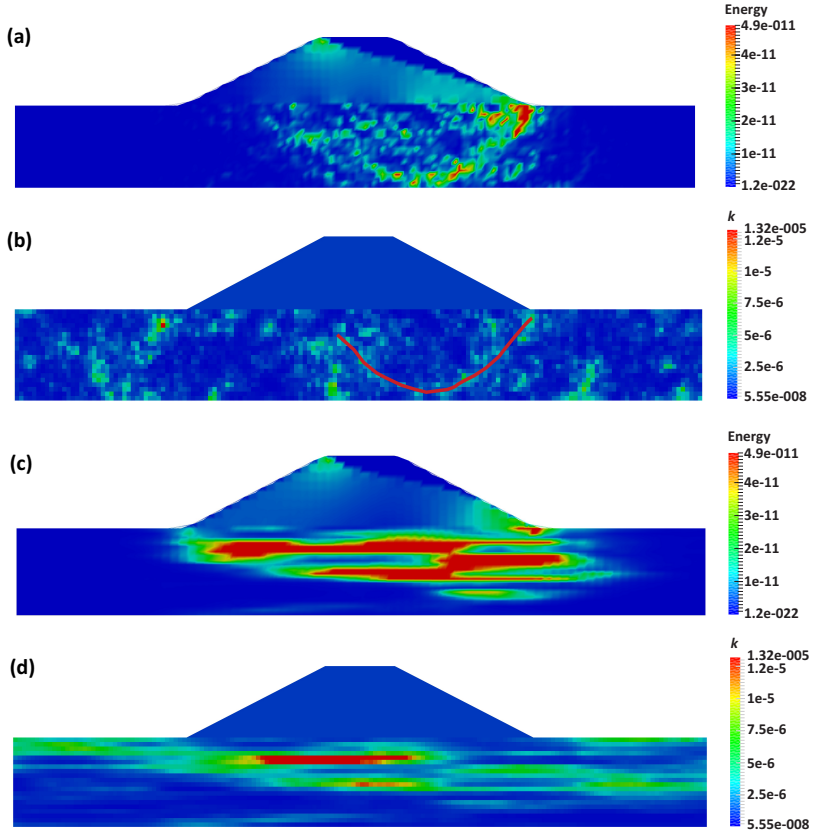

Figure 6.20: Realisation with the maximum global kinetic energy for $COV_k = 1.0$ and $\xi = 1$ ((a) and (b)) and $COV_k = 1.0$ and $\xi = 20$ ((c) and (d)): (a) kinetic energy (unit: J); (b) hydraulic conductivity (unit: m/s); (c) kinetic energy (unit: J); and (d) hydraulic conductivity (unit: m/s).

6.7. Conclusions

This chapter has briefly studied the influence of spatial variability, in the foundation hydraulic conductivity, on the local seepage velocity through and beneath an embankment. An investigation into the variability of a number of features known to influence the internal stability was presented, i.e. local velocity, hydraulic gradient and kinetic energy.

It has been shown that, when the foundation is only weakly heterogeneous with respect to hydraulic conductivity, it is easy to narrow down the zone in which piping may initiate. The maximum local velocity occurs in a small area close to the downstream slope toe and toe protection could be installed.

However, when the foundation shows strong heterogeneity in hydraulic conductivity the problem becomes more complex due to the significant variation of the maximum local velocity over the domain. Generally, this variation can be categorized into two types:

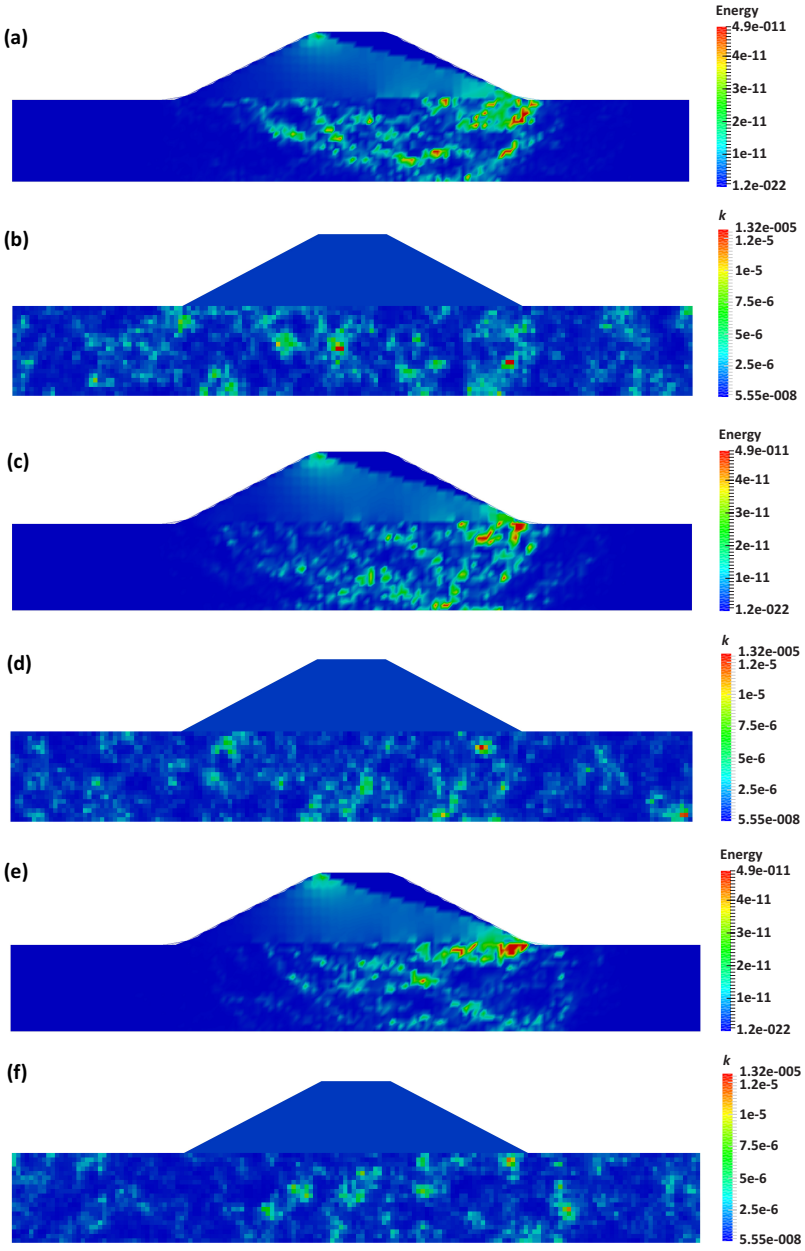

Figure 6.21: Realisations with high global kinetic energy for $COV_k = 1.0$ and $\xi = 1$: (a) 2nd highest (unit: J); (b) hydraulic conductivity (unit: m/s); (c) 5th highest (unit: J); (d) hydraulic conductivity (unit: m/s); (e) 10th highest (unit: J); and (f) hydraulic conductivity (unit: m/s)

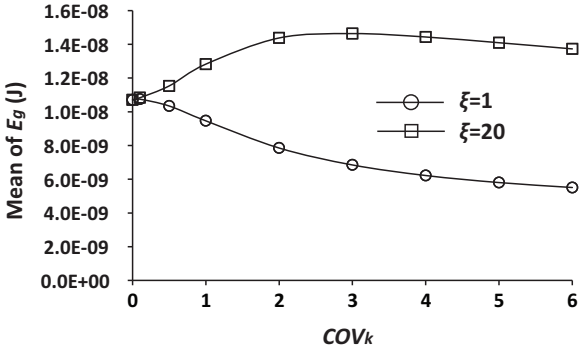

Figure 6.22: Mean of E_g versus COV_k for different degrees of anisotropy.

(1) The maximum local velocity is located under the foundation, far from the downstream ground surface. The high local velocity zone is surrounded by smaller velocity zones. It is easier to form a passage for piping development once piping is initiated due to a higher drag force;

(2) The maximum local velocity occurs near the downstream ground surface. It is easier to reach critical conditions to initiate piping.

In the quantitative analysis of the exit gradient and kinetic energy related to piping initiation, it was found that the heterogeneity of hydraulic conductivity increased the possibility of piping initiation. Due to the heterogeneity, the exit velocity gradient is generally higher than that of the homogeneous case. Meanwhile, in the computation of kinetic energy, it was found that the global kinetic energy E_g can also be higher than that of the homogeneous case and the distribution of the local kinetic energy E_l was significantly different from the homogeneous case. In addition, E_g decreases with an increase of COV_k; in particular, higher values of the degree of anisotropy lead, in general, to higher global levels of kinetic energy and pathways of locally elevated kinetic energy, which, in turn, leads to an increased risk of piping growth (once initiated).

7

Conclusions and Recommendations

7.1. Conclusions

Soil slopes under seepage are common geotechnical structures, e.g. dams or dykes. The seepage flow alters the stress state of the structures, thereby affecting their stability. However, this also offers an opportunity—pore pressure measurements are more simple (and cheaper) than stress/strain measurements—to better determine the material properties and therefore safety. Since natural soils are variable materials, deterministic methods of analysing slope stability, e.g. a single FOS, have significant disadvantages. Probabilistic methods, which have been developed since the 1960s, are gradually taking the place of deterministic methods. However, in probabilistic analyses of seepage and slope stability, the input values of soil parameters have errors because the field and laboratory tests of soil parameters are limited in number. Therefore, only a general distribution of the soil parameter values is often possible, with local spatial variability generally being difficult to capture. However, this approach often leads to large uncertainties and therefore conservative design. Inverse analysis, which makes use of observation data, can be used to improve the estimation of soil parameters (in general, and in space) and thereby reduce the statistical estimate of uncertainty in the prediction of slope stability. As soil properties used in analyses, e.g. cohesion, friction angle, hydraulic conductivity, etc., all derive from the soil composition, it is also logical that they are not independent. This can be used to further reduce uncertainties. Meanwhile, the complexity of the hydraulic behaviour of unsaturated soils increases the difficulty of saturated–unsaturated seepage analysis. In order to improve the estimation of unsaturated slope stability, a more realistic hydraulic model is required to simulate the flow in the soil.

In this thesis, a data assimilation method, called the EnKF, has been linked with a probabilistic method, i.e. RFEM, to reduce the statistical estimate of uncertainty existing in the stability analysis of a slope subjected to seepage. The proposed numerical approach makes use of hydraulic measurements (hydraulic head or pore water pressure in this thesis) to back-calculate the hydraulic parameters (hydraulic conductivity in this thesis). Based on the data assimilation, the local variability of hydraulic parameters can be better estimated. Also, the improved estimation of the hydraulic parameters results in a better estimation of the seepage behaviour and, as seepage behavour influences the stability of the structure, so a better estimation of the slope stability is possible. In addition, because of likely correlations between different soil parameters, the strength parameters (i.e. cohesion and friction angle) can also be improved based on the improved estimation of hydraulic parameters, and this in turn benefits the stability analysis. Furthermore, a more realistic hydraulic model is considered, which can simulate the hysteretic behaviour of unsaturated soils and better predict saturated–unsaturated seepage.

In all cases, by reducing uncertainty the range of calculated factors of safety is also reduced, and, in most cases, this improves the calculated reliability, even when the mean factor of safety reduced. It is seen that, as more information is used in the analyses, the statistical estimate of uncertainty reduces. This includes the better estimation of initial parameter distributions and more measurement data, both with respect to space and time.

In this work, only theoretical analyses have been undertaken and further experimental or field work is needed to confirm the findings and confirm the practicality of the method. Costs have also not been examined; however, although the cost of detailed instrumentation and advanced analysis are not insignificant, they are likely to be far cheaper in many cases than extensive refurbishment.

Specific conclusions regarding this thesis are listed as follows:

(i) A numerical approach, linking data assimilation (EnKF) with stochastic analysis (RFEM), has been proposed to reduce the statistical estimate of uncertainty in the stability analyses of slopes under steady or transient state seepage based on field hydraulic measurements. This approach proves that hydraulic measurements can be beneficial to slope stability estimation, in addition to the common way of using measured stress/strain response in inverse analyses, as conducted by previous researchers reported in the literature.

(ii) The EnKF improves the estimation of the hydraulic parameters. This leads to an improvement in the estimation of the seepage behaviour (including the pore water pressures), as well as in the estimation of strength parameters as long as there is cross-correlation between them.

(iii) When the EnKF is used, the input values used to generate the initial ensemble of unknown parameters needs careful selection in order to get a reasonable result. For example, the EnKF cannot work out the local variability of k_{sat} without considering the spatial variability in the input ensemble. It should be noted that, if the variation of a parameter is not estimated well, it is better to assume a larger standard deviation in order to get acceptable results. This is because it allows the generated initial ensemble values to cover a larger range, which helps in searching for the correct values of the parameter.

(iv) In transient seepage analysis, it has been found that the spatial continuity (reflected by the scale of fluctuation) has a significant influence on the back-calculated results via the EnKF. Even when the original standard deviations of the FOS are close to each other for different values of the scale of fluctuation, after using the EnKF, the updated estimation of the standard deviation of the FOS is clearly seen to be different.

(v) Hysteresis in the water retention behaviour of unsaturated soils causes a significant difference in the FOS between non-hysteretic and hysteretic cases. In stochastic saturated–unsaturated seepage analysis, k_{sat} is found to be the most influential parameter compared to other parameters used for the van Genuchten SWRC. When the heterogeneity of k_{sat} is considered at the same time, the distributions of FOS can be significantly affected, which, in turn, affects the estimation of slope reliability. Since the drying curve is generally used for a non-hysteretic analysis and the soil is assumed to be in the drying condition initially (Ebel et al., 2010; Tsai and Chen, 2010), the mean of the FOS for the hysteretic case is found to be smaller than that for the non-hysteretic case. Moreover, the standard deviation of the FOS is usually larger in hysteretic analysis.

(vi) The heterogeneity of hydraulic conductivity shows a significant influence on stochastic steady-state seepage, and specifically on the distribution of local velocity and kinetic energy. Due to the existence of heterogeneity, the maximum local velocity could occur at various locations within the structure, which affects the prediction of piping initiation and development. Analysis shows that the exit velocity gradient at the downstream boundary has an increased probability of exceeding the critical exit gradient because of the heterogeneous hydraulic conductivity, especially when degree of anisotropy is high.

7.2. Recommendations for future research

There are some aspects which have not been investigated in this thesis due to time and knowledge limitations. For future research, a few recommendations are listed as follows:

(i) The measurements used in the data assimilation in this thesis are synthetic, rather than real field observation data. The proposed framework to reduce the statistical estimate of uncertainty in the slope stability could be applied in a real project in future research.

(ii) Soil property correlations should be investigated. It is seen that knowledge of such correlations can reduce uncertainty/increase reliability, although the knowledge of such correlations is limited.

(iii) The seepage process does not consider the influence of soil deformation, i.e. it is an uncoupled seepage analysis. Therefore, for future work, a fully coupled seepage analysis would be interesting in which the influence of soil mechanical behaviour is incorporated. If there is measurement of strain or displacement, the inverse method can also be applied to back-calculate the mechanical parameters.

(iv) The seepage analysis could be extended to 3D. The heterogeneity of soil hydraulic parameters in the third dimension (i.e. perpendicular to the cross-section analysed in a 2D problem) increases the variability of the seepage behaviour, which may have a significant influence on the stability of a relatively long 3D slope.

(v) The data assimilation of seepage and the probabilistic analysis of slope stability are time-consuming processes, because multiple random fields have to be generated (and the problem analysed repeatedly) in order to model the range of possible responses due to the spatial variability of soil parameters. Parallel computing could be a useful and feasible option to increase the efficiency of such analyses.

(vi) Combining conditional random fields with the EnKF could also be interesting. The conditional random field can directly reduce the uncertainty of the hydraulic parameters as long as there are measurements of those parameters,

so the combination of these two methods can further improve the estimation of hydraulic behaviour and thereby the estimation of mechanical response.

(vii) The piping mechanism could be further investigated, so that a better knowledge of piping susceptibility and possible early warning of piping failure could be observed/predicted.

(viii) In this thesis, an elastic-perfectly-plastic model is used to simulate the soil mechanical behaviour. More complicated models could be used to better simulate the stress-strain behaviour, considering, for example, strain-softening behaviour. However, these models are known to cause grid dependence in FE solutions without special treatment. Future research should consider the influence of the soil model and heterogeneity on grid dependency, and investigate possible mitigation measures.

References

Ahmed, A. A. (2009). Stochastic analysis of free surface flow through earth dams. *Computers and Geotechnics*, 36(7):1186–1190.

Ahmed, A. A. (2012). Stochastic analysis of seepage under hydraulic structures resting on anisotropic heterogeneous soils. *Journal of Geotechnical and Geoenvironmental Engineering*, 139(6):1001–1004.

Alonso, E. E. (1976). Risk analysis of slopes and its application to slopes in Canadian sensitive clays. *Géotechnique*, 26(3):453–472.

Arnold, P. and Hicks, M. A. (2010). Stochastic modelling of unsaturated slope stability. In *Proceedings of the 5th International Conference on Unsaturated Soils, Barcelona, Spain*, pages 1237–1242.

Arnold, P. and Hicks, M. A. (2011). A stochastic approach to rainfall-induced slope failure. In *Proceedings of the Third International Symposium on Geotechnical Safety and Risk, Munich*, pages 107–115.

ASCE (2008). Standard guideline for fitting saturated hydraulic conductivity using probability density functions. In *ASCE Standard ASCE/EWRI 50-08, ASCE, Reston*.

Avanidou, T. and Paleologos, E. K. (2002). Infiltration in stratified, heterogeneous soils: Relative importance of parameters and model variations. *Water Resources Research*, 38(11):1232.

Baecher, G. B. and Christian, J. T. (2005). *Reliability and statistics in geotechnical engineering*. New York: John Wiley & Sons.

Bakr, A. A., Gelhar, L. W., Gutjahr, A. L., and MacMillan, J. R. (1978). Stochastic analysis of spatial variability in subsurface flows: 1. Comparison of one- and three-dimensional flows. *Water Resources Research*, 14(2):263–271.

Bartetzko, A. and Kopf, A. J. (2007). The relationship of undrained shear strength and porosity with depth in shallow (< 50 m) marine sediments. *Sedimentary Geology*, 196(1):235–249.

Bashir, R., Sharma, J., and Stefaniak, H. (2015). Effect of hysteresis of soil-water characteristic curves on infiltration under different climatic conditions. *Canadian Geotechnical Journal*, 53(2):273–284.

Bathe, K.-J. and Khoshgoftaar, M. R. (1979). Finite element free surface seepage analysis without mesh iteration. *International Journal for Numerical and Analytical Methods in Geomechanics*, 3(1):13–22.

Bishop, A. W. (1960). The principles of effective stress. *TekniskUkeblad*, 106(39):859–863.

Bjerrum, L., Kringstad, S., and Kummeneje, O. (1961). The shear strength of a fine sand. In *Proceedings of 5th International Conference on Soil Mechanics and Foundation Engineering, Paris*, pages 29–37.

Bligh, W. G. (1910). Dams, barrages and weirs on porous foundations. *Engineering News*, 64(26):708–710.

Bolzon, G., Fedele, R., and Maier, G. (2002). Parameter identification of a cohesive crack model by Kalman filter. *Computer Methods in Applied Mechanics and Engineering*, 191(25):2847–2871.

Burgers, G., van Leeuwen, P. J., and Evensen, G. (1998). Analysis scheme in the ensemble Kalman filter. *Monthly Weather Review*, 126(6):1719–1724.

Cai, F. and Ugai, K. (2004). Numerical analysis of rainfall effects on slope stability. *International Journal of Geomechanics*, 4(2):69–78.

Campanella, R. G., Martens, S., Tomlinson, S., and Davies, M. P. (1995). In-situ measurement of hydraulic conductivity in sands. In *Proceedings of 48th Canadian Geotechnical Conference, Canadian Geotechnical Society, Vancouver, BC*, volume 1, pages 309–318.

Carman, P. C. (1937). Fluid flow through granular beds. *Transactions of the Institution of Chemical Engineers*, 15:150–166.

Carsel, R. F. and Parrish, R. S. (1988). Developing joint probability distributions of soil water retention characteristics. *Water Resources Research*, 24(5):755–769.

Celia, M. A., Bouloutas, E. T., and Zarba, R. L. (1990). A general mass-conservative numerical solution for the unsaturated flow equation. *Water Resources Research*, 26(7):1483–1496.

Chapuis, R. P. and Aubertin, M. (2001). A simplified method to estimate saturated and unsaturated seepage through dikes under steady-state conditions. *Canadian Geotechnical Journal*, 38(6):1321–1328.

Chapuis, R. P., Chenaf, D., Bussière, B., Aubertin, M., and Crespo, R. (2001). A user's approach to assess numerical codes for saturated and unsaturated seepage conditions. *Canadian Geotechnical Journal*, 38(5):1113–1126.

Chen, W.-F. and Mizuno, E. (1990). *Nonlinear analysis in soil mechanics*. Amsterdam: Elsevier.

Chen, Y. and Zhang, D. (2006). Data assimilation for transient flow in geologic formations via ensemble Kalman filter. *Advances in Water Resources*, 29(8):1107–1122.

Chen, Z., Govindaraju, R. S., and Kavvas, M. L. (1994a). Spatial averaging of unsaturated flow equations under infiltration conditions over areally heterogeneous fields: 1. Development of models. *Water Resources Research*, 30(2):523–533.

Chen, Z., Govindaraju, R. S., and Kavvas, M. L. (1994b). Spatial averaging of unsaturated flow equations under infiltration conditions over areally heterogeneous fields: 2. Numerical simulations. *Water Resources Research*, 30(2):535–548.

Ching, J. and Phoon, K.-K. (2013). Multivariate distribution for undrained shear strengths under various test procedures. *Canadian Geotechnical Journal*, 50(9):907–923.

Ching, J. and Phoon, K.-K. (2014). Correlations among some clay parameters—the multivariate distribution. *Canadian Geotechnical Journal*, 51(6):686–704.

Cho, S. E. (2007). Effects of spatial variability of soil properties on slope stability. *Engineering Geology*, 92(3):97–109.

Cho, S. E. (2012). Probabilistic analysis of seepage that considers the spatial variability of permeability for an embankment on soil foundation. *Engineering Geology*, 133:30–39.

Cho, S. E. and Park, H. C. (2010). Effect of spatial variability of cross-correlated soil properties on bearing capacity of strip footing. *International Journal for Numerical and Analytical Methods in Geomechanics*, 34(1):1–26.

Cividini, A., Maier, G., and Nappi, A. (1983). Parameter estimation of a static geotechnical model using a Bayes' approach. *International Journal of Rock Mechanics and Mining Sciences & Geomechanics Abstracts*, 20(5):215–226.

Conte, E., Silvestri, F., and Troncone, A. (2010). Stability analysis of slopes in soils with strain-softening behaviour. *Computers and Geotechnics*, 37(5):710–722.

Cooley, J. W. and Tukey, J. W. (1965). An algorithm for the machine calculation of complex Fourier series. *Mathematics of Computation*, 19(90):297–301.

Cornell, C. A. (1969). Structural safety specifications based on second-moment reliability analysis. In *IABSE Symposium on Concepts of Safety of Structures and Methods of Design, London*, pages 235–245.

Cornell, C. A. (1970). A first-order reliability theory for structural design. In *Structural Reliability and Codified Design, SM Study No. 3, University of Waterloo, Waterloo, Ontario, Canada*.

Cornell, C. A. (1972). First-order uncertainty analysis of soil deformation and stability. In *Proceedings of First International Conference on Applications of Probability and Statistics in Soil and Structural Engineering (ICAPI), Hong Kong*, pages 129–144.

Dai, T. S. and Sparling, J. H. (1973). Measurement of hydraulic conductivity of peats. *Canadian Journal of Soil Science*, 53(1):21–26.

De Rooij, G. H., Kasteel, R. T., Papritz, A., and Flühler, H. (2004). Joint distributions of the unsaturated soil hydraulic parameters and their effect on other variates. *Vadose Zone Journal*, 3(3):947–955.

Dee, D. P. and Da Silva, A. M. (1998). Data assimilation in the presence of forecast bias. *Quarterly Journal of the Royal Meteorological Society*, 124(545):269–295.

DeGroot, D. J. and Baecher, G. B. (1993). Estimating autocovariance of in-situ soil properties. *Journal of Geotechnical Engineering*, 119(1):147–166.

Deng, Y.-F., Tang, A.-M., Cui, Y.-J., and Li, X.-L. (2011). Study on the hydraulic conductivity of Boom Clay. *Canadian Geotechnical Journal*, 48(10):1461–1470.

Duncan, J. M. (2000). Factors of safety and reliability in geotechnical engineering. *Journal of Geotechnical and Geoenvironmental Engineering*, 126(4):307–316.

Ebel, B. A., Loague, K., and Borja, R. I. (2010). The impacts of hysteresis on variably saturated hydrologic response and slope failure. *Environmental Earth Sciences*, 61(6):1215–1225.

El-Ramly, H., Morgenstern, N. R., and Cruden, D. M. (2003). Probabilistic stability analysis of a tailings dyke on presheared clay shale. *Canadian Geotechnical Journal*, 40(1):192–208.

El-Ramly, H., Morgenstern, N. R., and Cruden, D. M. (2006). Lodalen slide: a probabilistic assessment. *Canadian Geotechnical Journal*, 43(9):956–968.

Evensen, G. (1994). Sequential data assimilation with a nonlinear quasi-geostrophic model using Monte Carlo methods to forecast error statistics. *Journal of Geophysical Research: Oceans*, 99(5):10143–10162.

Evensen, G. (2003). The ensemble Kalman filter: Theoretical formulation and practical implementation. *Ocean dynamics*, 53(4):343–367.

Evensen, G. (2009). *Data assimilation: the ensemble Kalman filter*. New York: Springer.

Fenton, G. A. (1994). Error evaluation of three random-field generators. *Journal of engineering mechanics*, 120(12):2478–2497.

Fenton, G. A. and Griffiths, D. V. (1996). Statistics of free surface flow through stochastic earth dam. *Journal of Geotechnical Engineering*, 122(6):427–436.

Fenton, G. A. and Griffiths, D. V. (1997). Extreme hydraulic gradient statistics in stochastic earth dam. *Journal of Geotechnical and Geoenvironmental Engineering*, 123(11):995–1000.

Fenton, G. A. and Griffiths, D. V. (2003). Bearing-capacity prediction of spatially random c - φ soils. *Canadian Geotechnical Journal*, 40(1):54–65.

Fenton, G. A. and Griffiths, D. V. (2008). *Risk assessment in geotechnical engineering*. New York:Wiley.

Fenton, G. A. and Vanmarcke, E. H. (1990). Simulation of random fields via local average subdivision. *Journal of Engineering Mechanics*, 116(8):1733–1749.

Firouzianbandpey, S., Griffiths, D. V., Ibsen, L. B., and Andersen, L. V. (2014). Spatial correlation length of normalized cone data in sand: case study in the north of Denmark. *Canadian Geotechnical Journal*, 51(8):844–857.

Foster, M., Fell, R., and Spannagle, M. (2000). A method for assessing the relative likelihood of failure of embankment dams by piping. *Canadian Geotechnical Journal*, 37(5):1025–1061.

Fredlund, D. G. and Krahn, J. (1977). Comparison of slope stability methods of analysis. *Canadian Geotechnical Journal*, 14(3):429–439.

Fredlund, D. G. and Xing, A. (1994). Equations for the soil-water characteristic curve. *Canadian Geotechnical Journal*, 31(4):521–532.

Freeze, R. A. (1975). A stochastic-conceptual analysis of one-dimensional groundwater flow in nonuniform homogeneous media. *Water Resources Research*, 11(5):725–741.

Gardner, R. H., O'Neill, R. V., Mankin, J. B., and Carney, J. H. (1981). A comparison of sensitivity analysis and error analysis based on a stream ecosystem model. *Ecological Modelling*, 12(3):173–190.

Gelhar, L. W. (1976). Effects of hydraulic conductivity variations on groundwater flows. In *Proceedings of the 2nd International Symposium on Stochastic Hydraulics, International Association for Hydraulic Research, Lund, Sweden*, pages 409–428.

Gens, A., Ledesma, A., and Alonso, E. E. (1996). Estimation of parameters in geotechnical backanalysis—II. Application to a tunnel excavation problem. *Computers and Geotechnics*, 18(1):29–46.

Gersch, W. and Yonemoto, J. (1977). Synthesis of multivariate random vibration systems: a two-stage least squares AR-MA model approach. *Journal of Sound and Vibration*, 52(4):553–565.

Gilbert, R. B., Wright, S. G., and Liedtke, E. (1998). Uncertainty in back analysis of slopes: Kettleman hills case history. *Journal of Geotechnical and Geoenvironmental Engineering*, 124(12):1167–1176.

Gioda, G. and Sakurai, S. (1987). Back analysis procedures for the interpretation of field measurements in geomechanics. *International Journal for Numerical and Analytical Methods in Geomechanics*, 11(6):555–583.

Griffiths, D. V. and Fenton, G. A. (1993). Seepage beneath water retaining structures founded on spatially random soil. *Géotechnique*, 43(4):577–87.

Griffiths, D. V. and Fenton, G. A. (1997). Three-dimensional seepage through spatially random soil. *Journal of Geotechnical and Geoenvironmental Engineering*, 123(2):153–160.

Griffiths, D. V. and Fenton, G. A. (2004). Probabilistic slope stability analysis by finite elements. *Journal of Geotechnical and Geoenvironmental Engineering*, 130(5):507–518.

Griffiths, D. V. and Fenton, G. A. (2007). *Probabilistic methods in geotechnical engineering*. New York: Springer Wien.

Griffiths, D. V., Huang, J., and Fenton, G. A. (2009). Influence of spatial variability on slope reliability using 2-D random fields. *Journal of Geotechnical and Geoenvironmental Engineering*, 135(10):1367–1378.

Griffiths, D. V. and Lane, P. A. (1999). Slope stability analysis by finite elements. *Géotechnique*, 49(3):387–403.

Gui, S., Zhang, R., Turner, J. P., and Xue, X. (2000). Probabilistic slope stability analysis with stochastic soil hydraulic conductivity. *Journal of Geotechnical and Geoenvironmental Engineering*, 126(1):1–9.

Gupta, N., Rudra, R. P., and Parkin, G. (2006). Analysis of spatial variability of hydraulic conductivity at field scale. *Canadian Biosystems Engineering*, 48:1.55–1.62.

Han, X.-W., Shao, M.-A., and Horton, R. (2010). Estimating van Genuchten model parameters of undisturbed soils using an integral method. *Pedosphere*, 20(1):55–62.

Hasofer, A. M. and Lind, N. C. (1974). An exact and invariant first-order reliability format. *Journal of the Engineering Mechanics Division*, 100(1):111–121.

Hicks, M. A., Nuttall, J. D., and Chen, J. (2014). Influence of heterogeneity on 3D slope reliability and failure consequence. *Computers and Geotechnics*, 61:198–208.

Hicks, M. A., Nuttall, J. D., and Spencer, W. A. (2007). Stochastic and finite element modelling of 3D heterogeneity in geo-engineering. In *Proceedings of ECCOMAS Thematic Conf Heterogeneous Materials with Applications in Construction and Biomedical Engineering, Prague*, pages 236–7.

Hicks, M. A. and Onisiphorou, C. (2005). Stochastic evaluation of static liquefaction in a predominantly dilative sand fill. *Géotechnique*, 55(2):123–133.

Hicks, M. A. and Samy, K. (2002a). Influence of anisotropic spatial variability on slope reliability. In *Proceedings of the 8th International Symposium Numerical Models Geomech. Rome, Italy*, pages 535–539.

Hicks, M. A. and Samy, K. (2002b). Influence of heterogeneity on undrained clay slope stability. *Quarterly Journal of Engineering Geology and Hydrogeology*, 35(1):41–49.

Hicks, M. A. and Samy, K. (2004). Stochastic evaluation of heterogeneous slope stability. *Italian Geotechnical Journal*, 38(2):54–66.

Hicks, M. A. and Spencer, W. A. (2008). 3D finite element modelling of slope reliability. *Proceedings of 8th WCCM and 5th ECCOMAS, Venice*.

Hicks, M. A. and Spencer, W. A. (2010). Influence of heterogeneity on the reliability and failure of a long 3d slope. *Computers and Geotechnics*, 37(7):948–955.

Holtz, R. D. and Krizek, R. J. (1971). Effects of stress path and over-consolidation ratio on the shear strength of a kaolin clay. In *Proceedings of Fifth Regional Conference for Africa on Soil Mechanics and Foundation Engineering, Luanda, Angola*, pages 17–25.

Hommels, A. and Molenkamp, F. (2006). Inverse analysis of an embankment using the ensemble Kalman filter including heterogeneity of the soft soil. *Sixth European Conference on Numerical Methods in Geotechnical Engineering, Graz*, pages 635–639.

Hommels, A., Molenkamp, F., Heemink, A. W., and Nguyen, B. L. (2001). Effectiveness of inverse modelling techniques applied in geomechanics. Technical report, Delft Cluster Pub.

Hommels, A., Molenkamp, F., Heemink, A. W., and Nguyen, B. L. (2005). Inverse analysis of an embankment on soft clay using the ensemble Kalman filter. In *Proceedings of the 10th International Conference on Civil, Structural and Environmental Engineering Computing, Stirling, Scotland*, pages 1–15.

Honjo, Y., Wen-Tsung, L., and Guha, S. (1994). Inverse analysis of an embankment on soft clay by extended Bayesian method. *International Journal for Numerical and Analytical Methods in Geomechanics*, 18(10):709–734.

Huang, W.-C., Weng, M.-C., and Chen, R.-K. (2014). Levee failure mechanisms during the extreme rainfall event: a case study in Southern Taiwan. *Natural Hazards*, 70(2):1287–1307.

Huat, B. B. K., Kazemian, S., Prasad, A., and Barghchi, M. (2011). State of an art review of peat: General perspective. *International Journal of Physical Sciences*, 6(8):1988–1996.

Jafarpour, B. and Tarrahi, M. (2011). Assessing the performance of the ensemble Kalman filter for subsurface flow data integration under variogram uncertainty. *Water Resources Research*, 47(5):W05537.

Jaynes, D. (1984). Comparison of soil-water hysteresis models. *Journal of Hydrology*, 75(1-4):287–299.

Kalman, R. E. (1960). A new approach to linear filtering and prediction problems. *Journal of Basic Engineering*, 82(1):35–45.

Kanning, W. (2012). *The weakest link: spatial variability in the piping failure mechanism of dikes*. PhD thesis, Delft University of Technology.

Krymskaya, M. V., Hanea, R. G., and Verlaan, M. (2009). An iterative ensemble Kalman filter for reservoir engineering applications. *Computational Geosciences*, 13(2):235–244.

Lam, L., Fredlund, D. G., and Barbour, S. L. (1987). Transient seepage model for saturated-unsaturated soil systems: a geotechnical engineering approach. *Canadian Geotechnical Journal*, 24(4):565–580.

Lane, E. W. (1935). Security from under-seepage-masonry dams on earth foundations. *Transactions of the American Society of Civil Engineers*, 100(1):1235–1272.

Le, T. M. H., Gallipoli, D., Sánchez, M., and Wheeler, S. (2015). Stability and failure mass of unsaturated heterogeneous slopes. *Canadian Geotechnical Journal*, 52(11):1747–1761.

Le, T. M. H., Gallipoli, D., Sánchez, M., and Wheeler, S. J. (2012). Stochastic analysis of unsaturated seepage through randomly heterogeneous earth embankments. *International Journal for Numerical and Analytical Methods in Geomechanics*, 36(8):1056–1076.

Ledesma, A., Gens, A., and Alonso, E. E. (1996a). Estimation of parameters in geotechnical backanalysis—I. Maximum likelihood approach. *Computers and Geotechnics*, 18(1):1–27.

Ledesma, A., Gens, A., and Alonso, E. E. (1996b). Parameter and variance estimation in geotechnical backanalysis using prior information. *International Journal for Numerical and Analytical Methods in Geomechanics*, 20(2):119–141.

Lee, I.-M. and Kim, D.-H. (1999). Parameter estimation using extended Bayesian method in tunnelling. *Computers and Geotechnics*, 24(2):109–124.

Lehmann, F. and Ackerer, P. H. (1998). Comparison of iterative methods for improved solutions of the fluid flow equation in partially saturated porous media. *Transport in Porous Media*, 31(3):275–292.

Li, Y., Hicks, M. A., and Nuttall, J. D. (2015a). Comparative analyses of slope reliability in 3d. *Engineering Geology*, 196:12–23.

Li, Y., Hicks, M. A., and Vardon, P. J. (2015b). Three dimensional discrete failures in long heterogeneous slopes. In *Proceedings of 5th International Symposium on Geotechnical Safety and Risk, Rotterdam*, pages 666–670.

Liu, K., Hicks, M. A., Vardon, P. J., and Jommi, C. (2015a). Probabilistic analysis of velocity distribution under earth embankments for piping investigation. In *Proceedings of 5th International Symposium on Geotechnical Safety and Risk, Rotterdam*, pages 683–688.

Liu, K., Vardon, P. J., Arnold, P., and Hicks, M. A. (2015b). Effect of hysteresis on the stability of an embankment under transient seepage. *IOP Conference Series: Earth and Environmental Science*, 26(1):012013.

Liu, K., Vardon, P. J., Hicks, M. A., and Arnold, P. (2017). Combined effect of hysteresis and heterogeneity on the stability of an embankment under transient seepage. *Engineering Geology*, 219:140–150.

Lloret-Cabot, M., Fenton, G. A., and Hicks, M. A. (2014). On the estimation of scale of fluctuation in geostatistics. *Georisk: Assessment and Management of Risk for Engineered Systems and Geohazards*, 8(2):129–140.

Lloret-Cabot, M., Hicks, M. A., and van den Eijnden, A. P. (2012). Investigation of the reduction in uncertainty due to soil variability when conditioning a random field using kriging. *Géotechnique Letters*, 2:123–127.

Lumb, P. (1966). The variability of natural soils. *Canadian Geotechnical Journal*, 3(2):74–97.

Ma, K.-C., Tan, Y.-C., and Chen, C.-H. (2011). The influence of water retention curve hysteresis on the stability of unsaturated soil slopes. *Hydrological Processes*, 25(23):3563–3574.

Madsen, H. O. (1985). First order vs. second order reliability analysis of series structures. *Structural Safety*, 2(3):207–214.

Matheron, G. (1973). The intrinsic random functions and their applications. *Advances in Applied Probability*, 5(3):439–468.

Matsui, T. and San, K.-C. (1992). Finite element slope stability analysis by shear strength reduction technique. *Soils and Foundations*, 32(1):59–70.

McMillan, W. D. (1966). *Theoretical analysis of groundwater basin operations*. Hydraulic Laboratory, University of California.

Mesri, G., Stark, T. D., Ajlouni, M. A., and Chen, C. S. (1997). Secondary compression of peat with or without surcharging. *Journal of Geotechnical and Geoenvironmental Engineering*, 123(5):411–421.

Mualem, Y. (1976). A new model for predicting the hydraulic conductivity of unsaturated porous media. *Water Resources Research*, 12(3):513–522.

Nakagawa, K., Saito, M., and Berndtsson, R. (2012). On the importance of hysteresis and heterogeneity in the numerical simulation of unsaturated flow. *Hydrological Research Letters*, 6(0):59–64.

Nguyen, V. U. and Chowdhury, R. N. (1985). Simulation for risk analysis with correlated variables. *Géotechnique*, 35(1):47–58.

Nielsen, D. R., Biggar, J. W., and Erh, K. T. (1973). Spatial variability of field-measured soil-water properties. *Hilgardia*, 42:215–259.

Papaioannou, I. and Straub, D. (2012). Reliability updating in geotechnical engineering including spatial variability of soil. *Computers and Geotechnics*, 42:44–51.

Pasetto, D., Niu, G.-Y., Pangle, L., Paniconi, C., Putti, M., and Troch, P. A. (2015). Impact of sensor failure on the observability of flow dynamics at the biosphere 2 leo hillslopes. *Advances in Water Resources*, 86:327–339.

Pham, H. Q., Fredlund, D. G., and Barbour, S. L. (2005). A study of hysteresis models for soil-water characteristic curves. *Canadian Geotechnical Journal*, 42(6):1548–1568.

Phoon, K.-K. and Ching, J. (2014). *Risk and reliability in geotechnical engineering*. CRC Press.

Phoon, K.-K. and Kulhawy, F. H. (1999). Characterization of geotechnical variability. *Canadian Geotechnical Journal*, 36(4):612–624.

Phoon, K.-K., Santoso, A., and Quek, S.-T. (2010). Probabilistic analysis of soil-water characteristic curves. *Journal of Geotechnical and Geoenvironmental Engineering*, 136(3):445–455.

Polemio, M. and Lollino, P. (2011). Failure of infrastructure embankments induced by flooding and seepage: a neglected source of hazard. *Natural Hazards and Earth System Sciences*, 11(12):3383–3396.

Rackwitz, R. (2000). Reviewing probabilistic soils modelling. *Computers and Geotechnics*, 26(3):199–223.

Rahardjo, H., Nio, A. S., Leong, E. C., and Song, N. Y. (2010). Effects of groundwater table position and soil properties on stability of slope during rainfall. *Journal of Geotechnical and Geoenvironmental Engineering*, 136(11):1555–1564.

Rahardjo, H., Ong, T., Rezaur, R., and Leong, E. C. (2007). Factors controlling instability of homogeneous soil slopes under rainfall. *Journal of Geotechnical and Geoenvironmental Engineering*, 133(12):1532–1543.

Rayne, T. W., Bradbury, K. R., and Mickelson, D. M. (1996). *Variability of hydraulic conductivity in uniform sandy till, Dane County, Wisconsin*, volume 74. Wisconsin Geological and Natural History Survey.

Revelli, R. and Ridolfi, L. (2000). Influence of heterogeneity on the flow in unconfined aquifers. *Journal of Hydrology*, 228(1):150–159.

Richards, K. S. and Reddy, K. R. (2012). Experimental investigation of initiation of backward erosion piping in soils. *Géotechnique*, 62(10):933–942.

Richards, K. S. and Reddy, K. R. (2014). Kinetic energy method for predicting initiation of backward erosion in earthen dams and levees. *Environmental and Engineering Geoscience*, 20(1):85–97.

Robertson, P. K. (2010). Estimating in-situ soil permeability from CPT and CPTu. In *Proceedings of 2nd International Symposium on Cone Penetration Testing, California State Polytechnic University Pomona, CA*, pages 535–542.

Rosenblueth, E. (1975). Point estimates for probability moments. *Proceedings of the National Academy of Sciences*, 72(10):3812–3814.

Rosenblueth, E. (1981). Two-point estimates in probabilities. *Applied Mathematical Modelling*, 5(5):329–335.

Russo, D. and Bouton, M. (1992). Statistical analysis of spatial variability in unsaturated flow parameters. *Water Resources Research*, 28(7):1911–1925.

Santoso, A. M., Phoon, K.-K., and Quek, S.-T. (2011). Effects of soil spatial variability on rainfall-induced landslides. *Computers and Structures*, 89(11):893–900.

Schlotzhauer, S. M. and Price, J. S. (1999). Soil water flow dynamics in a managed cutover peat field, quebec: Field and laboratory investigations. *Water Resources Research*, 35(12):3675–3683.

Sellmeijer, J. B. (2006). Numerical computation of seepage erosion below dams (piping). In *Proceedings of 3rd International Conference on Scour and Erosion, Amsterdam*, pages 596–601.

Sellmeijer, J. B. and Koenders, M. A. (1991). A mathematical model for piping. *Applied Mathematical Modelling*, 15(11-12):646–651.

Serre, D., Peyras, L., Tourment, R., and Diab, Y. (2008). Levee performance assessment methods integrated in a GIS to support planning maintenance actions. *Journal of Infrastructure Systems*, 14(3):201–213.

Sivakumar Babu, G. L. and Murthy, D. S. (2005). Reliability analysis of unsaturated soil slopes. *Journal of Geotechnical and Geoenvironmental Engineering*, 131(11):1423–1428.

Sivakumar Babu, G. L. and Vasudevan, A. K. (2008). Seepage velocity and piping resistance of coir fiber mixed soils. *Journal of Irrigation and Drainage Engineering*, 134(4):485–492.

Smith, I. M., Griffiths, D. V., and Margetts, L. (2013). *Programming the finite element method*. New York: John Wiley & Sons.

Smith, L. and Freeze, R. A. (1979a). Stochastic analysis of steady state groundwater flow in a bounded domain: 1. One-dimensional simulations. *Water Resources Research*, 15(3):521–528.

Smith, L. and Freeze, R. A. (1979b). Stochastic analysis of steady state groundwater flow in a bounded domain: 2. Two-dimensional simulations. *Water Resources Research*, 15(6):1543–1559.

Springer, E. P. and Cundy, T. W. (1987). Field-scale evaluation of infiltration parameters from soil texture for hydrologic analysis. *Water Resources Research*, 23(2):325–334.

Srivastava, A., Sivakumar Babu, G. L., and Haldar, S. (2010). Influence of spatial variability of permeability property on steady state seepage flow and slope stability analysis. *Engineering Geology*, 110(3):93–101.

Suchomel, R. and Mašın, D. (2010). Comparison of different probabilistic methods for predicting stability of a slope in spatially variable c–φ soil. *Computers and Geotechnics*, 37(1):132–140.

Tami, D., Rahardjo, H., and Leong, E.-C. (2004). Effects of hysteresis on steady-state infiltration in unsaturated slopes. *Journal of Geotechnical and Geoenvironmental Engineering*, 130(9):956–967.

Tang, D. H. and Pinder, G. F. (1977). Simulation of groundwater flow and mass transport under uncertainty. *Advances in Water Resources*, 1(1):25–30.

Tang, W. H., Yucemen, M. S., and Ang, A. H.-S. (1976). Probability-based short term design of soil slopes. *Canadian Geotechnical Journal*, 13(3):201–215.

Terzaghi, K. V. (1922). Der grundbruch an stauwerken und seine verhuetung. *Die Wasserkraft*, 17(24):445–449.

Thevanayagam, S. (1998). Effect of fines and confining stress on undrained shear strength of silty sands. *Journal of Geotechnical and Geoenvironmental Engineering*, 124(6):479–491.

Tsai, T.-L. and Chen, H.-F. (2010). Effects of degree of saturation on shallow landslides triggered by rainfall. *Environmental Earth Sciences*, 59(6):1285–1295.

Tsaparas, I., Rahardjo, H., Toll, D. G., and Leong, E. C. (2002). Controlling parameters for rainfall-induced landslides. *Computers and Geotechnics*, 29(1):1–27.

Tschuchnigg, F., Schweiger, H. F., and Sloan, S. W. (2015). Slope stability analysis by means of finite element limit analysis and finite element strength reduction techniques. Part I: Numerical studies considering non-associated plasticity. *Computers and Geotechnics*, 70:169–177.

Vallejo, L. E. and Mawby, R. (2000). Porosity influence on the shear strength of granular material–clay mixtures. *Engineering Geology*, 58(2):125–136.

Van Baars, S. (2005). The horizontal failure mechanism of the Wilnis peat dyke. *Géotechnique*, 55(4):319–323.

Van Beek, V. M., Bezuijen, A., Sellmeijer, J. B., and Barends, F. B. J. (2014). Initiation of backward erosion piping in uniform sands. *Géotechnique*, 64(12):927–941.

van Genuchten, M. T. (1980). A closed-form equation for predicting the hydraulic conductivity of unsaturated soils. *Soil Science Society of America Journal*, 44(5):892–898.

Vanapalli, S., Fredlund, D., Pufahl, D., and Clifton, A. (1996). Model for the prediction of shear strength with respect to soil suction. *Canadian Geotechnical Journal*, 33(3):379–392.

Vanmarcke, E. H. (1977). Reliability of earth slopes. *Journal of the Soil Mechanics and Foundations Division*, 103(11):1247–1265.

Vardanega, P. J. and Haigh, S. K. (2014). The undrained strength–liquidity index relationship. *Canadian Geotechnical Journal*, 51(9):1073–1086.

Vardon, P. J., Liu, K., and Hicks, M. A. (2016). Reduction of slope stability uncertainty based on hydraulic measurement via inverse analysis. *Georisk: Assessment and Management of Risk for Engineered Systems and Geohazards*, 10(3):223–240.

Verruijt, A. (2012). *Soil mechanics*. The Netherlands. http://geotech.fce.vutbr.cz/studium/mech_zemin/soil_mechanics.pdf.

Wang, L., Hwang, J. H., Luo, Z., Juang, C. H., and Xiao, J. (2013). Probabilistic back analysis of slope failure–a case study in Taiwan. *Computers and Geotechnics*, 51:12–23.

Wang, L., Luo, Z., Xiao, J., and Juang, C. H. (2014). Probabilistic inverse analysis of excavation-induced wall and ground responses for assessing damage potential of adjacent buildings. *Geotechnical and Geological Engineering*, 32(2):273–285.

Warren, J. and Price, H. (1961). Flow in heterogeneous porous media. *Society of Petroleum Engineers Journal*, 1(03):153–169.

Wells, T., Fityus, S., Smith, D. W., and Moe, H. (2006). The indirect estimation of saturated hydraulic conductivity of soils, using measurements of gas permeability. i. laboratory testing with dry granular soils. *Soil Research*, 44(7):719–725.

Wu, L., Huang, R., and Xu, Q. (2012). Incorporating hysteresis in one-dimensional seepage modeling in unsaturated soils. *KSCE Journal of Civil Engineering*, 16(1):69–77.

Wu, T. H. and Kraft, L. M. (1970). Safety analysis of slopes. *Journal of Soil Mechanics and Foundations Div ASCE*, 96:609–630.

Xu, T., Gómez-Hernández, J. J., Li, L., and Zhou, H. (2013). Parallelized ensemble Kalman filter for hydraulic conductivity characterization. *Computers and Geosciences*, 52:42–49.

Yang, C., Sheng, D., and Carter, J. P. (2011a). Hysteretic seepage analysis in unsaturated soil covers. In *Proceedings of the 5th Asia–Pacific Conference on Unsaturated Soils, Pattaya, Thailand*, pages 541–546.

Yang, C., Sheng, D., and Carter, J. P. (2012a). Effect of hydraulic hysteresis on seepage analysis for unsaturated soils. *Computers and Geotechnics*, 41:36–56.

Yang, C., Sheng, D., Carter, J. P., and Huang, J. (2012b). Stochastic evaluation of hydraulic hysteresis in unsaturated soils. *Journal of Geotechnical and Geoenvironmental Engineering*, 139(7):1211–1214.

Yang, C. X., Wu, Y. H., Hon, T., and Feng, X.-T. (2011b). Application of extended Kalman filter to back analysis of the natural stress state accounting for measuring uncertainties. *International Journal for Numerical and Analytical Methods in Geomechanics*, 35(6):694–712.

Zhang, L. L. (2007). Effects of soil hydraulic hysteresis on slope reliability. In *First International Symposium on Geotechnical Safety and Risk, Shanghai*, pages 399–405.

Zhang, L. L., Fredlund, M. D., Fredlund, D. G., Lu, H., and Wilson, G. W. (2015). The influence of the unsaturated soil zone on 2-d and 3-d slope stability analyses. *Engineering Geology*, 193:374–383.

Zhang, L. L., Li, J. H., Li, X., Zhang, J., and Zhu, H. (2016). *Rainfall-Induced Soil Slope Failure Stability Analysis and Probabilistic Assessment*. CRC Press.

Zhang, L. L., Zhang, J., Zhang, L. M., and Tang, W. H. (2010). Back analysis of slope failure with Markov chain monte carlo simulation. *Computers and Geotechnics*, 37(7):905–912.

Zhang, L. L., Zhang, L. M., and Tang, W. H. (2005). Rainfall-induced slope failure considering variability of soil properties. *Géotechnique*, 55(2):183–188.

Zhang, L. L., Zheng, Y. F., Zhang, L. M., Li, X., and Wang, J. H. (2014). Probabilistic model calibration for soil slope under rainfall: effects of measurement duration and frequency in field monitoring. *Géotechnique*, 64(5):365–378.

Zhang, L. L., Zuo, Z. B., Ye, G. L., Jeng, D. S., and Wang, J. H. (2013). Probabilistic parameter estimation and predictive uncertainty based on field measurements for unsaturated soil slope. *Computers and Geotechnics*, 48:72–81.

Zheng, D., Leung, J., and Lee, B. (2010). An ensemble Kalman filter for atmospheric data assimilation: Application to wind tunnel data. *Atmospheric Environment*, 44(13):1699–1705.

Zhou, H., Gómez-Hernández, J. J., and Li, L. (2014). Inverse methods in hydrogeology: Evolution and recent trends. *Advances in Water Resources*, 63:22–37.

Zhou, M., Li, Y., Xiang, Z., Swoboda, G., and Cen, Z. (2007). A modified extended Bayesian method for parameter estimation. *Tsinghua Science and Technology*, 12(5):546–553.

Zhu, H., Zhang, L. M., Zhang, L. L., and Zhou, C. B. (2013). Two-dimensional probabilistic infiltration analysis with a spatially varying permeability function. *Computers and Geotechnics*, 48:249–259.

Summary

Embankments, dikes and dams are common structures in geotechnical engineering, with considerable societal value. In these structures, slow water flow, i.e. seepage, often occurs. Therefore, the stability of such slopes under seepage is of great concern to engineers, because of the potential consequences of failure. In order to predict slope stability, a single factor of safety is often calculated, but this approach is unable to represent the actual condition of slopes because it ignores the spatial variability and uncertainty of soil properties. More recently, probabilistic methods, which can account for the uncertainty of soil parameters, have been developed and widely used. In probabilistic analysis, the input values, e.g. the distribution of soil parameter values, are needed. However, these are generally only a global description of the site, whereas the local spatial variability often cannot be well measured. To improve the estimation of the local variability of soil parameters, inverse analysis employing observed data has been applied in this thesis. In addition, a more accurate description of the hydraulic behaviour of unsaturated soils has been used to better simulate the flow in these structures.

The main purpose of this thesis is to more reliably predict slope stability under seepage. A framework which links stochastic analysis, i.e. the random finite element method, with the ensemble Kalman filter has been proposed. By using this approach, hydraulic measurements have been used to reduce the uncertainty in the estimation of hydraulic parameters, and thereby improve the estimation of pore water pressures and slope stability. The approach has been applied to both steady-state and transient seepage analyses. In both cases, the estimation of the local variability of hydraulic conductivity has been significantly improved and the uncertainty reduced. Moreover, in the transient seepage analysis, the improvement in the estimation of hydraulic conductivity using temporal measurements is better than that in the steady-state seepage analysis via static measurements. However, care must be taken when selecting initial parameters and parameter distributions.

In this thesis, a more realistic model of the hydraulic behaviour of unsaturated soils has been used in simulating the transient drying-wetting process, where the hysteretic water retention behaviour of unsaturated soil has been considered. The combined effect of the hysteresis and spatial variability of unsaturated soils has been investigated. It is found that, by ignoring this hysteresis, the slope stability may be overestimated.

In the final part of the thesis, the research has been extended to investigate the influence of soil heterogeneity on the internal stability of an embankment, i.e. on the potential for piping initiation and development. The stochastic seepage analysis showed that heterogeneity of the hydraulic conductivity increases the possibility of piping initiation. The locations of high local velocity are significantly affected by the spatial variability of soils.

Samenvatting

Taluds, dijken en dammen zijn veelvoorkomende geotechnische werken met vaak een aanzienlijke maatschappelijke waarde. In deze werken vindt vaak trage grondwaterstroming plaats. Het is voor ingenieurs daarom van groot belang de stabiliteit van dergelijke hellingen onder invloed van grondwaterstroming te onderzoeken, vanwege de mogelijke gevolgen voor bezwijken. Om hellingstabiliteit te voorspellen wordt vaak een enkele veiligheidsfactor berekend, maar deze aanpak is niet geschikt om de werkelijke toestand van een helling te beschrijven omdat de ruimtelijke variabiliteit en onzekerheid van bodemeigenschappen genegeerd worden. Recentelijk zijn probabilistische methoden ontwikkeld die onzekerheden in grondparameters in rekening kunnen brengen. Deze methoden worden op grote schaal gebruikt. Deze probabilistische analyses vragen om invoerwaarden, zoals de statistische verdeling van de waarde voor een grondparameter. Deze invoerwaarden zijn meestal slechts een globale beschrijving van het terrein en lokale ruimtelijke variabiliteit blijkt vaak niet goed meetbaar. Om de schatting van de lokale variabiliteit van bodemparameters te verbeteren wordt in dit onderzoek inverse analyse toegepast, waarin observatiedata wordt gebruikt. Daarnaast is een meer nauwkeurige beschrijving van het hydraulisch gedrag van onverzadigde grond gebruikt om de grondwaterstroming beter te simuleren.

Het hoofddoel van dit proefschrift is met grotere zekerheid de stabiliteit van hellingen onder invloed van grondwaterstroming te voorspellen. Hiervoor is een methode voorgesteld die stochastische analyse (de random finite elelemnt method) combineert met de ensemble Kalman filter. Door deze aanpak kunnen hydraulische metingen gebruikt worden om de onzekerheid in de schatting van hydraulische parameters te verminderen, waardoorde schattingen van grondwaterspanning en hellingstabiliteit verbeterd worden. De aanpak is toegepast op zowel stationaire als transiënte stromingsanalyses. In beide gevallen is de schatting van de lokale variatie van doorlatendheid aanzienlijk verbeterd en de onzekerheid gereduceerd. Bovendien is de verbetering van de schatting van doorlatendheid groter wanneer tijds-afhankelijke waarnemingsdata wordt gebruikt in transiënte analyses dan wanneer statische data wordt gebruikt in stationaire analyses. Echter initiële paramters en parameterdistributies dienen met zorg te zijn gekozen.

In dit onderzoek is een realistischer model van het hydraulische gedrag van onverzadigde grond toegepast voor het simuleren van het transiënte proces van verandering inverzadiging van de grond. Het hysteresegedrag van onverzadigde grond is hierin meegenomen. Het gecombineerde effect van de hysterese en de ruimtelijke spreiding van onverzadigde grond is onderzocht. Gebleken is dat door het negeren van deze hysterese de stabiliteit van de helling overschat kan worden.

In het laatste deel van dit proefschrift gaat in op de invloed van bodemheterogeniteit op de inwendige stabiliteit van een dijk, d.w.z. de mogelijke initiatie-en

ontwikkeling van piping. De stochastische hydrologische analyse toont aan dat met de heterogeniteit van de doorlatendheid de mogelijkheid tot initiatie van piping toeneemt. De locaties van hoge lokale stroomsnelheden worden aanzienlijk beïnvloed door de ruimtelijke variatie van de bodem.

Notation

Acronyms

CDF	cumulative distribution function
EKF	extended Kalman filter
EnKF	ensemble Kalman filter
FEM	finite element method
FORM	first order reliability method
FOS	factor of safety
KF	Kalman filter
LAS	local average subdivision
LEM	limit equilibrium method
MCM	Monte Carlo method
PDF	probability density function
PEM	point estimate method
PWP	pore water pressure
RFEM	random finite element method
RMSE	root mean square error
SOF	scale of fluctuation
SPREAD	uncertainty of the ensemble members
SRM	strength reduction method
SWRC	soil water retention curve
VGM	van Genuchten–Mualem model
VWC	volumetric water content

Greek Symbols

α	approximately inverse of the air entry suction head in the SWRC
α_d	approximately the inverse of the air-entry suction head in the drying SWRC
α_w	approximately the inverse of the air-entry suction head for main wetting curve
β	reliability index
χ	scalar defining the suction-induced effective stress
γ	unit weight of soil
γ_w	unit weight of water
κ	slope of the scanning curve
$\boldsymbol{\epsilon}_i$	a vector of measurement errors
$\boldsymbol{\epsilon}_{initial}$	initial errors in hydraulic head
$\boldsymbol{\epsilon}_{updated}$	updated errors in hydraulic head
$\boldsymbol{\rho}$	correlation matrix
$\boldsymbol{\sigma}'$	effective stress vector
μ	mean
μ_F	mean of the performance function
μ_k	mean of the hydraulic conductivity
$\mu_{v_{max}}$	mean of the maximum local velocity
ν	Poisson's ratio
ϕ'	effective friction angle
ϕ_f'	factored effective friction angle at slope failure
ρ	spatial correlation between variable values at different locations
ρ_s	density of soil solids
ρ_w	density of water
$\rho_{\ln k,\phi}$	correlation coefficient between $\ln k$ and friction angle
$\rho_{\ln k,c}$	correlation coefficient between $\ln k$ and cohesion

$\rho_{c,\phi}$ correlation coefficient between cohesion c and friction angle ϕ

$\rho_{X,Y}$ correlation coefficient between X and Y

σ standard deviation

σ_F standard deviation of the performance function

σ_k standard deviation of hydraulic conductivity

σ_t total stress normal to the sliding plane

σ_X standard deviation of X

σ_x' effective normal stress in x direction

σ_Y standard deviation of Y

σ_y' effective normal stress in y direction

σ_z' effective normal stress in z direction

$\sigma_{v_{max}}$ standard deviation of the maximum local velocity

τ lag distance between two points in a random field

τ_{ss} shear stress

τ_{xy} shear stress in y-direction, acting upon a plane having its normal in the x-direction

θ volumetric water content

θ_h horizontal scale of fluctuation of hydraulic conductivity

θ_k scale of fluctuation of hydraulic conductivity k

θ_r residual volumetric water content

θ_s saturated volumetric water content

θ_v vertical scale of fluctuation of hydraulic conductivity

$\theta_{\ln k}$ scale of fluctuation of $\ln k$

ξ degree of anisotropy of the heterogeneity

Latin Symbols

$\mathbf{0}$ a null matrix

$\mathbf{1}_N$	matrix in which each element is equal to $1/N$
$\overline{\mathbf{x}}_t^f$	ensemble mean of $\mathbf{x}_t^f$
$\mathbf{D}$	matrix of measurement data perturbed by noise
$\mathbf{e}$	matrix containing vectors of measurement errors
$\mathbf{F}$	model used to forecast the state vector
$\mathbf{G}_{depend}$	vector of correlated values
$\mathbf{g}_{indepen d}$	vector of uncorrelated values
$\mathbf{H}$	measurement operator which relates the state vector to the measurement points
$\mathbf{h}$	vector of hydraulic heads
$\mathbf{h}^*$	a vector of real measurements
$\mathbf{h}_i$	a vector of perturbed measurements
$\mathbf{h}_{initial}$	hydraulic heads calculated from the initial estimations of the hydraulic conductivity field
$\mathbf{h}_{reference}$	hydraulic heads calculated from the reference hydraulic conductivity field
$\mathbf{h}_{updated}$	hydraulic heads calculated from the updated estimations of the hydraulic conductivity field
$\mathbf{I}$	identity matrix
$\mathbf{K_G}$	Kalman gain
$\mathbf{k}$	vector of natural log of hydraulic conductivity
$\mathbf{L}$	triangular matrix decomposed from $\boldsymbol{\rho}$
$\mathbf{m}$	vector used to derive effective stress vector
$\mathbf{P}_t^f$	error covariance matrix of the ensemble of forecasted state vectors
$\mathbf{R}$	matrix based on $\boldsymbol{\epsilon}_i$
$\mathbf{x}$	an ensemble of N state vectors
$\mathbf{x}_i$	state vector for the EnKF
$\mathbf{x}_t^f$	matrix containing the ensemble of forecasted state vectors
$\mathbf{x}_t^u$	matrix containing the ensemble of updated state vectors

$\ln k$	natural log of hydraulic conductivity k
$\ln k_{sat}$	natural log of saturated hydraulic conductivity k_{sat}
$\mathrm{VAR}(j)$	ensemble variance for each $\ln k_{sat}$
A	total area of the cross-section
A_p	area of the voids in the cross-section
c'	effective cohesion
c_f'	factored effective cohesion at slope failure
COV	coefficient of variation
$COV(X,Y)$	covariance between X and Y
COV_k	coefficient of variation of hydraulic conductivity
E	elastic stiffness
e	ensemble mean of k_{sat}
E_g	global kinetic energy of the water
E_l	local kinetic energy of the water
$E_{g,homo}$	global kinetic energy of the water in homogeneous case
F	performance function
g	gravitational acceleration
G_s	specific gravity of the soil particles
h	hydraulic head
H_c	hydraulic head across the structure
h_i^e	estimated values of hydraulic head
h_i^t	true values of hydraulic head
h_s	suction head
h_{PWP}	pore pressure head
$h_{s,ae,d}$	air-entry suction head for the main drying curve
$h_{s,ae,w}$	air-entry suction head for the main wetting curve
$h_{s,ae}$	air-entry suction head
i	an ensemble

i_c	critical exit gradient for piping
ii	a counter
j	Gauss point number
k_x	hydaulic conducitivity in the x direction
k_y	hydaulic conducitivity in the y direction
k_z	hydraulic conductivity in the z direction
k_{sat}	saturated hydraulic conductivity
L	seepage length
l	scale of fluctuation
l_h	scale of fluctuation in the horizontal direction
l_v	scale of fluctuation in the vertical direction
m	number of hydraulic head measurements
M_f	mass of fluid
N	number of ensemble members
n	fitting parameter in the SWRC
N_h	the number of unknown hydraulic head values in the foundation layer
n_p	porosity
N_k	number of unknown hydraulic conductivity values
nn	number of element nodes
p	pore water pressure
q	discharge
r	true value of k_{sat}
S	effective degree of saturation
s	matric suction
t	iteration number in steady-state or time in transient seepage
T_1	period of the first sinusoid
T_2	period of the second sinusoid
u_a	pore air pressure

u_w	pore water pressure
V	volume of soil
v_{max}^b	maximum local velocity at the bottom boundary
v_c	critical local velocity
v_d	deterministic maximum local velocity
v_s	pore seepage velocity
v_{max}	maximum local velocity of the whole domain
WL	water level
X	a variable
x	coordinate in the horizontal direction
Y	a variable
z	elevation or coordinate in the vertical direction

List of Figures

List of Tables

Acknowledgements

It has been a long journey to finish my PhD. At the completion of my thesis, I want to express my gratitude to all the people who have helped me to achieve my doctorate.

Firstly, I would like to thank my supervisors, Prof. Michael A. Hicks and Dr. Philip J. Vardon. Thanks for giving me this great opportunity of pursing a PhD in TU Delft. Thank you both for being so patient during my entire PhD study and spending lots of time to supervise me and review my work. I really appreciate that I could be one of your students.

Besides my supervisors, I would like to thank my colleagues in the Section of Geo-Engineering: Patrick Arnold, Hongfen Zhao, Yutian Yao, Jiao Yuan, Shuhong Tan, Yajun Li, Bin Wang, Rui Rui, Tom de Gast, Anders Beijer Lundberg, Bram van den Eijnden, Haoyuan Liu, Weiyuan Zhang, Qiang Li and others. Patrick, special thanks goes to you. You helped so much when I was struggling with my research. Thanks for reviewing my papers and your guidance. Meanwhile, I also want to thank my former and current office-mates: Richard de Jager, Vinh Pham, Luke Bergwerff and Arash Maghsoudloo. It is a great pleasure to share the room with you all.

Living in the Netherlands for over five years, I made a lot of friends here: Hua Zhong, Junchao Shi, Yaolu Liu, Zhebin Hu, Yujie Guo, Zhan Hu, Jiakun Gong and others. Thank you for sharing good times with me in Holland.

I would also like to thank my other committee members: Prof. Neil Dixon, Prof. Cristina Jommi, Prof. Bas Jonkman, Prof. Stefano Utili and Dr. Femke C. Vossepoel, for their time and comments on my thesis.

My gratitude also goes to the China Scholarship Council and TU Delft for their financial support during my PhD study.

Last but not least, I would like to express my gratitude to my family: my parents, my brother and my sister in law, and my lovely little nephew. Without your support, I would never have been able to come this far.

Curriculum Vitæ

Kang Liu was born on September 22, 1988, in a small city named Tianchang, Anhui province, China. He was educated there until he graduated from high school.

In 2005, he started studying Water Conservancy and Hydropower Engineering at Hohai University in Nanjing, China and obtained his Bachelor degree in 2009. After that, he was recommended to continue his study as a master student of Hohai University without taking part in the national graduate record examination because of his excellent record in the previous four years' study. During his master, his major was Hydraulic Structure Engineering, focusing on experimental research on soil strength by using a newly-designed in-situ direct shear test method. In January 2012, he received his master degree.

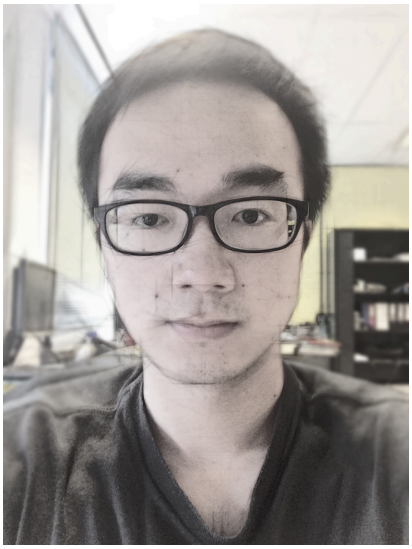

From February 2012, he started his PhD study in the Section of Geo-Engineering, Delft University of Technology, under the supervision of Prof. Michael A. Hicks and Dr. Philip J. Vardon. His PhD, which was funded by the China Scholarship Council (CSC), is to improve the calculation of slope stability for slopes under seepage, by means of inverse analysis and more realistic consideration of hydraulic behaviour.

List of Publications

Journal publication

1. Vardon, P. J., **Liu**, **K**., and Hicks, M. A. (2016). Reduction of slope stability uncertainty based on hydraulic measurement via inverse analysis. *Georisk: Assessment and Management of Risk for Engineered Systems and Geohazards*, 10(3):223-240.

2. **Liu**, **K**., Vardon, P. J., Hicks, M. A., and Arnold, P. (2017). Combined effect of hysteresis and heterogeneity on the stability of an embankment under transient seepage. *Engineering Geology*, 219:140-150.

3. **Liu**, **K**., Vardon, P. J., and Hicks, M. A. (2017). Sequential reduction of slope stability uncertainty based on temporal hydraulic measurements via the ensemble Kalman filter. Submitted to *Computers and Geotechnics*.

4. **Liu**, **K**., Vardon, P. J., and Hicks, M. A. (2017). Probabilistic analysis of seepage velocity distribution under earth embankments for internal stability. Submitted to *Environmental Geotechnics*.

Conference publication

1. **Liu**, **K**., Hicks, M. A., Vardon, P. J., and Jommi, C. (2015). Probabilistic Analysis of Velocity Distribution under Earth Embankments for Piping investigation. *5th International Symposium on Geotechnical Safety and Risk*, Rotterdam, pages 671-676.

2. **Liu**, **K**., Vardon, P. J., Arnold, P., and Hicks, M. A. (2015). Effect of hysteresis on the stability of an embankment under transient seepage. *International Symposium on Geohazards and Geomechanics (ISGG2015)*, Warwick, pages 012013.